Czech Technical University in Prague
Faculty of Electrical Engineering
Department of Electromagnetic Field

# Methods of Effective Signal Coupling into the Photonic Crystal Fibers

Doctoral thesis by Dmytro Suslov

Ph.D. Programme: Electrical Engineering and Information Technology [P2612]
Branch of study: Radioelectronics [2601V010]

Supervisor: Ing. Matěj Komanec, Ph.D.
Co-Supervisor: prof. Ing. Stanislav Zvánovec, Ph.D.

2021

# Declaration of Originality

I, the undersigned, hereby declare that this doctoral thesis is the result of my research in our research team and my contribution corresponds to that specified at the beginning of each research chapter. The thesis was written under the professional supervision of Ing. Matěj Komanec, Ph.D. and Prof. Ing. Stanislav Zvánovec, Ph.D., using the literature and resources listed in the Bibliography and References.

In Prague, 2021

.....
Ing. Dmytro Suslov

# Acknowledgement

First, I would like to thank my supervisors Matěj Komanec and Stanislav Zvánovec for the support and guidance they have provided during my work. They have provided me a great opportunity to be a part of an excellent optical team, filled with many great people.

I would also like to thank Radan Slavík at the University of Southampton for his cooperation and many discussions we had. The insight and the materials he provided have significantly contributed to this work.

Lastly, I want to thank my parents who supported and encouraged me throughout all my studies.

# Abstract

Photonic crystal fibers (PCFs) have been an interesting field of study for several decades. Their guiding mechanism is today well understood and there are drawing techniques capable of producing increasingly longer fibers, bringing the cost down and providing higher fiber availability. The flexibility of PCF design allows tailoring of the fiber properties for a specific application. However, the PCF's design differs significantly from the typical single-mode fibers (SMFs) that are widely used and readily available. Therefore, to fully utilize the PCFs an efficient coupling method of SMF and PCF is required.

The coupling method must be flexible enough to account for different PCF designs and their mode-field diameters to achieve minimal insertion losses. In case of hollow-core fibers (HCFs) the method should also reduce the Fresnel losses that occur at the interface between solid-core SMF and the air-core of HCF. Furthermore, it must be able to mitigate the cross coupling into higher-order modes (HOM).

In this thesis I first demonstrate a simple but accurate technique to characterize PCF properties, which enabled us to design an efficient coupling method with SMF. A real interconnection is then demonstrated based on the proposed coupling method for two different HCFs. Lastly I demonstrate use of the proposed interconnection technique in practical applications of HCF-based Fabry-Perot interferometer and microwave photonics HCF-based delay line.

# Key Words

Photonic crystal fibers, hollow-core fibers, coupling methods, fiber interconnections

# Abstrakt

Fotonická vlákna (photonic crystal fibers, PCFs) jsou již několik dekád velmi zajímavou oblastí výzkumu. Mechanismy vedení světla v nich jsou v současnosti již dobře popsány a navíc dnešní metody výroby vláken PCF umožňují dosažení stále delších úseku během jednoho tahu, což značně snižuje jejich cenu a tedy i zvyšuje jejich dostupnost. Flexibilita návrhu PCF umožňuje přizpůsobení vlastností vlákna ke konkrétní aplikaci. Nicméně návrh PCF se značně liší od typických jednovidových vláken (single-mode fibers, SMF), která jsou dobře dostupná a běžně využívána. Pro plné využití PCF je tedy nezbytné vyvinout metody efektivní vazby mezi SMF a PCF.

V návrhu takové vazby musí být zahrnuta velká škála možných PCF designů a profilů, včetně rozdílných šířek stopy pole (mode-field diameters, MFD). V případě dutých vláken (hollow-core fibers, HCF) taková vazba musí být schopna potlačit Fresnelovy ztráty, ke kterým dochází na rozhraní mezi pevným jádrem SMF a vzduchovým jádrem v HCF. Nakonec takové napojení musí být schopno omezit vybuzení vyšších vidů (higher order modes, HOMs).

V této práci nejprve představím odvozenou, ale přesnou metodu sloužící k popisu vlastností reálných PCF, na jejímž základě pak následně byla vyvinuta efektnivní vazba PCF se SMF. Takové propojení je pak demonstrováno na dvou různých HCF. Nakonec je ukázano využití metody propojení ve dvou praktických aplikacích interferometrů založených na HCF. Jedná se o ukázku Fabry-Perotova interferometru a zpožďovací linky založené na HCF.

# Klíčová Slova

Fotonická vlákna, hollow-core vlákna, metody vazby, vláknová propojení

# Contents


Page

**1 Introduction** **1**

**2 State of the art** **3**

2.1 Microstructured fiber design . . . . . 3

2.2 Coupling theory . . . . . 11

2.3 Coupling methods and interconnection techniques . . . . . 14

**3 Objectives of the thesis** **21**

**4 Accomplished results** **23**

4.1 Exact modeling of photonic crystal fibers for determination of fundamental properties . . . . . 25

4.2 Low-loss and low-back reflection hollow-core to standard fiber interconnection 32

4.3 Low loss and high performance interconnection between standard single-mode fiber and antiresonant hollow-core fiber . . . . . 37

4.4 Long-length and thermally stable high-finesse Fabry-Perot interferometers made of hollow-core optical fiber . . . . . 48

4.5 Optical Fiber Delay Lines in Microwave Photonics: Sensitivity to Temperature and Means to Reduce it . . . . . 54

**5 Conclusion** **63**

**References** **65**

**Author's Publications** **73**

**Curriculum Vitae** **75**

# Abbreviations

| | |
|---|---|
| $A_{\text{eff}}$ | Mode Effecive Area |
| ARC | Anti-Reflective Coating |
| ARF | Anti-Resonant Fiber |
| CL | Confinement Loss |
| ESM | Endlessly Single-Mode |
| FEM | Finite Element Method |
| GRIN | Graded-Index |
| HCF | Hollow-Core Fiber |
| HOM | Higher-Order Mode |
| IG-PCF | Index-Guided Photonic Crystal Fiber |
| LC-HCF | Large-core Hollow-Core Fiber |
| MFA | Mode-Field Adapter |
| MFD | Mode-Field Diameter |
| NANF | Nested Antiresonant Nodeless Fiber |
| PBGF | Photonic-Bandgap Fiber |
| PCF | Photonic Crystal Fiber |
| PRISM | Perturbed Resonance for Improved Single Modednes |
| SCG | Supercontinuum Generation |
| SMF | Single-Mode Fiber |
| SSL | Surface Scattering Loss |
| TEC | Thermally Expanded Core |

# CHAPTER 1 Introduction

The inception of photonic crystal fibers (PCFs) by T. A. Birks, P. S. J. Russell and their group at the University of Bath in 1995 [1, 2] has created a new and exciting field of optical fiber research. Thanks to the new principle of light guiding in optical fibers, this field has attracted much interest from the scientific community. Indeed, significant progress has been made in PCF in just two decades. Both from the a design point of view, and in terms of manufacturing and practical applications.

The first demonstrated PCFs had many defects in the air-hole structure and were only a few dozen centimeters long. However, with increasing sophistication and precision in the design and manufacturing process, it is now possible to tailor the properties of PCFs exactly, such as nonlinearity or the dispersion profile, to the specific application by changing the design of the air-hole structure. This is in stark contrast to bulk fibers, such as typical single-mode fibers (SMFs), where these critical properties are mostly dependent on the chosen material of the fiber.

Using PCFs, it is possible to tailor fiber nonlinearity $\gamma$ by changing the size of the core area of a PCF. A large core area and low $\gamma$ are beneficial for high-power delivery applications. On the other hand, there are many applications, such as supercontinuum generation (SCG) [3], optical parametric amplification or nonlinear pulse compression benefiting from high $\gamma$, which are possible in PCFs as $\gamma$ in ordinary SMFs is too low ($\gamma = 0.78\,\mathrm{W}^{-1}\cdot\mathrm{km}^{-1}$) to be efficiently used in a nonlinear application.

What is more, PCFs are capable of guiding light in air, confined by the surrounding glass structure in the hollow-core type fibers (HCFs). HCFs provide many additional benefits over typical SMFs. These stem from the fact that light propagates in the air, instead of in the glass material. Therefore hollow-core fibers are capable of low latency (speed of light propagation) [4, 5], low nonlinearity [4, 6, 7], high damage threshold, high thermal stability [4, 8] and potentially ultra-low losses. For these reasons HCFs have been identified as a possible candidate to replace existing SMFs for particular applications in telecommunication networks [9].

Typically a finite element method can be used to design and calculate PCF mode-field distribution. From mode-field distribution it is then possible to analytically derive PCF properties, such as dispersion, mode effective area ($A_{\mathrm{eff}}$) or $\gamma$. However, such an approach is insufficient because it is known that during the PCF drawing process a small

deformation of the air-hole structure occurs. These deformations happen due to small changes in viscosity, pressure or surface tension at the time when the glass material is melted. While the PCF air-hole deformation may appear small, they can result in significant errors in the derived PCF properties [10, 11]. This is especially true for the chromatic dispersion curve, as waveguide dispersion is typically dominant in PCFs.

New modeling techniques, such as the fluid dynamics model, attempt to overcome such limitations as this technique models the entire drawing process and, therefore, can predict the PCF air-hole structure deformation that can occur [12]. This technique can also help optimizing PCF drawing process which can improve produced fiber lengths and therefore reduce the cost of the PCFs [13]. This can, again, facilitate the wider adoption of PCFs into fiber-optic systems.

To easily incorporate PCFs into existing fiber-optic systems and networks, it is necessary to create a simple, permanent, reliable and cost-efficient solution for coupling PCFs with conventional SMFs.

Mode-field distribution of PCFs typically differs from that of SMFs. This must be accounted for to reduce coupling losses and is often compensated with a mode-field adapter (MFA). Additionally, if the difference in the refractive indices of PCF and SMF is presented, a Fresnel reflection can occur at the PCF-SMF interface. The reflection then causes both coupling losses and back-reflection, which can be detrimental in reflection-sensitive applications, notably high-power applications and interferometers. This is especially of interest in the case of HCFs as the air-glass interface presents a high contrast of refractive indices.

Common methods of permanent fiber interconnection, such as fusion splicing, are difficult to implement with PCFs, as there is a risk of air-holes collapsing due to overheating the glass material, back reflection not being mitigated with splicing and mode-field adaptation being hard to control.

This thesis focuses on methods of efficient coupling between SMF and PCFs. I will first briefly introduce the theoretical evaluation of the PCF-SMF interconnection. Then, I will overview existing methods of signal coupling into PCFs and the results that were achieved by these methods. Lastly, I will present my own work on this topic in the form of published journal papers, which will be accompanied by a short description of my contribution.

# CHAPTER 2 State of the art

In this section I overview the state-of-the-art achievements of the PCF-SMF coupling and interconnection. I start with a theoretical analysis of the interconnection and present the challenges. I then examine efficient coupling methods used to create a SMF-PCF interconnection starting with the least complex ones before continuing into more sophisticated solutions.

## 2.1 Microstructured fiber design

The topic of PCFs is incredibly broad with a vast history. In this thesis I limit the scope to two separate PCFs groups: index-guided PCF (IG-PCF) and HCF, where HCF can be further separated based on its guidance mechanism into photonic-bandgap fibers (PBGFs) and anti-resonant fibers (ARFs); ARFs are currently the most promising fiber design both in research and applications. Examples of the various PCF designs can be seen in Figure 2.1.

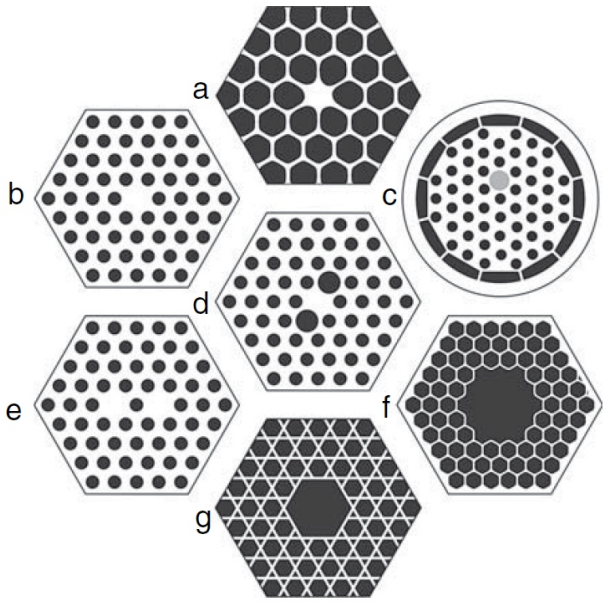


*Figure 2.1: Examples of PCF designs [14]. (a) highly nonlinear PCF, (b) endlessly single-mode PCF, (c) double-clad PCF with offset doped lasing core and high-numerical aperture inner cladding for pumping (d) birefringent PCF, (e) dual-solid-core PCF, (f) 19-cell hollow-core PCF, (g) hollow-core PCF with a Kagome lattice.*

The concept of photonic crystal was first described by Yablonovitch in 1987 [15]. However, it was not until 1995 when Russel and his group demonstrated the first photonic crystal fiber[1, 2]. Photonic bandgap presents periodic changes of refractive index, these then create the forbidden bands of wavelengths at which light cannot propagate. In PCFs these changes are created using a periodic air-hole structure in an otherwise homogeneous glass material and the light is then trapped in a bandgap structure defect - a missing air-hole in the center of the bandgap structure.

The PCF design presents many advantages since the PCF properties can be tailored by modifying the air-hole structure. For example, by changing the air-hole structure, waveguide dispersion of the PCF can be tailored to the specific application. This is because PCFs can be designed in such a way that waveguide dispersion becomes the dominant part of the chromatic dispersion.

In [16] it was shown that by using air-holes of varying sizes it is possible to better control the chromatic dispersion and its slope. In this paper the authors have presented a theoretical PCF design with ultra-flat dispersion of $0 \pm 0.5$ ps/(km·nm) from 1.19 to 1.69 µm. By using a different (sunflower) air-hole arrangement, it was shown [17] to provide a flat dispersion of $0.249 \pm 1.146$ ps/(km·nm) ranging from 1.20 to 1.84 µm.

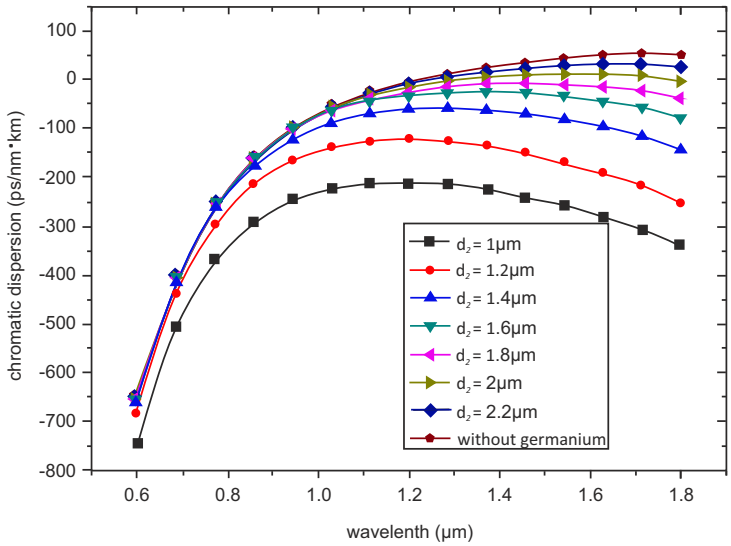


*Figure 2.2: Chromatic dispersion dependence on the core size of the germanium doped PCF [18]. Each curve shows chromatic dispersion for different diameter of the core in square PCF lattice. Calculated for pitch $\Lambda = 3\,\mu\,m$, air-hole diameter $d_2 = 2.2\,\mu m$*

Paper [18] presents a numerical analysis of the design with a square and triangular PCF lattice. This design provided chromatic dispersion ranging from -210 to 15 ps/(km·nm) over wavelengths from 0.6 to 1.8 µm and large birefringence in the order of $10^{-3}$. The resulting dispersion curve based on the PCF structure can be seen in Figure 2.2.

Another interesting property of the PCFs is their ability to guide only the fundamental mode at any wavelength. This is called endlessly single-mode (ESM) fibers [19].

A single-mode operation can be described by a normalized frequency that describes the cut off value for the fundamental mode. In PCFs this can be described as [19]:

$$V_{\text{eff}} = \frac{2\pi\Lambda}{\lambda}\sqrt{F}\sqrt{n^2_{\text{material}} - n^2_{\text{air}}}\,, \tag{2.1}$$

where $\Lambda$ is pitch (distance between the centers of the neighboring air-holes), air filing factor $F = \frac{d}{\Lambda}$ ($d$ is the diameter of the air-hole), $n_{\text{material}}$ is the refractive index of the fiber material and $n_{\text{air}}$ is the refractive index of air.

From Equation 2.1, we can see that the $V_{\text{eff}}$ can be changed via PCF design by modifying the parameters $\frac{\Lambda}{\lambda}$ and $F = \frac{d}{\Lambda}$. It is therefore possible to create a PCF air-hole structure where the PCF can exhibit endlessly single-mode behavior for any chosen wavelength. However, this does not mean that all PCFs are ESM. It is only true for the PCFs with smaller air-holes and, therefore, smaller air-filling factor $F$. Example of the $V_{\text{eff}}$ value based on $\frac{\Lambda}{\lambda}$ and $F = \frac{d}{\Lambda}$ parameters can be seen in Figure 2.3.

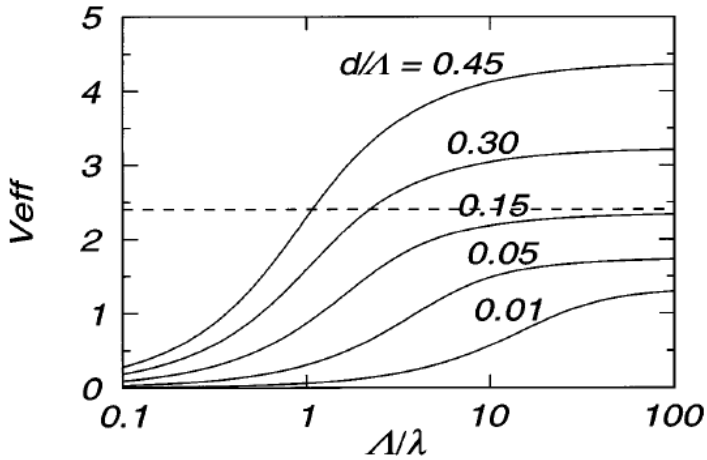


*Figure 2.3: The $V_{\text{eff}}$ values based on the $\frac{\Lambda}{\lambda}$ and $F = \frac{d}{\Lambda}$ parameters. Dashed line represents value 2.405 which is a cutoff value for SMFs [19].*

ESM behavior can also be understood by considering the air-hole structure to be a sort of modal filter where the transverse effective wavelength of the fundamental mode is too large to pass through the space between air-holes, and is, therefore, confined to the core area. HOMs can escape through the air-hole structure if $F$ is sufficiently small, since their transverse effective wavelength is shorter. With increasing size of the air-holes, the HOMs can be confined and propagate as well [19], [14].

PCF design can be further tailored for the specific application while still maintaining an ESM regime. In [20] the authors have shown ESM fiber where additional smaller air-holes were added around the core, which provided a good control of the dispersion curve and low bending loss due to good field confinement.

In [21] the authors have demonstrated an alternative method, where changes are made to the outer part of the the air-hole area while the core region remains unchanged. These changes include the size of the air-holes, as well as the insertion of rods with a high

refractive index. This allowed for the ESM regime to be achieved, low confinement loss (up to $10^{-6}$ dB/km) and a large mode area ($A_{\text{eff}}$ = 385 µm$^2$ at 0.8 µm, which is a 2.2 times improvement over the fiber without the high refractive index rods).

### Photonic bandgap fibers

Based on the principle of photonic crystal [15], a fiber can be constructed in such a way that the light will be guided in the air surrounded by a glass air-hole structure - the so-called hollow-core fibers. This requires propagation constant $\beta$ to be below vacuum wave vector $k_0$ and, in practice, results in designs with a high air-filling factor and a large core [14]. This was shown in practice in the first PBGFs where the fiber core was created by removing 7-cells (7 air-holes) from the center of the PBG structure [22], see Figure 2.4.

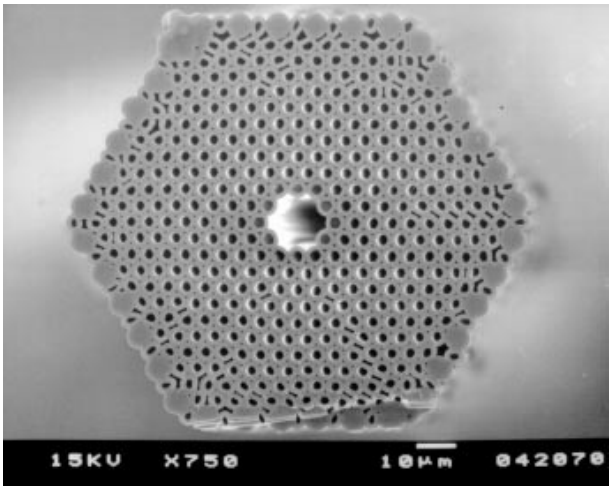


*Figure 2.4: SEM image of the first 7-cell HCF, as shown in [22].*

Guiding light in air presents many advantages compared to light propagating in a glass. It is theoretically possible to achieve waveguiding with lower attenuation than of state-of-the-art SMFs, as SMFs suffer from scattering losses (Rayleigh scattering) [23]. In HCFs, scattering can be minimized due to the low optical field overlap with the glass [14, 24], therefore it is theoretically possible to create a fiber with lower attenuation than the lowest reported solid-core fiber (0.14 dB/km [25]).

However, a different loss mechanism was identified for HCFs - surface scattering loss (SSL) [26]. During the HCF drawing process, when the glass melts, surface capillary waves can emerge which are then frozen into the fiber as it solidifies again. The light is then scattered on the surface of the hollow core. The origin of these surface capillary waves is thermodynamic and therefore cannot be mitigated by gradually improving the drawing process [24, 26].

Unlike Rayleigh scattering, SSL can be mitigated by a proper design of HCF [24, 26], particularly by enlarging the HCF core [27]. Since the overlap of the guided light will reduce with increasing core size, so will SSL. This was demonstrated on the first HCFs

where the 7-cell HCF offered attenuation of 13 dB/km[28] while increasing the core size to 19-cell improved attenuation to 1.7 dB/km[27], see the HCF structures in Figure 2.5. It was later identified that the attenuation reduction was partly due to the increase in core size and the thickening of the core boundary. The thickening creates an anti-resonance with the core mode which expels more light from the air-glass boundary thereby reducing SSL [26, 29].

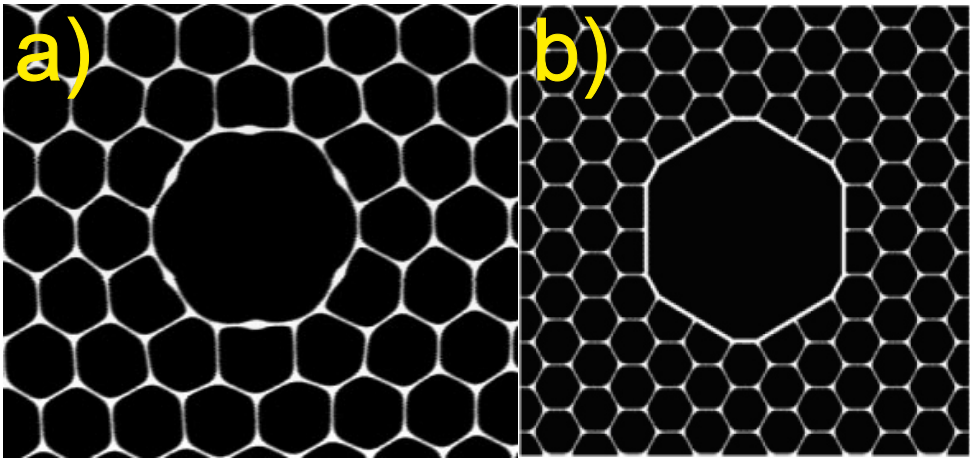


*Figure 2.5: SEM image of a) 7-cell, 13 dB/km attenuation HCF [28] and b) 19-cell, 1.7 dB/km attenuation HCF [26].*

The antiresonant effect was presented in a later study [30] where the authors managed to produce a fiber with 1.2 dB/km attenuation, which set a benchmark for HCF that was only recently surpassed. However, the addition of the thicker core boundary presented a drawback in the form of surface modes. These modes are guided at the edge of the core glass boundary and can be phase-matched with the core guided (fundamental) mode at certain wavelengths. This then forces the light to move to the surface of the core boundary which significantly increases losses of the guided mode [14, 27, 30, 31].

More recently, a 19-cell PBGF with a thin core boundary was presented [9]. In this work, through the optimization of their drawing process, the authors were able to shift the spectral regions of high loss to the edges of the transmission spectra, see Figure 2.6. This has resulted in a broad transmission window of 1.45 to 1.65 µm, which would be especially interesting for telecommunications. This application was also demonstrated in the paper by transmitting 37$x$40 Gbit/s channels at 1.154 µm.

A similar design approach was used in [32], although the focus was shifted into producing longer fiber lengths which is one of the crucial steps in implementing hollow-core fibers in wider range of applications, namely in telecommunications. As a result, an 11 -km-long 19-cell hollow-core PBGF was produced for the 1.55 µm telecommunication window and a 3.85 -km-long hollow-core PBGF for the 2 µm window. Attenuation at 2 µm was 3 dB/km with 160 nm bandwidth and 5 dB/km at 1.55 µm with 200 nm bandwidth.

However, increasing the size of the core presents an additional drawback as larger cores are able to guide HOMs. Therefore, increasing the size of the core as a means of

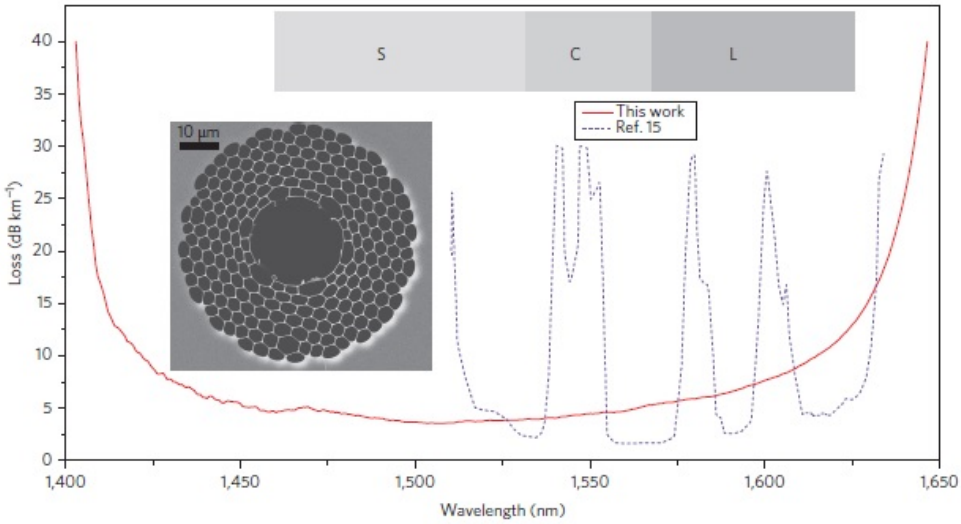


*Figure 2.6: 19-cell PBGF transmission spectrum with high loss regions shifted to the edges of the transmission spectrum [9].*

reducing attenuation will lead to fiber designs with only limited usage. A low-attenuation 19-cell hollow-core PBGF (with 20 µm core diameter) was calculated to support 35 to 45 modes [33] at 1.57 µm. The attenuation of the lower-order HOMs ($LP_{11}$, $LP_{02}$) was measured to be comparable to the fundamental mode in a 19-cell hollow-core PBGF. Only the $LP_{12}$ mode was showing attenuation of 480 dB/km higher than in the fundamental mode (5.9 dB/km at 1.52 µm) [34].

A novel design was presented with a focus on HOM suppression - a so-called Perturbed Resonance for Improved Single Modedness (PRISM) fiber [35]. In this paper, a 19-cell hollow-core PBGF was produced with fundamental mode attenuation of 7.5 dB/km at 1.59 µm. To reduce HOMs, two additional 7-cell (shunt) cores were created. These shunt cores were designed in such a way that they are phase-matched with the HOMs, see Figure 2.7. This leaves the central 19-cell hollow-core with only a fundamental mode propagating. However, such an approach necessitates a significant requirement on the manufacturing process since the additional cores are challenging to create, and even small defects can cause significant losses in hollow-core fibers.

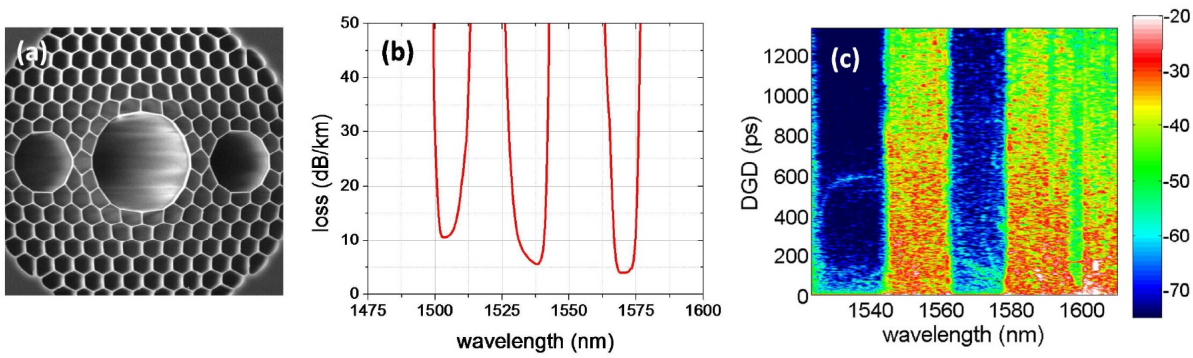


*Figure 2.7: (a) SEM image of a PRISM fiber, (b) its transmission spectrum and (c) the spectrogram showing HOM content (low HOM wavelengths are at 1530 and 1570 nm) [36].*

It is important to note, by optimizing hollow-core launch conditions it is possible to significantly limit the HOM excitation in the fiber. This was shown in [9], where polarization and coupling were optimized, see Figure 2.8. Additionally, a single-mode fiber was used at the output as a sort of spacial-filter which ensured that only fundamental mode was transmitted. This technique produced 30 dB HOM suppression.

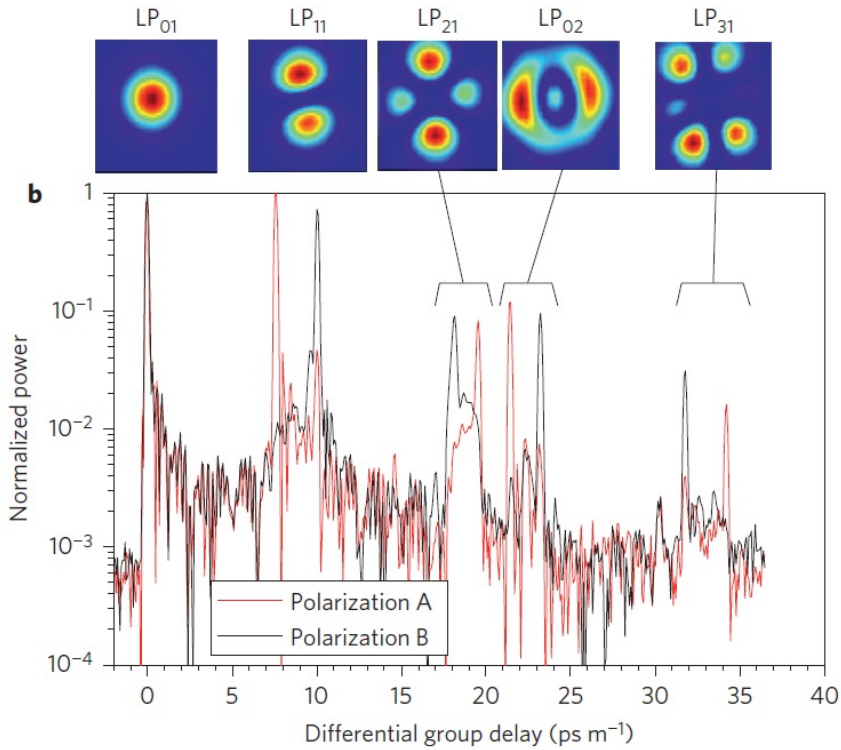


*Figure 2.8: HOM delay of 19-cell PBGF [9].*

In addition to PBGFs, a different mechanism of light confinement in the hollow-core was developed, namely anti-resonant fibers [37]. The so-called negative curvature fibers [38], a subsection of anti-resonant fibers, have, in particular, recently sparked interest due to their broadband transmission [39] and low attenuation [40] and boast the potential to rival attenuation of a typical SMF. In the negative curvature fiber the hollow-core is surrounded with glass capillaries. The thickness of the glass capillaries is designed so that it would be in anti-resonance with the guided mode. This excludes light from the glass material thereby minimizing SSL.

Negative curvature fibers demonstrate that it is possible to create all-silica fibers operational in the mid-IR region with attenuation significantly below the material scattering losses [41].

Authors in [42] demonstrated that if the capillaries are intersecting or touching, then such an intersection would be thick enough to act as a separate resonator and, therefore, guide modes. These modes can then be phase-matched with the core mode of the fiber which would exclude the core-guided mode into the cladding region and result in higher scattering losses.

An additional concern is confinement loss (CL). In typical hollow-core PBGF CLs are easily mitigated by using several rings of air-holes as cladding. Negative curvature fibers on the other hand use only one ring of glass capillaries. To minimize CL, a new fiber design was proposed - the so called Nested Antiresonant Nodeless Fiber (NANF) [43]. In NANF, an additional small, nested, glass capillary is added to the existing large ones, while the capillaries, otherwise, do not touch. These nested capillaries act as additional rings of the resonator and significantly reduce CL. [43] demonstrated that such a solution provides a 2-orders-of-magnitude improvement in confinement losses over a design without the nested elements (field intensity at the edge of outer glass cladding is at $10^{-6}$ of the maximum value for a design without nested resonators compared to $10^{-8}$ for the design with nested resonators, see Figure 2.9).

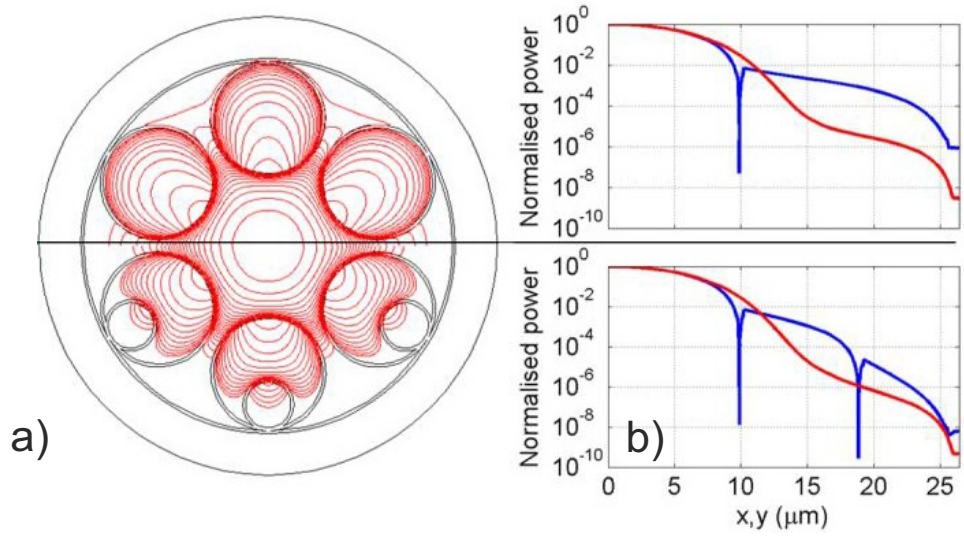


*Figure 2.9: a) Effect of nested resonators on confinement loss. Design with nested resonators is at the bottom, while the design without is at the top. Red curves denote the -3 dB contour plots. b) Poynting vector of the fundamental mode cross-section [43].*

Based on the design described in [43], rapid development and optimization have occurred within the last few years. This has produced fibers with attenuation of 2 dB/km [44] and 1.3 dB/km [45] in 2018, 0.65 dB/km in 2019 [46] and 0.28 dB/km in 2020 [40], which rivals the attenuation of conventional single-mode fibers.

NANFs have also demonstrated an exceptionally broad transmission spectra showing near octave spanning transmission spectrum [39], with attenuation below 100 dB/km overall and 25 dB/km at 1.2 µm. However, even in the latest paper [40], the presented NANF shows attenuation of 0.28 dB/km for 1.51 to 1.6 µm and below 0.3 dB/km for 1.51 to 1.64 µm spectra.

Regarding HOMs, the NANF presents nearly single-modal performance with the exception of the first HOM ($LP_{11}$). In [40] $LP_{11}$ mode shows attenuation of 12 dB/km, which is still an order of magnitude higher than the fundamental mode. All other HOMs show significantly higher attenuation of over 5000 dB/km.

## 2.2 Coupling theory

Spatial overlap of guided modes is necessary for efficient (low-loss) coupling of light from one fiber to the other. If the spatial distribution of the optical fields is not well matched, light could be coupled into HOMs, which typically have far higher attenuation than the fundamental mode and would result into losses. Admittedly, PBGFs, in particular, often have relatively low attenuation of lower-order HOMs (typically $LP_{02}$ or even $LP_{11}$). However, HOM excitation can cause asymmetrical losses when coupling between typical SMF and PCFs. This is because light can be coupled from SMF into the HOMs of PCF, so at short lengths of PCF they contribute to the total measured power, but HOMs propagating in PCF cannot be coupled into SMF. HOM suppression is interesting in applications sensitive to modal noise, e.g., interferometry [47], precise time [48], frequency transfer [49] and even telecommunications [50, 51], while low insertion loss (IL) is interesting in a high-power application.

To evaluate the quality of spatial mode matching, we can use an overlap integral, which is the coupling efficiency ($\eta$) of the two optical fields calculated as the spatial overlap of their respective electric fields:

$$\eta = \frac{|\int E_1^* E_2 \, dA|^2}{\int |E_1|^2 \, dA \int |E_2|^2 \, dA}, \tag{2.2}$$

where $E_1$ and $E_2$ are the transverse electric fields of the two coupled modes and integration is done over the entire fiber cross-section.

In practice it is also important to consider, that the two interconnected fibers might not be perfectly aligned, even if their mode-fields would otherwise be ideally matched. There could, therefore, be an additional transverse ($\eta_{tnv}$) and angular ($\eta_{ang}$) misalignment that can reduce the efficiency of the interconnect. Considering the Gaussian shape of the mode-field distribution we can calculate coupling transverse and angular efficiencies as [52]:

$$\eta_{tnv} = \frac{4w_1^2 w_2^2}{w_1^2 + w_2^2} \cdot exp\left(-\frac{2(\Delta x)^2}{w_1^2 + w_2^2}\right), \tag{2.3}$$

$$\eta_{ang} = exp\left(-\left(\frac{\pi \Delta\theta w}{\lambda/n}\right)^2\right), \tag{2.4}$$

where $w_1^2$ and $w_2^2$ are the radii of the mode field of the two particular fibers, $\Delta x$ is the transverse offset, $\Delta\theta$ is their angular offset and $n$ is the refractive index of the particular fibers.

Another issue to consider is the Fresnel reflection that occurs at the interface of the two materials due to the difference in the refractive indexes (e.g., glass core of typical SMF-28 fiber and air in hollow-core PCF). The Fresnel reflection would cause a small portion of light to be reflected rendering it as no longer available for coupling which translates to

interconnect losses (referred to in this work as Fresnel losses). Furthermore, the reflected light can be coupled back into the fiber and propagate in a backward direction. These back reflections can be detrimental in high-power applications, as even a small portion of power that is reflected and coupled back could cause the damage of some components.

The reflection coefficient $R$ and the resulting Fresnel loss can be described by [53, 54].

$$R = \frac{E_r \times H_r}{E_i \times H_i} = \left(\frac{n_1 - n_2}{n_1 + n_2}\right)^2, \tag{2.5}$$

$$L_{FR} = -10 \cdot log(1 - R), \tag{2.6}$$

where $E_i$, $H_i$ are incident wave electric and magnetic field intensity, $E_r$, $H_r$ are reflected wave electric and magnetic field intensity, $n_1$ is the refractive index of the first material (glass), $n_2$ is the refractive index of the second material (air).

Considering the above-mentioned phenomena, several studies attempted to analytically characterize the interconnection between two dissimilar fibers. These studies have often focused on the computational methods, their validity and efficiency.

In [55] the focus was on the theoretical analysis of the splice loss between the SMF and D-fiber using the Finite element method (FEM) as a basis. Using FEM allowed the transverse electrical field components of the fibers to be obtained and, subsequently, the overlap integral to be calculated. The misalignment, distance offset and even rotation of the two fibers (which could serve as an optimization tool for interconnect loss) were considered. It was found that the optimum splice-loss would occur at a distance of 1 µm with $0^o$ rotation when the two fibers are perpendicular. However, and more importantly, the study showed the importance of FEM, as well as the usefulness of overlap integral, in modeling fiber interconnects, even though the study was more focused on the effectiveness of the numerical method itself.

In 2001, a study was published that examined the impact of PCF properties on the resulting splice loss [56]. The interconnect between index-guided PCF with hexagonal lattice and SMF was examined. Parameters, such as air-hole diameter $d$, pitch $\Lambda$ and the air-filling factor $d/\Lambda$, were optimized for the interconnect loss. Interconnect losses were calculated using the Finite-differences time-domain method based on the monitoring of transmitted and reflected wave energy. A strong correlation between splice loss and the PCF lattice parameters was found. The study demonstrated that the PCFs can be optimized for an effective splice and that splice losses can be estimated analytically based on the PCF structure.

A similar analysis was conducted in [57]. The study considered an interconnect between SMF and index-guiding PCF. The interconnect losses were calculated from the overlap integral, while the mode-distributions were obtain using FEM. The study found similar results that showed a strong correlation between the PCF's $d/\Lambda$ and the splice loss. The loss ranged from as low as 0.1 dB up to ~5 dB. Interestingly, the study found

negligible Fresnel losses as the effective refractive indexes of the two fibers are considered to be similar and the study did not consider any gap between the fibers.

In another paper a numerical analysis was conducted with a focus on the Fresnel reflections in the PCF-SMF interconnect [54]. This study considered a nonzero incident angle between the two fibers and the effect of the PCF structure on the Fresnel loss. The study used a fully vectorial effective index method to calculate reflections. The study established a dependence between the PCF structure and the Fresnel loss. This is due to the effective refractive index dependency on the PCF structure. It was shown that by increasing $\Lambda$ (and therefore decreasing $d/\Lambda$) a Fresnel reflection can be reduced by over 50%. This reduction was attributed to the increase in the effective refractive index of the PCF. Additionally, Fresnel losses can be reduced by controlling the angle between the two fibers, e.g., in the special case of $45^o$ it was found that Fresnel losses are zero.

The crucial point of the above-mentioned studies is that they were theoretical analyses of the interconnects often focusing on the validity of the numerical method itself. The analyses considered PCF structure optimization as a tool to minimize splice loss or Fresnel loss itself, while disregarding more practical aspects that such PCF could be unsuitable for the required application.

## 2.3 Coupling methods and interconnection techniques

In this section I overview common coupling methods and relevant interconnection techniques, starting with simple butt-coupling, continuing with various mode-field adaptation techniques and ending with a permanent interconnection formed by fusion splicing or with the help of a free-space optics.

### Butt-coupling

The most simple and straightforward method for coupling of fibers with dissimilar MFD and field-distribution is butt-coupling as, for example, in [58], where conventional SMF-28 fiber and HCF are aligned. Using the divergence of the output light and aligning the two fibers with a gap that sets the MFD of the first fiber to match the input MFD of the second fiber. The experimental results show minimum IL of about 0.6 dB for both SMF-to-HCF and HCF-to-SMF direction. The effect of Fresnel-losses is considered, with the losses of 0.18 dB (4%), between the flat end of the glass fiber and air interface. However, using butt-coupling technique, it is not possible to reduce Fresnel-losses.

In [36] the authors have used another approach based on having an HCF equipped with a connector, which was created using PRISM type fiber and a custom made large mode area fiber, which served as MFA. The solid-core single-mode large mode area MFA allowed the deposition of an anti-reflective coating (ARC), which provided back-reflection suppression of -31.3 dB at 1571 nm (given by the ARC). The IL of the interconnect was 0.3 dB and that value was observed for both directions of propagation. This was likely the result of the PRISM fiber, as there were no HOMs. The disadvantage of this approach is the use of large mode area fiber, which has MFD of 14.5 µm and would likely add additional losses when coupled with a conventional SMF-28 type fiber (MFD = 10.4 µm).

### Graded-index mode-field adapters

Mode-field adaptation can be realized using graded-index (GRIN) fiber [59]. This technique utilizes the light propagation in GRIN fibers that follows a sinusoidal pattern. Therefore, controlling the length of the GRIN fiber, we can precisely control the resulting MFD and NA. Depending on the GRIN refractive index profile, length must be controlled with micrometer precision.

This technique was demonstrated experimentally in the coupling of SMF and PCF [61], where the 275-µm-long piece of GRIN fiber was spliced between SMF and PCF. This resulted in the coupling IL of 0.5 dB where 0.2 dB accounted for splicing losses.

A similar method was used in [60], where the authors coupled SMF with HCF, but used the no-core (coreless) fiber and set a gap between the GRIN fiber and HCF to better adapt

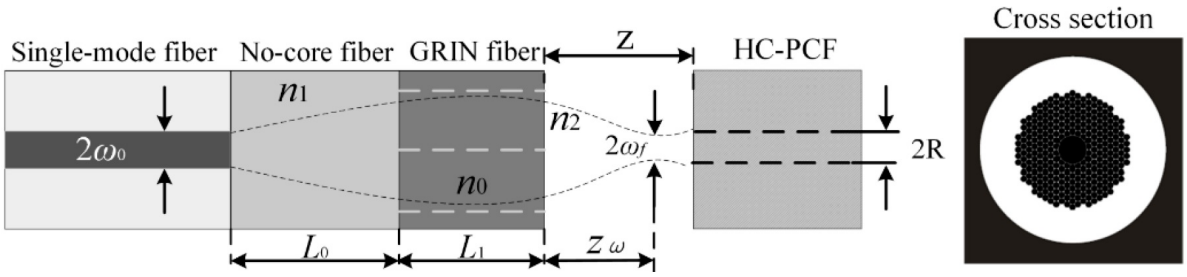


*Figure 2.10: Schematics of the coupling model presented in [60] along with the HCF cross-section.*

the SMF MFD. The schematics of the interconnection can be seen in Figure 2.10. While the theoretical analysis promised lossless interconnect, the experimental verification showed IL = 0.96 dB. The difference between the theoretical result and the experiment is mainly due to the calculation not considering the shape of HCF mode field-distribution.

## Thermally-expanded core mode-field adapters

MFD can also be enlarged by the thermally expanded core (TEC) of the fiber, typically SMF. TEC produces an adiabatic increase of core size and, thus, an increase of the MFD, provided that the core expansion transition is smooth and lossless. The TECs are mostly employed in laser diode coupling [62, 63] or waveguide coupling [64], nevertheless they can also be adapted for PCF coupling.

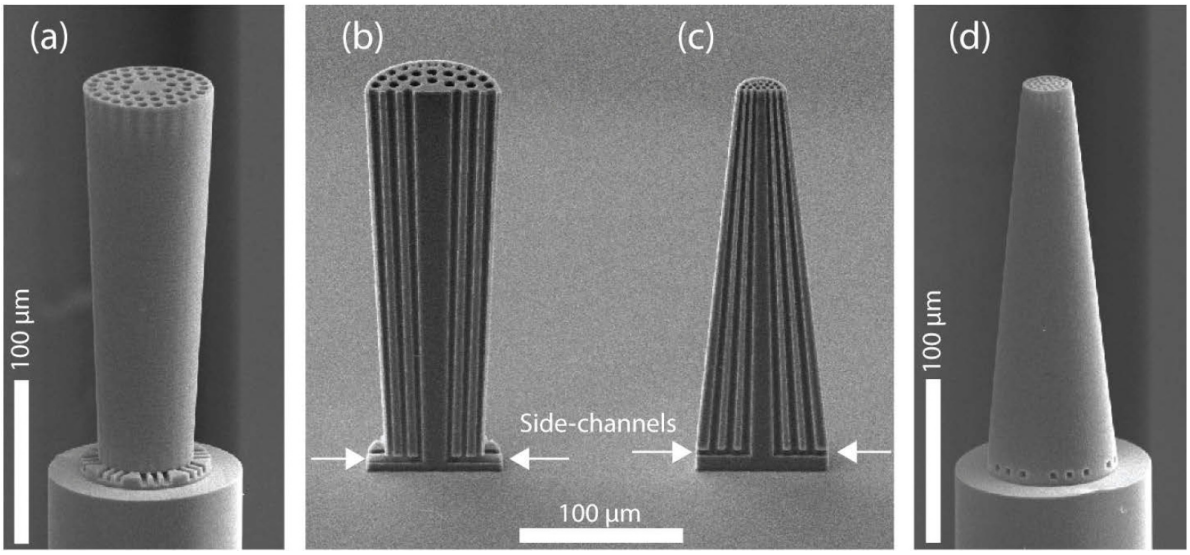


*Figure 2.11: SEM image of the fabricated (a) up-taper, (b) up-taper cross-section, (c) down-taper cross-section, (d) down-taper [65].*

The modification of MFD in SMF was examined in [65]. The authors presented a 3D printed polymer MFA that is printed on the SMF end. The adapters are designed as a PCF to allow for the better confinement of light and provide a wider range of mode-field adaptation. An image of the MFAs can be seen in Figure 2.11. Using this method, the

authors have demonstrated MFAs that are capable of expanding SMF MFD from the standard 10.4 µm up to 17.3 µm as well reducing it down to 4 µm. The 3D printed MFAs were experimentally demonstrated in SMF coupling with planar chips. In the case of down-tapers, the micro-structured MFA shows comparable losses to the step-index tapers IL = 1.53 dB, while the micro-structured up-taper shows superior performance IL = 1.10 dB over step-index IL = 1.77 dB. While this paper does not demonstrate coupling of the two dissimilar fibers, it presents a novel approach to MFAs, which can be adapted for coupling of optical fibers.

## Taper-based mode-field adapters

A novel method of coupling only to HCFs was presented in [66] using a so-called nanospike, which is a thinned tip of the SMF, see Figure 2.12. The nanospike was prepared by tapering the SMF down to 400 nm and then etching a 1- mm-long tip with a diameter of 150 nm. The tip was then inserted into the HCF core to create the interconnect. The interesting part of this coupling method is that due to the thin nanospike, the nanospike can align itself in the core of the HCF by the optomechanical force. This, therefore, requires a sufficiently strong (several hundred mW) optical signal to be present for the self alignment to work. The self alignment is capable of correcting even a 3 µm misalignment error, with soft glass materials allowing for even higher error correction [67]. Using the nanospike method it was possible to achieve IL of 0.57 dB. The Fresnel losses were measured to be about 0.0043 dB (~0.01%), which provides a tremendous improvement over the typical 0.18 dB (4%) silica-air reflection. This method was also tested in practical applications with liquid filled HCF [67] and a HCF gas-cell [68].

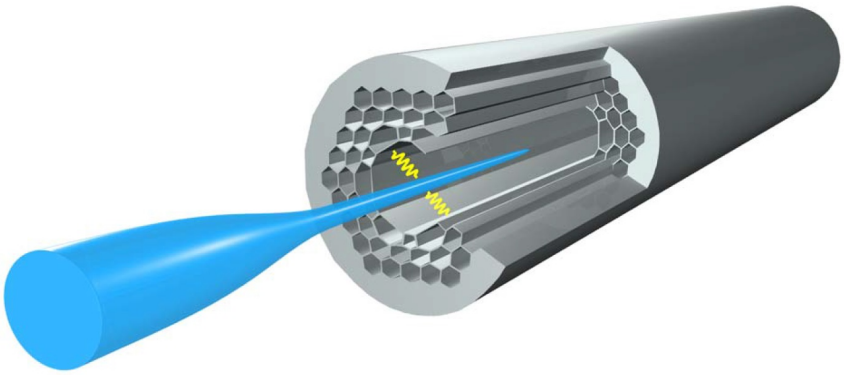

*Figure 2.12: Sketch of the nanospike coupling method [66].*

A similar method was used for coupling hollow-core and SMFs [69]. In this work, the authors have inserted the etched tip of the SMF into HCF. This creates an adiabatic transition between the SMF28 mode and the HCF mode. The difference in this case is that the etched fiber tip is too thick to align itself via the optomechanical forces, as was the case with the nanospike [66]. The insertion losses in this method strongly depend on

the angular misalignment between the etched tip and the axis of HCF and show a strong dependence on axial offset between the two fibers. To mitigate both of these problems the authors have etched SMF down to 16 µm, which is slightly smaller than the 20 µm core of the HCF. This significantly reduced the axial and angular misalignment error, as there is not enough physical space for it. Additional errors could also be produced by cleave angle, although the authors have identified this to contribute to a significantly lesser degree. Using this method, the authors were able to achieve overall IL of 0.79 dB, which was in agreement with the theoretical value calculated from the overlap integral. Furthermore, the authors have sealed the interconnect in a glass capillary with a UV glue, demonstrating a permanent interconnection.

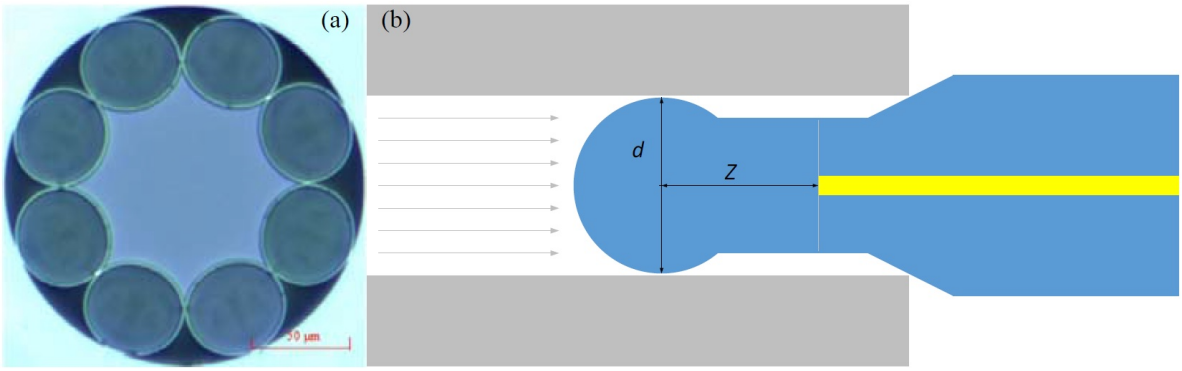


*Figure 2.13: (a) Image of the LC-HCF cross section and (b) the coupling principle of the LC-HCF with SMF using a ball lens [70].*

As with the etched fiber case, it is possible to use fiber tapers to achieve similar results [71, 72]. By tapering the SMF, the core of the fiber shrinks and the guided fundamental mode spreads out to the point where it is guided by cladding-air interface. This results in increase of MFD. In [71], the authors show a single coupling of SMF to ice-cream type ARF and SMF to NANF. By tapering the SMF to a 40 µm diameter, it was possible to experimentally demonstrate minimum coupling IL of 0.45 dB and 0.77 dB at 1570 nm for ice-cream type ARF and NANF, respectively.

In [72], the taper based interconnect was shown in the SMF-to-HCF-to-SMF configuration. The ice-cream shaped ARF was used in this paper. SMF was again tapered to a 40 µm diameter. The total coupling IL of this configuration was experimentally achieved to be 2.82 dB. The high losses were due to the MFD mismatch that allowed the HOM excitation, which increased losses when the light was coupled back into SMF. Furthermore, the authors have identified that the taper itself was not smooth and taper bending made the interconnect strongly dependent on the insertion depth of the taper and thus increased total losses.

A large-core HCF (LC-HCF) fiber with a core diameter of 110 µm was coupled with SMF in [70, 73]. The authors have found a significant improvement of coupling efficiency with an increase of SMF NA and, therefore, used a ball lens attached to the etched end of

the SMF which was inserted into the LC-HCF, see Figure 2.13. The result is a coupling IL of 3 dB that was achieved with SMF NA = 0.22, where the ball lens diameter was equal to the core diameter of LC-HCF (110 µm).

### Fusion splicing

Fusion splicing remains one of the most common methods for permanent fiber interconnection. It can be used for both splicing of common SMFs, PCFs [74, 75] and even HCFs [76, 77]. Over time several techniques for glass heating have emerged. From a simple torch flame [78] to filament heating [79] to modern techniques of arc-fusion [80] and $CO_2$ laser splicing [81], [82]. There are differences between these techniques, such as the heating area, heating uniformity or even usable materials.

The first paper reported PCF splice with dispersion shifted fiber was published in 1999 [74] with splice loss of 1.5 dB at 1.55 µm. It was also the first time that the basic properties of PCF, such as attenuation or dispersion, were experimentally measured. The mode area of the PCF used was 14 $\mu m^2$ while for dispersion shifted fiber it was 50 $\mu m^2$, therefore the authors attribute a large portion of the interconnect IL to the mode size mismatch. The paper states that the mode size mismatch alone can account for the observed 1.5 dB loss.

Further efforts were then made to develop an effective splicing method between PCF and SMF. The development of this technique with the use of a $CO_2$ laser is well described in the papers [81, 83]. [81] describes the practical considerations of PCF fusion splicing with regard to the vast range of PCF air-hole arrangements, the cleave unevenness, PCF contamination due to the humidity absorption, fiber misalignment or mode size and shape mismatch.

In [83] an experimental splice between PCF ($d/\Lambda$ = 0.682, $\Lambda$ = 12.22 µm) and typical SMF with IL ranging from 1.3 to 2.8 dB was demonstrated. The authors contribute most of the losses to the mode size mismatch.

Similar results were obtained using arc-based fusion splicers [84], showing IL ranging from 0.7 to 2.5 dB, based on the splicer arc duration.

However, both arc and $CO_2$ laser splicing revealed a major disadvantage in the form of the PCF air-hole collapse. This is because the solid-core SMF and PCF with delicate air-hole structures are heated at the same time, but the heat propagation in the two fibers is vastly different, which leads to the air-hole structure collapse. This has been addressed in [84–87]. For example, [84] showed that the air-hole structure collapse can influence the IL of a splice in the range from 0.8 to 3 dB. [86] managed to control the splicing process and limit the air-hole collapse by shifting the main heating area over the SMF and achieved IL ranging from 0.25 - 0.6 dB.

More recently this approach was shown in SMF-to-HCF splicing [77] where the authors also reheated the fiber after splicing. This was shown to reduce the IL by over 1 dB to 1.76 dB, while simultaneously increasing splice strength (from 50.6 to 52.2 kpsi).

Lastly, a study was shown on angled HCF-to-SMF splicing which would reduce Fresnel back reflection [76]. The ILs produced by the authors were around 1 to 2 dB and return losses were measured over -50 dB, however the angle cleaving of HCF proved difficult. Cleave angles ranged from 7 - 12° which made the interconnection properties inconsistent.

### Free-space optics-based interconnection

A recent method for PCF interconnection was shown using free-space optics. In [88] the HCF was integrated with SMF using micro-lens collimators. The SMF was first spliced with the MFA and a large mode area (LMA) fiber. The LMA was cut at an 8° angle to reduce Fresnel back reflection. The entire component was then packaged with two optical micro-lens collimators at the end of the LMA fiber and at the start of the HCF, see Figure 2.14. The experimentally demonstrated IL was 0.53 dB, Fresnel back reflection was measured at -47 dB. The authors also measured the HOM content showing $LP_{11}$ mode coupling at -20 dB. This setup was with an HCF-to-HCF interconnection configuration [88] with IL of 1.28 dB.

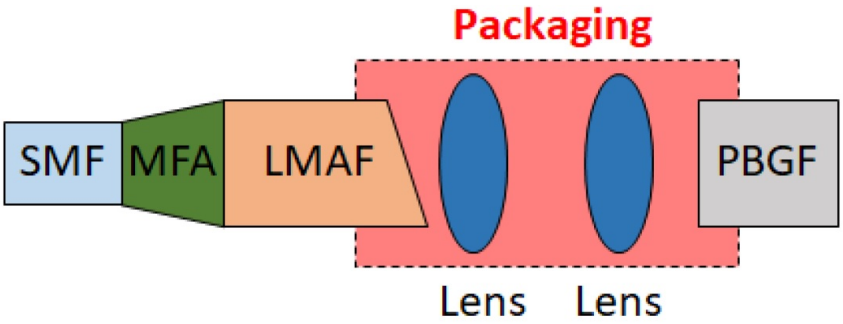


*Figure 2.14: Schematics of the micro-lens collimator based coupling solution [88].*

The same setup can be used to manufacture practical optical components. In [88] this was demonstrated by inserting an isolator between the micro-lens collimator. The total insertion loss of the isolator was 1.5 dB with > 40 dB isolation at 1550 nm.

This coupling method has been further demonstrated in various configurations [89] where several additional components were manufactured - 1x2 splitter, band-pass filter and WDM coupler, showing the versatility of this coupling method.

# CHAPTER 3 Objectives of the thesis

The rapid development of photonic crystal fibers and, in particular, hollow-core fibers have enabled numerous attractive research fields and practical applications. This has also brought an underlying need for efficient coupling methods of hollow-core fibers and conventional solid-core optical fibers, represented mostly by SMFs.

Such a coupling method (and subsequent interconnection) i) must be low-loss, since the state-of-the-art hollow-core fibers provide low attenuation and the coupling insertion loss is more significant; ii) must address Fresnel losses that occur at the glass/air interface between HCF and SMF (Fresnel losses present themselves in two ways: First, the power that is reflected at the interface cannot propagate further and, therefore, this increases the losses of the interconnection. Second, the power that is reflected can propagate in the opposite direction (back reflection), which is unsuitable for some applications, such as high power delivery); iii) must suppress HOM excitation because if HOMs are excited in HCF, they can typically propagate over long distances and they also manifest as asymmetrical losses since HOMs would not be coupled back from HCF to SMF. Additionally, HOMs can have a negative influence on many applications sensitive to modal noise, such as interferometry [47] or precise time transfer [48].

In this dissertation thesis I have therefore outlined the following objectives:

- Accurate PCF model including imperfections in the real post-draw PCF structure.
- Design and optimization of mode-field adaptation for SMF-to-HCF (HCF-to-SMF).
- A method of Fresnel loss suppression that occurs at the SMF-to-HCF interface.
- Proposal and experimental verification of bidirectional SMF-to-HCF (HCF-to-SMF) interconnection in a complete SMF-HCF-SMF fiber component.
- A practical evaluation of the proposed and developed interconnection with state-of-the-art hollow-core fibers, showing its high potential in cutting-edge applications.

# CHAPTER 4 Accomplished results

The accomplished results were published as peer reviewed papers in impacted journals and international conferences. Related publications and their relevance to the topic are outlined below. The full list of the author's publications is then given in Chapter 5.

Section 4.1 describes, in detail, a derived accurate model that includes photonic crystal fiber draw imperfections in the real post-draw PCF structure. The developed model can be used to quickly and accurately characterize any given PCF and obtain the necessary properties for the coupling method proposal and subsequent interconnection design. The results are experimentally verified using a sample PCF and show high agreement with the numerical results.

In Section 4.2 we present our novel coupling method on a sample of an SMF-to-PBGF-to-SMF interconnection. We use graded-index (GRIN) multimode fiber of a predefined length acting as MFA. The permanent interconnection is then formed by gluing two fiber arrays where MFA and PBGF are located. This method allows for ARC deposition on the MFA end-facet due to the low temperatures during the gluing process (as opposed to conventional fusion splicing where the ARC would be damaged) which eliminates Fresnel loss efficiently. We have reached a state-of-the-art IL of 0.3 dB, -30 dB back reflection, as well as the excitation of a fundamental mode with high suppression of unwanted HOMs.

The paper presented in Section 4.3 further develops on the results achieved in Section 4.2 demonstrating the SMF-to-NANF-to-SMF interconnection with the record-low IL of 0.15 dB per interconnection. We examine HOM excitation and show that the coupling method allows for the coupling of only -35 dB into $LP_{11}$ and -24 dB into $LP_{02}$ modes. The back reflection is again reduced using ARC down to -40 dB. We also compare the performance of OM1 fiber and OM2 fiber-based MFA and thermally-expanded core-based MFA. The best MFA with OM2 fiber is experimentally prepared using fast UV curable glue which results in a permanent NANF component with interconnected SMFs at both ends.

Section 4.4 shows the application of our coupling method and interconnection technique in a high-finesse Fabry-Perot interferometer. This requires a deposition of the highly reflective coating (>98%) on the GRIN MFAs. The MFA and NANF are then aligned and glued, forming a permanent interconnection. We demonstrate finesse of 154 and 130 for 5- and 23- m-long NANF, respectively, which corresponds to 47 and 50 kHz transmission peak bandwidth at -3 dB, respectively.

In Section 4.5 the impact of thermal stability was examined in application of delay lines in the microwave photonics. This paper compares several delay line designs. The NANF based delay line that is made using our interconnection technique is demonstrated. The use of NANF shows time delay changed per unit length as 2 ps/km/K, compared to 40 ps/km/K of SMF.

## 4.1 Exact modeling of photonic crystal fibers for determination of fundamental properties

Reference paper:

D. Suslov, M. Komanec, T. Němeček, J. Bohata, S. Zvánovec, "Exact modeling of photonic crystal fibers for determination of fundamental properties" *Optical Fiber Technology*, 2020, 56 ISSN 1068-5200.

Relevance to the thesis:

For efficient coupling between PCF and SMF, a precise characterisation of the real PCF structure is essential. However, measuring each PCF property experimentally is both time and cost intensive. Another option is to derive PCF properties from the model. This requires an accurate model of the post-draw PCF air-hole structure. During the PCF drawing process the air-hole structure suffers many small defects. Air-holes can change their diameter and even shape (they become elliptical). However, many PCF models ignore these defects outright and consider ideal or idealized fiber structure (e.g., that all air-holes have the same diameter and are circular). In this paper I examine the significance of these air-hole defects on the resulting PCF properties, as well as examine the impact of imprecise refractive index characterization. I outline the necessary steps to easily prepare an accurate PCF model based on an image of the PCF cross section (requires only a short piece of PCF). Finally, the results are experimentally verified and the difference between ideal and real fiber is demonstrated on an example of supercontinuum generation.

Optical Fiber Technology 56 (2020) 102177

Contents lists available at ScienceDirect

Optical Fiber Technology

journal homepage: www.elsevier.com/locate/yofte

# Exact modeling of photonic crystal fibers for determination of fundamental properties

Dmytro Suslov*, Matěj Komanec, Tomáš Němeček, Jan Bohata, Stanislav Zvánovec

*Department of Electromagnetic Field, Faculty of Electrical Engineering, Czech Technical University in Prague, Technicka 2, Prague 6 166 27, Czech Republic*

ARTICLE INFO

*Keywords:*
Photonic crystal fiber
Optical fiber modeling
Mode-field distribution
Supercontinuum generation

ABSTRACT

We present a simple but highly accurate modeling technique for real photonic crystal fibers (PCFs) characterization. We determine the influence caused by idealized model parameters. Our technique can be applied to arbitrary PCF air-hole structures, as it takes into account all structural distortions. It requires only an image of the PCF cross-section to create an accurate PCF model. Model outputs are presented in comparison with the measurement of chromatic dispersion curve and the effective mode area. We provide a study on the impact of imprecise determination of glass refractive index on the PCF model accuracy. We demonstrate how the simplification of the air-hole deformations can influence the chromatic dispersion curve. Finally, we show the effect of precise PCF modeling on example of supercontinuum generation.

## 1. Introduction

Photonic crystal fibers (PCFs) are widely used thanks to the versatility and freedom of their design. This allows to specifically tailor PCF properties towards individual applications such as supercontinuum generation (SCG) [1,2], sensing [3,4] or signal filtering [5].

Various methods have been proposed for efficient PCF design and tailoring of their properties [6,7]. These methods enable us to derive the PCF chromatic dispersion (CD) curve, mode-field distribution, or effective mode area ($A_{\mathrm{eff}}$) [8]. Moreover, results of PCF application, such as SCG, can be predicted even prior to the drawing of the PCF.

The PCF drawing process, however, can introduce distortions to the designed PCF air-hole structure causing significant differences from the pre-draw PCF design. The effect of such distortions has been studied in hollow-core fibers in [9–11], as well as in index-guided PCFs [12]. These distortions were found to cause an increase in insertion loss (IL) by a factor of ten [10], as well as a more than a 0.2 μm reduction in the PCF transmission bandwidth [10].

It is possible to predict the PCF structure evolution during the fiber drawing process by considering the pressure applied to the outer cladding and the surface tension, pressure and the viscosity of the air-hole microstructure (using the fluid dynamics model) [13]. However, this approach has its limitations and requires exact knowledge of the drawing process and as such, it is impossible to apply this method to characterize already drawn PCFs.

PCF parameters (CD, mode-field distribution, $A_{\mathrm{eff}}$) can be measured directly [8]. However, such approach is often time and cost-intensive. A fast and accurate method capable of deriving PCF properties based on the simulation model is preferable.

In this paper, we present an easy, straightforward and precise technique of PCF characterization based on the creation of an exact model of the post-draw PCF. This technique works well even with a short PCF segment (with length less than 1 m) and can be carried out in just 3 subsequent steps: i) At first, an accurate photograph of the PCF structure is acquired; ii) next refractive index (RI) of the glass is obtained; and iii) finally, the PCF model is created. Even though separate steps of this technique are known, a comprehensive study of the entire process is missing. Moreover, the impact of the modelling precision and air-hole structure deformation is provided, with regard to CD and SCG.

To demonstrate this technique, two models of a sample lead-silicate PCF are presented. The first one presents a precise post-draw PCF model with accurate PCF properties and the second model includes a simplified air-hole structure. Finally, the presented technique is verified by measurement of CD and $A_{\mathrm{eff}}$.

## 2. PCF model

We start our model with the PCF structure by acquiring the image of the unknown PCF cross-section. Then we determine the refractive index of the PCF glass material. Combining these two steps, we create the whole PCF model and calculate PCF properties using a finite element method (FEM) solver.

* Corresponding author.
*E-mail address:* suslodmy@fel.cvut.cz (D. Suslov).

https://doi.org/10.1016/j.yofte.2020.102177
Received 26 August 2019; Received in revised form 29 January 2020; Accepted 19 February 2020
1068-5200/ © 2020 Elsevier Inc. All rights reserved.

The following sections describe each of these steps in detail.

### 2.1. Air-hole structure

In literature, PCF structures are typically described by parameters such as the core diameter, the diameter of the air-holes (for each ring) and the distance between the air-holes (lattice constant/pitch) [14–16]. These parameters are often used in the PCF design process and therefore may lead to the assumption that the drawn PCF would have the same regular structure. However, this is usually not the case, as during the PCF drawing process distortions of the air-hole structure occur. These can then change/shift the shape/position of the air-holes, which can also lead to the change or deformation of the core area diameter. The distortions can influence each individual air-hole differently.

To obtain a precise PCF model, these distortions must be taken into account. For FEM based model, it is necessary to create a mesh that provides a representation of the PCF structure. This mesh must include all the distortions, therefore a detailed image of the PCF cross-section is needed. A scanning electron microscope (SEM) is typically used to capture the image, however we have found that for some types of PCFs an ordinary light microscope (OLM) can be used as well. An OLM with at least 400x magnification can provide enough detail for some simpler PCF structures, such as suspended-core PCFs. For more complicated structures with many air-holes, the use of SEM is necessary as OLM typically does not provide high enough resolution to capture the exact dimensions of the air-holes with a diameter in the order of micrometers. The comparison of microscopes usage can be seen in Fig. 1, where the image of suspended-core PCF cross-section is obtained with OLM as shown in Fig. 1a) and with SEM shown in Fig. 1b). The same comparison is then shown for a honeycomb PCF with small air-holes - see OLM image in Fig. 1c) and SEM image in Fig. 1d).

The captured image is then converted into a mesh using vector graphic software, where the outlines of the air-holes are drawn as vector elements which then form the PCF model. This allows us to capture all the distortions of the PCF structure. Since only the image of PCF cross-section is required, a very short piece of PCF is sufficient (e.g. cleaved-off PCF segments).

### 2.2. Refractive index

The second step of the PCF model is getting the RI dependence on wavelength, i.e. RI curve of the glass material. For a glass material, RI is described by the well-known Sellmeier equation [17]:

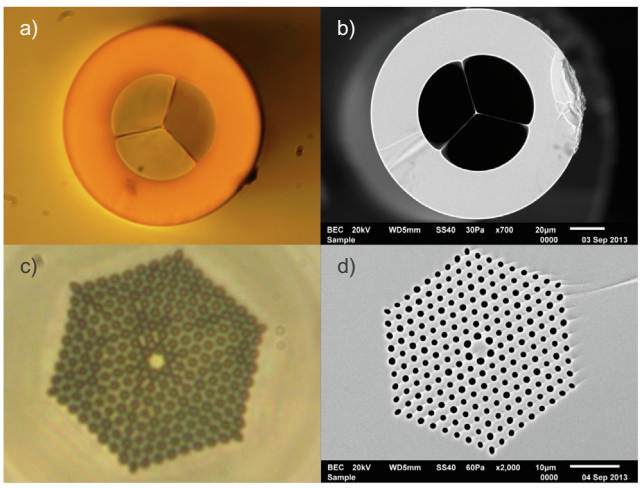


**Fig. 1.** Comparison of cross-sections of: a) suspended core PCF end-facet obtained with 400× magnification using OLM, b) suspended core PCF obtained with 700× magnification using SEM, c) PCF obtained with 1000× magnification using OLM, d) PCF obtained with 2000× magnification using SEM.

$$n(\lambda) = \sqrt{1 + \sum_{n=1}^{N} \frac{B_n \lambda^2}{\lambda^2 - C_n}} \tag{1}$$

where $\lambda$ is wavelength, $B_n$ and $C_n$ are $n$-th fitting coefficients.

Many of glass materials commonly used for manufacturing PCF have already been well defined and their fitting coefficients are readily available [18]. Glass RI values for each wavelength are commonly described with the precision of $10^{-4}$ and wavelength spanning from visible to near-infrared region.

However, newly developed glass materials require a detailed study of their respective RI curves. For proper PCF characterization, the RI curve must be measured with the above-mentioned precision of $10^{-4}$ for each value of RI. For this purpose, the Abbe refractometer is commonly used with the modification for the infrared region [19].

### 2.3. Modelling approach

One of the commonly used methods for the computation of modal properties in a PCF is FEM, which is a well-described method [20] [21] with many of the commercially available solvers. In this paper, we use Comsol Multiphysics 5.1 as a direct full-vector FEM eigenvalue solver.

The derived mode field distribution can provide several parameters like effective refractive index ($n_{\text{eff}}$), electric field intensity $E$ and the propagation constant ($\beta$) for a given wavelength. Also CD and $A_{\text{eff}}$ can be investigated. Especially CD curve can be used as a good tool for PCF examination since it is susceptible even to the small changes of the air-hole structure or glass material RI. The CD coefficient for each wavelength is determined as [22]:

$$D(\lambda) = \frac{-2\pi c}{\lambda^2}\beta_2 = \frac{\lambda}{c}\frac{\partial^2 \text{Re}(n_{\text{eff}})}{\partial \lambda^2} \tag{2}$$

where $c$ is the speed of light and $\beta_2$ is the group velocity dispersion.

$A_{\text{eff}}$ represents a significant parameter for nonlinear applications, which are typical uses of many PCFs. We calculate $A_{\text{eff}}$ by integrating the intensity of the electric field over the surface of the fiber end ($A$) as [22]:

$$A_{\text{eff}} = \frac{(\int I dA)^2}{\int I^2 dA} = \frac{(\int |E^2| dA)^2}{\int |E^4| dA} \tag{3}$$

where $I$ is the near-field optical intensity.

## 3. PCF model example

To demonstrate the impact of air-hole distortions and imprecise RI determination, a sample PCF is examined. We have selected a hexagonally-structured PCF made of lead-silicate glass (denoted as PBG-$08_1$) with the composition of PbO: 39.17%, $Bi_2O_3$: 27.26%, $Ga_2O_3$: 14.26%, $SiO_2$: 14.06% and CdO: 5.26%. Image of the sample PCF structure can be seen in Fig. 1d). We have created two models of this sample PCF.

### 3.1. PCF air-hole structure models

"Model 1" is based on the real post-draw PCF. This model is created by vectorization of the image of the PCF cross-section obtained with SEM. Therefore, this PCF model provides an accurate representation of the real post-draw PCF and the properties derived from this model match the properties of the real PCF (as will be shown later). This model is an exact copy of the PCF cross-section, it includes all air-hole shape deformations and size changes that occurred during drawing process. For this reason this model is not described by standardized PCF parameters that describe air-hole structure (air-hole diameters, pitch, core diameter).

"Model 2" is a commonly used, but simplified model. We present it to demonstrate how even small changes in the PCF air-hole structure

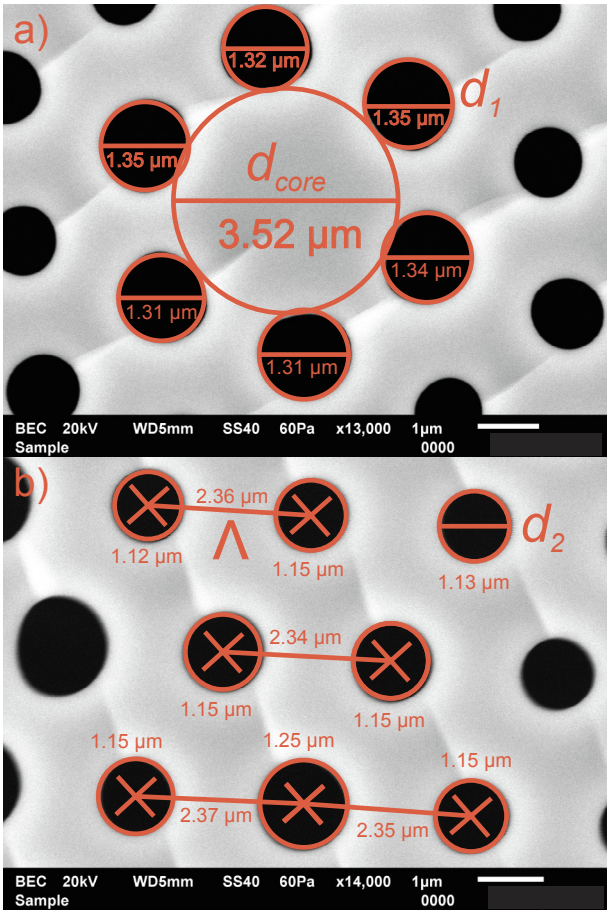


**Fig. 2.** Example of PCF air-hole structure parameter measurement for Model 2. Details of a) the measured diameter $d_1$ of the innermost rings, b) measured diameter $d_2$ of outer rings and the distance between air-holes (Λ).

(comparable to varying real parameters) can influence the derived PCF properties and that at first look reasonable simplifications of the PCF air-hole structure can lead to significantly incorrect results.

Model 2 is created using post-draw PCF structure as a template (the identical SEM image of the PCF cross-section that is used for Model 1), however in this case we consider all of the air-holes to be perfectly circular having the same specific air-hole diameter $d_1$ for all air-holes in the innermost ring and $d_2$ for all air-holes in the outer rings, the same distance between air-holes (pitch—Λ) and a core diameter ($d_{core}$).

Each of these parameters is obtained by averaging the measured values that can be seen in Fig. 2. First, we average all of the innermost ring air-holes to obtain parameter $d_1$ and then air-holes in outer rings to obtain parameter $d_2$. Last, we average distances between the air-holes to obtain parameter Λ. In our case, we have measured $d_1 = 1.33$ µm, $d_2 = 1.15$ µm, $\Lambda = 2.35$ µm and $d_{core} = 3.52$ µm. The core areas of the resulting air-hole structures of Model 1 and Model 2 are compared in Fig. 3.

### 3.2. Refractive index curves

Following the PCF model creation step, we now examine the impact of imprecise glass RI determination on the PCF model outputs. The Sellmeier coefficients of the lead-silicate glass (PBG-08$_1$) of the sample PCF were published in [16]. Refractive index is dependent on wavelength, thus precise characterization of RI is necessary to obtain correct PCF model results. This can sometimes present a challenge for new and experimental PCF materials, such as one used in our sample PCF. To demonstrate the effect of such an imprecision, we have constructed a

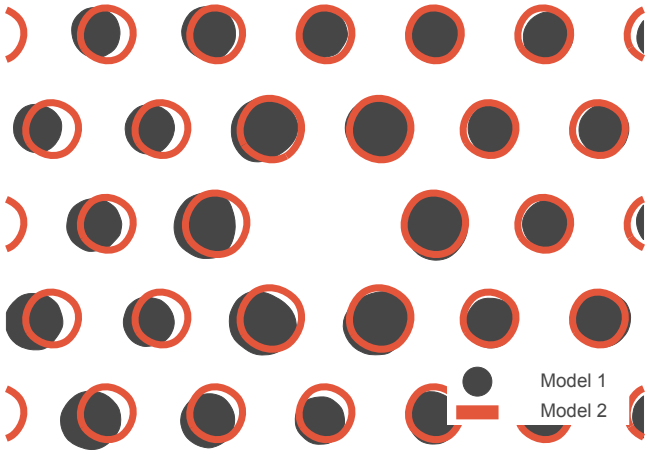


**Fig. 3.** Detail of the sample PCF core area. Model 1 is drawn in full black and Model 2 is represented by the red outlines.

**Table 1**
Sellmeier equation coefficients of the PBG-08 glass. PBG-08$_1$ are data presented in [16], PBG-08$_2$ are derived coefficients of the shifted RI curve.

| | PBG-08$_1$ | PBG-08$_2$ |
|---|---|---|
| $B_1$ | 2.0118814 | −0.385 |
| $B_2$ | 0.5467324 | 3.264 |
| $B_3$ | 1.3948861 | −0.3491 |
| $C_1$ | 0.011537 | −0.1281 |
| $C_2$ | 0.063552 | 0.004391 |
| $C_3$ | 141.65405 | −0.1265 |

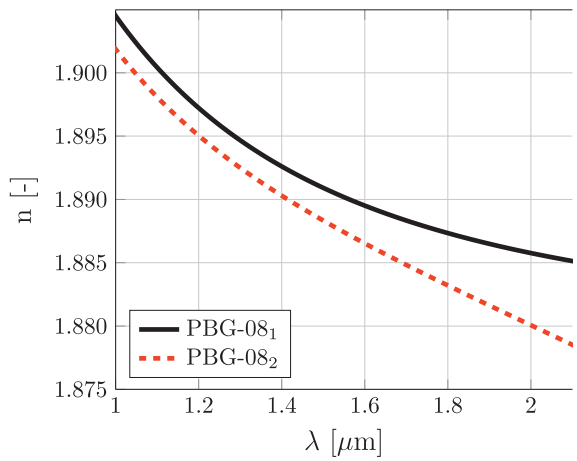


**Fig. 4.** Refractive index curves of PBG-08 glass; PBG-08$_1$ are data presented in [16], PBG-08$_2$ is shifted RI curve.

second RI curve (PBG-08$_2$), which is shifted and diverges in the longer wavelength region from the RI curve in [16] (PBG-08$_1$). Both examined RI Sellmeier equation coefficients are presented in Table 1 and in Fig. 4.

Here we can see that the two RI curves are merely shifted in the shorter wavelength region, but at longer wavelengths the two curves begin to diverge with difference in order of 0.005.

### 3.3. Model results

We have evaluated the impact of the RI curves on CD, which can be determined using Eq. 2. The calculation is carried out for Model 1 using two RI curves depicted in Fig. 4. We use a single model (Model 1) of air-hole structure, since a dominant part of CD in PCFs is formed by waveguide dispersion. Therefore, to demonstrate only the impact of RI on

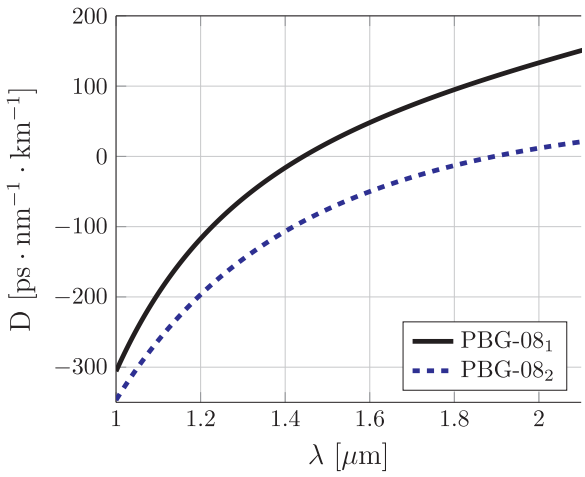


**Fig. 5.** Calculated chromatic dispersion curves using Model 1 with RI curve PBG-08$_1$ obtained from [16] and PBG-08$_2$ obtained from derived coefficients of the shifted RI curve.

the resulting CD, a single PCF model must be used. Calculated CD curves are then shown in Fig. 5.

This result underlines the fact that even small differences in RI such as ~ 0.005 can cause a significant divergence in the CD curves with a zero-dispersion wavelength (ZDWL) shift of up to 0.450 μm ($ZDWL_{PBG-08_1}$ = 1.445 μm and $ZDWL_{PBG-08_2}$ = 1.895 μm).

Seeing the strong effect of the glass RI, we study the effect of the air-hole structure deformation. CD curves are calculated for Model 1 and Model 2 using Sellmeier coefficients of PBG-08$_1$. The results can be seen in Fig. 6. The CD curves for Model 1 and Model 2 are in a good agreement for shorter wavelengths, but as wavelength increases the CD plots begin to diverge significantly (difference of 23.46 ps·nm$^{-1}$·km$^{-1}$ at 1.550 μm and 49.57 ps·nm$^{-1}$·km$^{-1}$ at 2 μm). The ZDWL shift between Model 1 and Model 2 is 0.077 μm (1.445 vs 1.522 μm). Such differences in CD curves can have significant consequences for practical applications which are discussed more in Chapter 5.

$A_{\text{eff}}$ is calculated for both Models using Eq. 3. The values of the electric field of the examined mode were obtained from FEM solver at $\lambda$ = 1.550 μm. The results are shown in Table 2.

These results show that there are only minor differences (0.01 μm$^2$) in $A_{\text{eff}}$ between the RI curves. However, there are noticeable differences in the $A_{\text{eff}}$ between the two models (0.71 μm$^2$), as the changes in the air-hole structure significantly affect the physical dimensions of the waveguide and therefore the mode-field distribution of the fundamental mode in PCF.

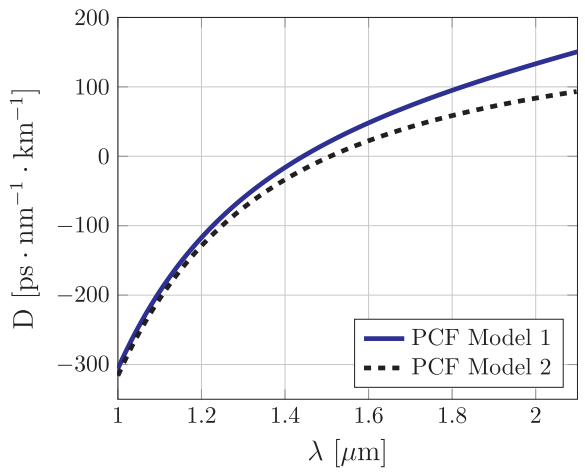


**Fig. 6.** Comparison of the CD curves for Model 1 and Model 2. Both models consider PBG-08$_1$ glass.

**Table 2**
Calculated $A_{\text{eff}}$ values at $\lambda$ = 1.550 μm.

| | PBG-08$_1$ | PBG-08$_2$ |
|---|---|---|
| $A_{\text{eff model1}}$ [μm$^2$] | 7.92 | 7.91 |
| $A_{\text{eff model2}}$ [μm$^2$] | 7.20 | 7.20 |

## 4. Verification of PCF model parameters

To demonstrate that our technique yields accurate values, we have verified the presented PCF model via the CD curve and $A_{\text{eff}}$. Note that these measurements are not necessary to create the PCF model.

### 4.1. Chromatic dispersion measurement

The CD curve of the sample PCF is measured using the free-space interferometric method [23], which is based on the measurement of the optical path difference between two signals propagating in the reference (free-space) path and measured (sample PCF) path – see the setup of the measurement depicted in Fig. 7.

In this setup we use a supercontinuum (SC) source (NKT SuperK Extreme EXR-15) as a broadband light source which allows us to measure the entire spectrum at once. The 6 W output of the supercontinuum source is launched via a free-space collimator and split in a 96/4 ratio via a wedge glass prism, where the 4% signal is further filtered using an optical filter (Thorlabs FELH0750) to remove the visible part of the SC spectrum. The signal is then split into two arms in free-space using a 50/50 beam splitter (BS) (Thorlabs PBSW-1550). The measurement arm contains the PCF and lens 1 and lens 2 (both Thorlabs C660TME-C) used to couple the signal into and out of the PCF. These lenses are positioned on the micromovement stage to enable alignment with sub-micron precision. The reference arm contains a micromovement stage with two mirrors (Thorlabs PF10-03-P01) that allow the tuning of the optical path length. The output of both arms is then combined on another 50/50 BS (Thorlabs PBSW-1550) and coupled into the output fiber using lens 3 (convex lens with $f$ = 5 cm). Resulting data are visualized via the optical spectrum analyzer (OSA) (Yokogawa AQ6370C).

These measurements provide a spectral interferogram which can be observed at OSA as a beat signal at specific wavelengths. From the interference pattern it is possible to calculate the resulting CD as [23]:

$$D = \frac{1}{c}\frac{\partial N_{\text{PCF}}}{\partial \lambda}, \tag{4}$$

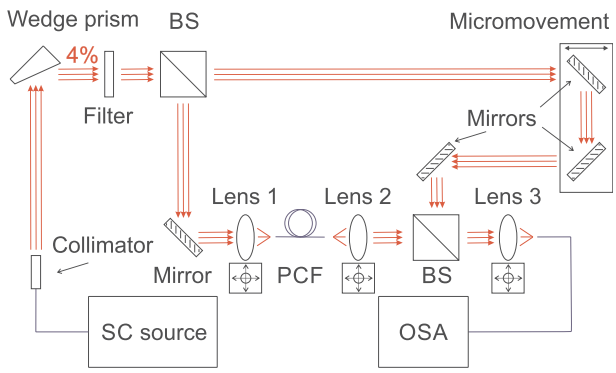


**Fig. 7.** Interferometric setup for the measurement of the CD curve using a broadband source. Supercontinuum source (SC source), beam splitter (BS), optical spectrum analyzer (OSA).

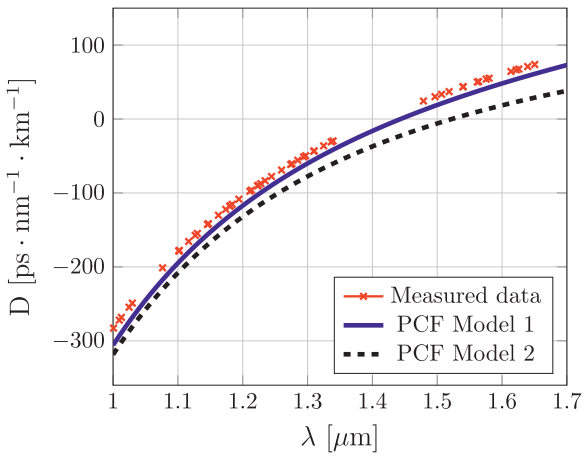


**Fig. 8.** Simulated and measured CD curve of sample PCF. Simulation results are based on Model 1 and Model 2 using PBG-08$_1$ glass material.

$$N_{\mathrm{PCF}} = \frac{2\Delta l - \Delta l_{\mathrm{lenses}}}{l_{\mathrm{PCF}}} + 1 \tag{5}$$

where $N_{\mathrm{PCF}}$ is given as the group refractive index of PCF, $l_{\mathrm{PCF}}$ is the PCF length, $\Delta l$ is the optical path difference between the measurement and reference arms, $\Delta l_{\mathrm{lenses}}$ is the additional optical path difference caused by the signal passing through the lenses in the measurement arm.

To validate our PCF model (Model 1 using PBG-08$_1$) measured and calculated CD curves are compared. We illustrate the results in Fig. 8.

The ZDWL obtained from our CD measurement is $ZDWL_{\mathrm{meas}} = 1.412$ µm, while the ZDWL obtained from the simulation Model 1 using PBG-08$_1$ is $ZDWL_{\mathrm{sim}} = 1.443$ µm. This result is in agreement with the model. The 0.031 µm blue shift of the measured CD curve is caused by the unknown lens thickness at the point of the signal as well as imprecision in determining the wavelength of interference maximum.

### 4.2. Effective mode area

The second validation of the PCF model is done via $A_{\mathrm{eff}}$ of the sample PCF, which is obtained by measuring the PCF mode-field distribution in the near-field. Effective mode area is calculated using Eq. 3. The measurement setup can be seen in Fig. 9.

The laser signal at 1.55 µm (ID Photonics Cobrite DX4) is coupled into our sample PCF with lens 1 (Thorlabs C660TME-C, 40% coupling efficiency). The PCF output signal is then collimated using lens 2 (Thorlabs C660TME-C) and propagates to the BS (Thorlabs PBSW-1550). 50% of the signal is captured with the CCD camera (Gentec Beamage 4 M IR), the other 50% is deflected and is not used.

For correct measurement of the near-field distribution, PCF end-facet must be positioned precisely in the focus of lens 2 and the magnification of lens 2 must be determined. To ensure that, we use laser 2 (ID Photonics Cobrite DX4) with lens 3 (convex lens with focus distance = 5 cm) that serves to illuminate the PCF end-facet. The image of the air-hole structure of the sample PCF is then reflected back on the BS and to the CCD camera. Therefore, when we can see the sharp image of the PCF air-hole structure on the CCD camera, we are sure that the PCF is in the focus of lens 2. The magnification of the lens 2 can be then easily determined from the image captured by the CCD camera, as the reflected image of the air-hole structure passes through lens 1 and BS, it is subjected to same magnification as mode-field distribution of the PCF and the dimensions of the PCF air-hole structure are already known.

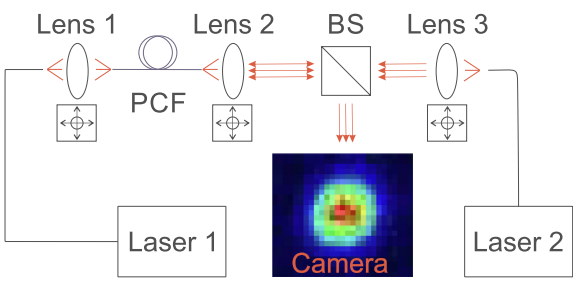


**Fig. 9.** Setup for measuring the mode-field distribution of sample PCF in the near-field.

Using this method we are able to obtain $A_{\mathrm{eff_{meas.}}} = 7.87$ µm$^2$ at $\lambda = 1.550$ µm, which is in good agreement with the data obtained from the Model 1 with $A_{\mathrm{eff}} = 7.92$ µm$^2$. The small 0.05 µm$^2$ difference in $A_{\mathrm{eff}}$ is contributed to the finite resolution of the camera (2048 × 2048 px), inherent noise of the camera and the uncertainty in determining the focus of the PCF end-facet.

## 5. Discussion

From the presented results, it is clear that to achieve accurate PCF characterization we need to transfer the exact PCF air-hole structure into the proposed model (Model 1). Defining a PCF by using uniform parameters (Model 2) is not suitable as the model does not include all deformations of shape, size, or position of the air-holes.

We have shown that in some cases an OLM with 400x magnification is sufficient to obtain a detailed enough image of the PCF air-hole structure. Using OLMs can simplify the model preparation process and make it less cost-intensive.

The precise characterization of the RI curve of studied PCF glass material has proven to be critical. In this paper, we have studied a sample PCF made from experimental lead-silicate glass. As shown in Fig. 4 and Fig. 5, even small RI variations in the order of $10^{-3}$ can produce significant differences in the resulting CD curve and 0.077 µm ZDWL shift. On the other hand, typically well known glass materials are used, such as silica glasses, which have already been precisely characterized and then the RI measurement step can be omitted.

Now we want to emphasize the importance of the precise PCF modeling in the context of a practical application. For this purpose, SCG was calculated using [24] with the parameters of Model 1 and Model 2. The sample PCF nonlinear coefficient $\gamma$ and the propagation constants $\beta_2$ - $\beta_m$ at the pump wavelength were calculated. $\beta_2$ can be obtained using Eq. 2, or derived from the models, while $\beta_3$ - $\beta_m$ are calculated by the derivation of subsequent $\beta$ as [22]:

$$\beta_m = \frac{\partial^m \beta}{\partial \omega^m}, \qquad (m = 1, 2, 3, \ldots) \tag{6}$$

where $\omega$ is the central frequency of the pump pulse spectrum.

The nonlinear coefficient $\gamma$ is calculated as [22]:

$$\gamma = \frac{2\pi n_2}{\lambda A_{\mathrm{eff}}} \tag{7}$$

where $n_2$ is the nonlinear refractive index; $n_2 = 4.3 \cdot 10^{-19}$ m$^2$/W (measured at $\lambda = 1.240$ µm) for PBG-08$_1$ glass [25]. $A_{\mathrm{eff}}$ is calculated using the COMSOL simulation for a particular wavelength and the PCF model. We consider the input pulse duration $t = 400$ fs with 30 kW peak power and 20% PCF coupling efficiency. A comparison of the derived $A_{\mathrm{eff}}$ and $\gamma$ is presented in Table 3.

Considering the ZDWL results shown in Fig. 6 (Model 1 = 1.445 µm and Model 2 = 1.522 µm with PBG − 08$_1$) and based on the values obtained with Model 2 it would lead to the assumption that optimal SCG could be achieved with sources centered at around 1.575 µm region. We have confirmed this by calculating SCG with such source and using values in Table 3. We could observe the SCG formation starting at 3 cm PCF length and fully forming at 4 cm PCF length with SCG spanning from 0.860 to 2.900 µm. However, for the same setup and with 4 cm of real drawn PCF (PCF model 1) we can observe SCG spanning only from 1.150 to 2.600 µm.

**Table 3**
Calculated $A_{\text{eff}}$ and $\gamma$ of sample PCF. Results are calculated for two PCF models considering PBG-08$_1$ glass material.

| | $\lambda$ = 1.450 μm | $\lambda$ = 1.575 μm |
|---|---|---|
| $A_{\text{eff model 1}}$ [μm$^2$] | 7.82 | 8.11 |
| $A_{\text{eff model 2}}$ [μm$^2$] | 7.10 | 7.20 |
| $\gamma_{\text{model 1}}$ [W$^{-1}$ km$^{-1}$] | 223.00 | 211.51 |
| $\gamma_{\text{model 2}}$ [W$^{-1}$ km$^{-1}$] | 262.44 | 242.09 |

To effectively pump real post-draw PCF, a laser source centered at 1.450 μm must be used, which produces SCG spanning from 0.600 to 2.900 μm with using only 3.5 cm of PCF. For practical applications, it is thereby necessary to use precise PCF modeling technique.

## 6. Conclusion

We presented an easy straightforward technique to obtain an accurate model of the real post-draw PCF, which gives reliable outputs for subsequent applications. The advantage of our approach is in time and cost saving without the need for a detailed experimental measurement campaign. In many cases, where the PCF glass material is already known only a several centimeters long PCF segment is all that is required to construct the accurate PCF model. Additionally, our PCF model (Model 1) was verified by CD and mode effective area measurements.

We then compared our accurate PCF Model 1 to a commonly used simplified model (Model 2) considering a sample lead-silicate hexagonally-structured PCF. We calculated the CD curve, $\gamma$ and $A_{\text{eff}}$ for both PCF models. We show a ZDWL shift of 0.077 μm between the two models and even 0.450 μm between the two presented RI curves. An impact on a selected application of supercontinuum generation is discussed showing that considering simplified Model 2 can lead to the use of non-optimal laser pump and therefore narrow SCG spanning only 1.150–2.600 μm as compared to the Model 1 with SCG spanning 0.600–2.900 μm.

These differences in model outputs illustrate the imprecision that occurs when even seemingly reasonable simplification of the PCF structure is considered (Model 2). The model differences in CD, $A_{\text{eff}}$ and SCG highlight the need to use real post-draw PCF design with all air-hole distortions and to define glass RI with the precision of at least $10^{-4}$.

## CRediT authorship contribution statement

**Dmytro Suslov:** Methodology, Software, Investigation, Writing - original draft, Visualization. **Matěj Komanec:** Validation, Resources, Writing - review & editing, Supervision. **Tomáš Němeček:** Software, Validation, Investigation, Writing - review & editing. **Jan Bohata:** Validation, Investigation, Writing - review & editing. **Stanislav Zvánovec:** Validation, Resources, Writing - review & editing, Supervision.

## Declaration of Competing Interest

The authors declare that they have no known competing financial interests or personal relationships that could have appeared to influence the work reported in this paper.

## Acknowledgement

This research was supported by the CTU in Prague grant SGS17/182/OHK3/3T/13 and by the project of the Ministry of Industry and Trade of the Czech Republic, TRIO FV10519.

## References

[1] J.H.V. Price, T.M. Monro, H. Ebendorff-Heidepriem, F. Poletti, P. Horak, V. Finazzi, J.Y.Y. Leong, P. Petropoulos, J.C. Flanagan, G. Brambilla, X. Feng, D.J. Richardson, Mid-IR supercontinuum generation from nonsilica microstructured optical fibers, IEEE J. Sel. Top. Quantum Electron. 13 (3) (2007) 738–749.
[2] L.E. Hooper, P.J. Mosley, A.C. Muir, W.J. Wadsworth, J.C. Knight, Coherent supercontinuum generation in photonic crystal fiber with all-normal group velocity dispersion, Opt. Express 19 (6) (2011) 4902–4907.
[3] O. Frazão, J.L. Santos, F.M. Araújo, L.A. Ferreira, Optical sensing with photonic crystal fibers, Laser Photon. Rev. 2 (6) (2008) 449–459.
[4] A.M. Cubillas, J. Hald, J.C. Petersen, High resolution spectroscopy of ammonia in a hollow-core fiber, Opt. Express 16 (6) (2008) 3976–3985.
[5] K.S. Hong, H.C. Park, B.Y. Kim, I.K. Hwang, W. Jin, J. Ju, D.I. Yeom, 1000nm tunable acousto-optic filter based on photonic crystal fiber, Appl. Phys. Lett. 92 (3) (2008) 031110.
[6] K. Saitoh, M. Koshiba, T. Hasegawa, E. Sasaoka, Chromatic dispersion control in photonic crystal fibers: application to ultra-flattened dispersion, Opt. Express 11 (8) (2003) 843–852.
[7] A. Ferrando, E. Silvestre, P. Andrés, J.J. Miret, M.V. Andrés, Designing the properties of dispersion-flattened photonic crystal fibers, Opt. Express 9 (13) (2001) 687–697.
[8] S. Xing, D. Grassani, S. Kharitonov, A. Billat, C.-S. Brés, Characterization and modeling of microstructured chalcogenide fibers for efficient mid-infrared wavelength conversion, Opt. Express 24 (9) (2016) 9741–9750.
[9] E.N. Fokoua, D.J. Richardson, F. Poletti, Impact of structural distortions on the performance of hollow-core photonic bandgap fibers, Opt. Express 22 (3) (2014) 2735–2744.
[10] M.J. Li, J.A. West, K.W. Koch, Modeling effects of structural distortions on air-core photonic bandgap fibers, J. Lightwave Technol. 25 (9) (2007) 2463–2468.
[11] G.T. Jasion, F. Poletti, J.S. Shrimpton, D.J. Richardson, Volume manufacturing of hollow core photonic band gap fibers: challenges and opportunities, Optical Fiber Communication Conference, Optical Society of America, 2015page W2A.37.
[12] M. Zghal, R. Cherif, Impact of small geometrical imperfections on chromatic dispersion and birefringence in photonic crystal fibers, Opt. Eng. 46 (12) (2007).
[13] G.T. Jasion, S.R. Sandoghchi, Y. Chen, N.V. Wheeler, T. Bradley, N. Baddela, J. Hayes, M. Petrovich, D.J. Richardson, J.S. Shrimpton, F. Poletti, Novel fluid dynamics model to predict draw of hollow core photonic band-gap fibres, in: 2014 The European Conference on Optical Communication (ECOC), 2014, pp. 1–3.
[14] F. Poli, A. Cucinotta, S. Selleri, Hotonic Crystal Fibers: Properties and Applications, Springer, 2007.
[15] I. Kaminow, T. Li, A.E. Willner, Optical fiber telecommunications VA: systems and networks, Elsevier, 2008.
[16] G. Stepniewski, R. Kasztelanic, D. Pysz, M. Klimczak, R. Buczynski, Temperature sensitivity of chromatic dispersion in nonlinear silica and heavy metal oxide glass photonic crystal fibers, Opt. Mater. Express 6 (8) (2016) 2689–2703.
[17] W. Sellmeier, Zur erklärung der abnormen farbenfolge im spectrum einiger substanzen, Ann. Phys. 219 (6) (1871) 272–282.
[18] Advanced Optics SCHOTT AG. Optical glass catalogue, 2018.
[19] J. Rheims, J. Köser, T. Wriedt, Refractive-index measurements in the near-IR using an Abbe refractometer, Meas. Sci. Technol. 8 (6) (1997) 601–605.
[20] P.G. Ciarlet, J.L. Lions, General preface, Finite Element Methods (Part 1), Handbook of Numerical Analysis, vol. 2, Elsevier, 1991.
[21] P.G. Ciarlet, J.L. Lions, General preface, Finite Element Methods (Part 2), Numerical Methods for Solids (Part 2), Handbook of Numerical Analysis, vol. 4, Elsevier, 1996.
[22] G. Agrawal, Nonlinear Fiber Optics. Optics and Photonics, Elsevier Science, 2012.
[23] P. Hlubina, M. Szpulak, D. Ciprian, T. Martynkien, W. Urbańczyk, Measurement of the group dispersion of the fundamental mode of holey fiber by white-light spectral interferometry, Opt. Express 15 (18) (2007) 11073–11081.
[24] J.R. Taylor, J.M. Dudley, Supercontinuum Generation in Optical Fibers, Cambridge University Press, 2010.
[25] G. Sobon, M. Klimczak, J. Sotor, K. Krzempek, D. Pysz, R. Stepien, T. Martynkien, K.M. Abramski, R. Buczynski, Infrared supercontinuum generation in soft-glass photonic crystal fibers pumped at 1560 nm, Opt. Mater. Express 4 (1) (2014) 7–15.

## 4.2 Low-loss and low-back reflection hollow-core to standard fiber interconnection

Reference paper:

M. Komanec, D. Suslov, S. Zvánovec, Y. Chen, T. Bradley, S.R. Sandoghchi, E.R. Numkam Fokoua, G.T. Jasion, M.N. Petrovich, F. Poletti, D.J. Richardson, R. Slavík, "Low-Loss and Low-Back-Reflection Hollow-Core to Standard Fiber Interconnection" *IEEE Photonics Technology Letters*, 2019, 31(10), 723-726. ISSN 1041-1135.

Relevance to the thesis:

In this paper we demonstrate a new coupling method leading to a permanent SMF-to-PBGF interconnection. The new interconnection technique is based on a fiber-array technology and uses GRIN multimode fiber (OM1) as the MFA. A GRIN fiber segment is spliced to the SMF and glued in the fiber-array. Then the fiber-array is polished to a defined length (modifying the GRIN fiber length) and, subsequently, the resulting MFD at MFA output. HCF is precisely cleaved and then glued in a second fiber-array while ensuring that the glue does not get into the HCF microstructure. Both fiber-arrays are then aligned together for efficient coupling and glued using a fast curable UV glue. Since glue is cured under low temperatures, it is possible to utilize ARC to suppress the Fresnel losses and back reflection. This method was demonstrated on the SMF-to-PBGF-to-SMF sample showing IL = 0.3 dB per interconnection (state-of-the-art at the time, which we then improved upon in further publications) and back reflection of -30 dB. The sample showed the same results for both direction of propagation, which was reached by low excitation of HOMs. This result served as an important step in developing a record-low loss coupling and interconnection for future NANFs.

# Low-Loss and Low-Back-Reflection Hollow-Core to Standard Fiber Interconnection

M. Komanec, D. Suslov, S. Zvánovec, Y. Chen, T. Bradley, S. R. Sandoghchi, E. R. Numkam Fokoua, G. T. Jasion, M. N. Petrovich, F. Poletti, D. J. Richardson, and R. Slavík

***Abstract*— We present a new approach to permanently inter-connect hollow-core fiber (HCF) to solid-core fiber, which does not involve fusion splicing. Our approach is based on a modification of the glue-based fiber-array technology routinely used for fiber pigtailing of planar lightwave circuits. The resulting interconnection provides for a low insertion loss due to the fact that the HCF microstructure is not deformed during the gluing (low temperature) process that is almost impossible to achieve with the standard (high temperature) fusion splicing method. Furthermore, this low-temperature technique enables the deposition and preservation of thin films deposited at the solid-to-hollow core fiber interface, allowing for additional functionality without the introduction of extra losses or any increase in complexity. To demonstrate this, we have applied an anti-reflection (AR) coating. A further feature of our approach is the ability to control very precisely the length of the graded-index (GRIN) fiber mode field (MF) adapter inserted in between the standard single-mode fiber (SMF-28) and the HCF. We show experimentally how the length of the GRIN fiber MF adapter influences the coupling between the SMF-28 and the fundamental as well as the higher-order modes of the HCF. We coupled between SMF-28 [10 $\mu$m mode field diameter (MFD)] and the fundamental mode of a 19-cell hollow-core photonic bandgap fiber (HC-PBGF, 21.1 $\mu$m MFD) with the lowest-ever reported insertion loss of 0.30 dB per interface.**

***Index Terms*— Optical components, optical fiber connecting, optical fibers.**

## I. Introduction

HOLLOW-CORE fibers such as hollow-core photonic bandgap fibers (HC-PBGFs) offer many advantages over conventional solid-core fibers due to the strongly reduced interaction of the guided light with the glass material. Examples of the benefits of this are the extremely low fiber non-linearity, low and stable [1] signal latency, the possibility to construct long-length gas cells [2], etc.

Manuscript received December 11, 2018; revised February 9, 2019; accepted February 22, 2019. Date of publication March 4, 2019; date of current version May 7, 2019. This work was supported in part by the Czech Technical University (CTU) in Prague under Grant SGS17/182/OHK3/3T/13, in part by the Optoelectronics Research Centre (ORC), University of Southampton, U.K., RAEng (Senior Research Fellowship - RCSFR1718\6\15), and in part by the Engineering and Physical Sciences Research Council (EPSRC) under Grant EP/P030181/1. *(Corresponding author: M. Komanec.)*

M. Komanec, D. Suslov, and S. Zvánovec are with the Faculty of Electrical Engineering, Czech Technical University in Prague, 16627 Prague, Czech Republic (e-mail: komanmat@fel.cvut.cz).

Y. Chen, T. Bradley, S. R. Sandoghchi, E. R. Numkam Fokoua, G. T. Jasion, M. N. Petrovich, F. Poletti, D. J. Richardson, and R. Slavík are with the Optoelectronics Research Centre, University of Southampton, Southampton SO17 1BJ, U.K.

Color versions of one or more of the figures in this letter are available online at http://ieeexplore.ieee.org.

Digital Object Identifier 10.1109/LPT.2019.2902635

A key property of any optical fiber is attenuation. In HC-PBGF the attenuation is defined principally by the fiber design. The common forms are the so-called 7-cell and 19-cell designs (made by removing 7 and 19 glass capillaries respectively to form the core in the preform from which the fiber is subsequently drawn). 7-cell HC-PBGFs typically have smaller cores (and mode field diameters, MFDs) and higher attenuation than 19-cell HC-PBGFs due to the increased interaction between the guided mode and the glass core surround (cladding). However, 7-cell HC-PBGF remains popular as it can be more straightforwardly interconnected to SMF-28 since both have a similar MFD. By contrast, when interconnecting 19-cell HC-PBGF [3] to SMF-28 there is a significant mismatch in MFD that needs to be managed e.g., using a mode field (MF) adapting bridge fiber.

Whilst generally operating in the single-mode regime both, 7-cell and 19-cell HC-PBGFs are inherently multi-moded, making the interconnection with SMF-28 prone to the unwanted coupling of part of the energy into higher-order modes (HOMs). This is highly undesirable in most applications, as it causes multi-path interference (MPI). To avoid this unwanted effect, the MFD and the MF profile of the fundamental modes of both interconnecting fibers must be very well matched; this is also needed to minimize the insertion loss (IL) of the interconnection.

There is sometimes an inconsistency in the literature when reporting insertion loss measurements for SMF-28-HC-PBGF interconnections. In some cases, the signal from the SMF-28 is coupled into the HC-PBGF and the power at the HC-PBGF output (total power in all of the excited guided modes) is measured. However, this does not represent the coupling loss between the fundamental mode of the SMF-28 and HC-PBGF. Moreover, due to multi-mode nature of HC-PBGFs, such measurements typically do not yield symmetric insertion loss values, i.e. the measured IL is different depending on whether the signal is propagating from the SMF-28 into the HC-PBGF, or vice-versa [4]. To properly characterize the coupling between the two fundamental fiber modes, it is important to measure only the power in the fundamental mode of HC-PBGF.

Apart from mitigating MPI and minimizing IL, the remaining challenges for hollow-core to solid-core fiber interconnection are the relatively strong Fresnel back-reflection and distortion of the HC-PBGF microstructure during the splicing process.

1041-1135 © 2019 IEEE. Personal use is permitted, but republication/redistribution requires IEEE permission.
See http://www.ieee.org/publications_standards/publications/rights/index.html for more information.



Authorized licensed use limited to: CZECH TECHNICAL UNIVERSITY. Downloaded on January 21,2021 at 14:03:23 UTC from IEEE Xplore. Restrictions apply.

Regarding the solid-core to hollow-core interconnection IL, the best result reported up to date is 0.3 dB [5]. This result, however, was not achieved using standard SMF-28, but a custom-made large mode area single-mode fiber. The insertion loss was measured for a HC-PBGF interconnected to SMF-28 fiber at both ends. Both interconnections exhibited a loss of 0.3 dB, confirming efficient coupling into the fundamental mode of the HC-PBGF. An anti-reflection (AR) coating was deposited on the large mode area fiber and this reduced the back-reflection to −31 dB at 1550 nm. The connection [5] was housed in a connector-style arrangement. This result is impressive and gives a benchmark as to how a coupling loss and back-reflection can be achieved with AR coatings. The main areas of improvements, however, are: (i) how to realize the low-loss connection with SMF-28, and (ii) how to hermetically seal the interconnection to avoid any degradation in the HCF loss with time (e.g., humidity-caused increase of attenuation).

Back-reflections can also be reduced by splicing angle-cleaved fibers to HC-PBGFs. The main drawback of this approach so far is in the relatively high level of IL > 3 dB [6] when 19-cell HC-PBGF was used (although an excellent −60 dB level of back-reflection was achieved). With further refinement a reduced IL of 1-2 dB with a slight compromise in back-reflection (−50 dB) was reported [7]. The main challenges of this approach are the difficulty in reliably achieving accurate angle cleaves on such delicate structures and the high sensitivity of the IL to the cleave quality.

In this letter, we demonstrate a novel approach for low-loss, low back-reflection and highly-efficient fundamental-mode coupling between SMF-28 fiber and HC-PBGF. Our approach is based on fiber-array (FA) interconnection technology [8] which can be used to create a robust and permanent HC-PBGF to SMF-28 interconnection, whilst at the same time hermetically sealing the end-facet of the HC-PBGF.

We incorporate a graded-index (GRIN) fiber based MF adapter and demonstrate how sensitive low-loss coupling between the SMF-28 and the fundamental mode of the HC-PBGF is to the precise length of the GRIN fiber used. We achieved ILs as low as 0.30 dB between the fundamental modes of the two fibers (a record value); with a reduced back-reflection loss of −30 dB. We also characterized the level of MPI and measured the polarization-dependent loss.

## II. Modified Fiber-Array Technology

Our approach is based on the FA assembly technique, which is a well-established method to pigtail photonic lightwave circuits (PLCs) with solid-core optical fibers. The fibers are first glued into a V-groove array, which is then glued onto the PLC end-facet. Adaptation is required to apply this basic approach to the case of HC-PBGF to solid-core fiber interconnection and a schematic of the modified FA assembly is depicted in Fig. 1 along with the principle of MF adaptation using a GRIN fiber segment.

First we use a 1-channel FA for the solid-core fiber and MF adaptation, we fusion splice GRIN fiber to the end of the input

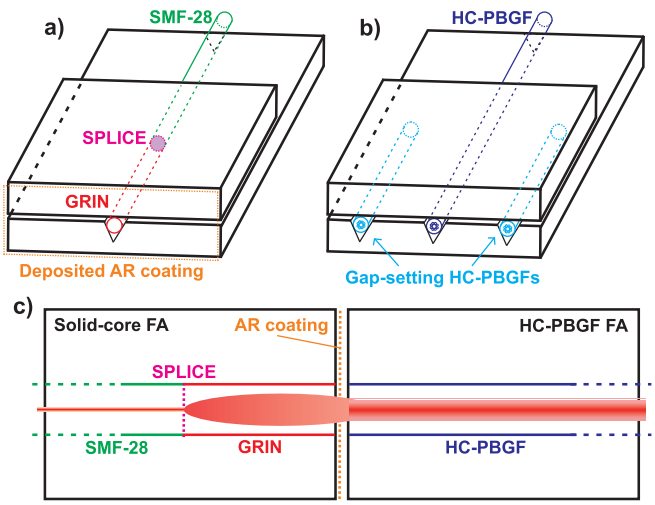


Fig. 1. Illustration of the developed 1-channel FA, a) containing SMF-28 spliced on GRIN, with the GRIN length precisely polished and with a subsequently deposited AR coating, b) containing HC-PBGF inserted and aligned with the FA end-facet. Two short segments of the same-diameter HC-PBGF are used to set the vertical gap size, c) with a schematic of the MF propagation and MF matching at the GRIN-HC-PBGF interface.

SMF-28. This MF adaptation technique has previously been used to make connectors for high power laser applications [9] in which a large MFD (and thus lower power density) is required at the point of interconnection. We cleave the GRIN fiber to a length longer than the target length and insert the spliced SMF-28 and GRIN segment into the V-groove before gluing it in place. Finally, we polish the fiber-array end-face until the desired GRIN length is achieved. This process allows for very precise control of the GRIN fiber length ($\mu$m-level), which is essential for low-loss interconnection, as we shall show later. Subsequently, for this proof-of-principle demonstration, we deposit a simple $TiO_2/SiO_2$ 2-layer AR coating on the GRIN end-facet (see the SMF-28-GRIN component in Fig. 1a). The AR coating had the minimum reflection of −32 dB at 1600 nm and a 3-dB bandwidth of 60 nm.

Simulations (ray-tracing in ZEMAX) indicated that the best commercially available GRIN fiber has a core diameter of 62.5 $\mu$m (standard OM1 graded-index multi-mode fiber). For a fully-collimating (quarter-pitch, length 265 $\mu$m) GRIN, it gives MFD of 24.6 $\mu$m, which is close to the MFD of the fundamental mode in HC-PBGF.

HC-PBGF cannot be polished in the V-groove in the same way as the solid-core GRIN fiber because of fear of damage to the delicate microstructure and ingression of polishing products. Thus, we modified the FA assembly procedure for HC-PBGF, which also takes into account the fact that HC-PBGFs generally have non-standard outer diameters which can vary from HC-PBGF sample to sample. The FA is a 1-channel type, but includes three V-grooves. The two side V-grooves are used to set the vertical gap between the upper and lower blocks of the FA by using HC-PBGF segments made of the same fiber (same diameter) as that to be used in the interconnection. At this stage, we intentionally leave the central V-groove empty. Subsequently, the HC-PBGF FA


Authorized licensed use limited to: CZECH TECHNICAL UNIVERSITY. Downloaded on January 21,2021 at 14:03:23 UTC from IEEE Xplore. Restrictions apply.

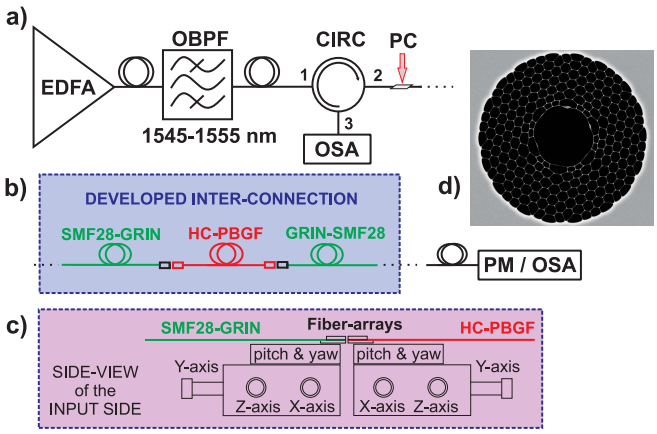


Fig. 2. Measurement configuration including a) input signal generation, b) developed interconnection with output power/spectral measurement, c) side-view of the alignment apparatus, and d) 19-cell HC-PBGF structure. EDFA - Erbium-doped fiber amplifier, OBPF - optical bandpass filter, CIRC - circulator, PC - polarization controller, GRIN - graded-index fiber MF adapter, PM - power meter, OSA - optical spectrum analyzer.

is polished and cleaned. After that, we insert a freshly cleaved HC-PBGF into the central V-groove and precisely align its end-face with the front edge of the FA (see the HC-PBGF component in Fig. 1b).

## III. Measurement Setup

The HC-PBGF used in our experiments was an in-house made 19-cell HC-PBGF with a 230 $\mu$m outer diameter and a 31.4 $\mu$m central air-hole diameter. The MFD of the fundamental mode was calculated (in COMSOL) to be 21.1 $\mu$m at 1550 nm. Calculated interconnection loss between the calculated shape of the HC-PBGF mode and a Gaussian beam of 21.1 $\mu$m (ideal) and 24.6 $\mu$m (our quarter-pitch GRIN lens) was 0.13 dB and 0.23 dB, respectively. We prepared two samples, having 10 m and 50 m HC-PBGF lengths, and made interconnections to SMF-28 fiber pigtails at each side.

For precise alignment, the FAs were placed on 5-axis micropositioning stages (X,Y,Z, pitch, and yaw), as shown in Fig. 2. We used a stabilized Erbium-doped fiber amplifier (EDFA) as a broadband light source. The EDFA output (ASE) was coupled into an optical bandpass filter (OBPF) with 10 nm bandwidth. The light then passed through a circulator (CIRC), a fiber polarization controller (PC), and the first SMF28-GRIN-HC-PBGF. After the HC-PBGF sample, the signal was coupled through the second HC-PBGF-GRIN-SMF-28 (again, using 5-axis micropositioning stage) and was measured with the optical spectrum analyzer (OSA) or power meter (PM). The spectrum of the reflected signal was measured at the 3rd CIRC port.

## IV. Results

First, we measured the IL dependence on the GRIN length. Our preliminary experimental results (not shown here) indicated that the optimum GRIN length is slightly longer than that expected from the theoretical analysis. We used five pairs of GRIN-SMF-28 FA with the 2-layer ARC and

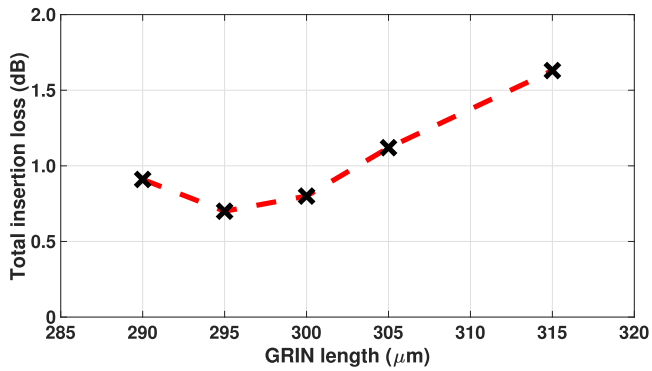


Fig. 3. Dependence of total insertion loss of the whole SMF-GRIN-HC-PBGF-GRIN-SMF component on the GRIN fiber MF adapter length (the same GRIN length was always used on both sides), utilizing a 10-m long 19-cell HC-PBGF.

GRIN lengths (the same lengths in each pair) of 290, 295, 300, 305 and 315 $\mu$m, respectively. The GRIN lengths were measured using an optical microscope, measuring the splice to end-facet distance with a measurement uncertainty of $\pm 1\,\mu$m. The measured IL for the whole SMF-28-GRIN-HC-PBGF-GRIN-SMF-28 assembly is plotted in Fig 3.

The minimum IL was obtained with a GRIN length of 295 $\mu$m. It is worth noting that deviation as little as 5 $\mu$m from the optimum GRIN length leads to the insertion loss increase of $>$0.1-0.2 dB (see Fig. 3). A similar level of insertion loss increase is expected (based on a numerical analysis) in the case of longitudinal or transverse misalignment of $\sim$5 $\mu$m. Note that besides slightly increased insertion loss, any misalignment will result as well in stronger unwanted HOM excitation.

Besides optimizing the IL using the two 5-axes stages, we also monitored the quality of the launch into the fundamental mode by observing the transmitted signal with the OSA. Any component of power launched into HOMs presents itself as MPI and is visible as spectral ripples on the transmitted broadband spectrum measured at the OSA. This technique is simpler than conventional measurements of MPI based on the time-of-flight technique [10] or $S^2$ measurement [10], [11]. The HOMs contributing most to MPI are the $LP_{11}$ mode and the $LP_{02}$ mode with differential modal delays of 8.7 ps/m and 21.4 ps/m respectively [11]. We should be able to observe MPI from these modes in HC-PBGF with lengths up to 45 m and 18 m length respectively when operating the OSA at its highest resolution of 20 pm.

The MPI for various GRIN lengths used for the 10-m long HC-PBGF sample is shown in Fig. 4, together with the measured IL for the entire SMF28-GRIN-HC-PBGF-GRIN-SMF-28 assembly.

The minimum MPI (demonstrated as the smallest amplitude spectral ripples) was achieved for a GRIN fiber length of 295 to 300 $\mu$m (the minimum IL was achieved for the 295 $\mu$m length).

Once we optimized the optical performance, we glued the FAs together. Apart from ensuring that the connection does not move during the glue-curing process, we had also to ensure



Authorized licensed use limited to: CZECH TECHNICAL UNIVERSITY. Downloaded on January 21,2021 at 14:03:23 UTC from IEEE Xplore. Restrictions apply.

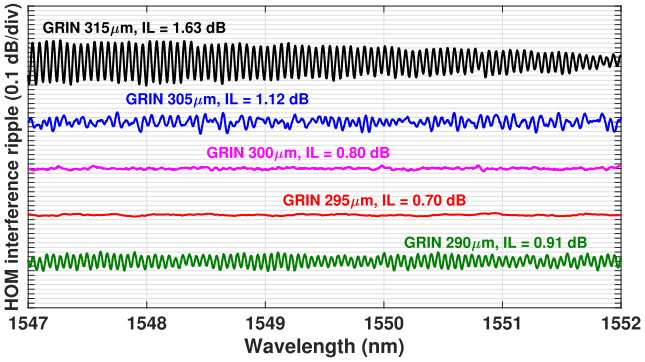


Fig. 4. HOM interference ripples in transmitted spectra for various GRIN fiber MF adapter lengths measured for the whole SMF28-GRIN-HC-PBGF-GRIN-SMF28 configuration including a 10-m long HC-PBGF.

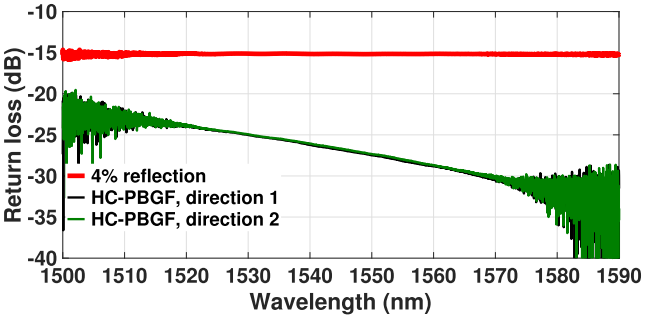


Fig. 5. Back-reflection spectra of the final component including 50-m long HC-PBGF.

that the glue does not creep into the HC-PBGF microstructured region - we used a fast ($<5$ s) UV-curable, high viscosity glue for this purpose. First, we aligned both 5-axis stages for the entire SMF-28-GRIN-HC-PBGF-GRIN-SMF-28 assembly. During the gluing, (the first interconnection followed by the second one), we observed a maximum increase in the IL per interface of 0.05 dB.

Subsequently, we interconnected a 50-m long HC-PBGF. We achieved an IL of 0.87±0.05 dB (which also includes the PDL) for the complete SMF-28-GRIN-HC-PBGF-GRIN-SMF-28 glued assembly. Considering the loss of the 50-m long HC-PBGF (4.0 dB/km), we calculated IL per connection of 0.30 dB. Figure 5 shows the measured back-reflection spectrum of the 50-m long HC-PBGF after the assembly process (without the OBPF). We observed 15 dB lower back-reflection at 1580 nm (the used ARC showed minimum reflection there) with respect to the measured 4 % reflection from a flat interface.

## V. Conclusion

In this letter we have presented for the first time a FA based approach to create a permanent hermetically sealed interconnection of HC-PBGF to SMF-28s. Our method provides signal propagation in the fundamental mode, with the signal propagating in the higher-order modes being significantly suppressed, reducing multipath propagation effects.

Using our approach, a coating can be applied to the interface. As a proof-of principle, we have reduced back-reflections by 15 dB compared to the typical silica-air interface by depositing a simple 2-layer AR coating. Apart from reducing the back-reflection, the AR coating is also expected to reduce IL by 0.17 dB per silica-air interface.

We reached best-ever reported insertion loss between SMF-28 and 19-cell HC-PBGF of 0.30 dB, confirmed both for a 10-m long and 50-m long HC-PBGF. The interconnection was reciprocal, with IL difference of only 0.03 dB for both propagation directions, confirming good coupling between fundamental modes of both fibers. Furthermore we have presented a simple approach of single-mode launch verification by monitoring MPI with a spectrum analyzer.

An additional advantage of the presented method lies is the fact that it can be straightforwardly extended to simultaneously interconnecting several (e.g., 64) HC-PBGFs with multiple SMF-28s or even with a multi-port planar lightwave circuit (e.g., a 64x64 PLC coupler).

## Acknowledgment

The data in this letter is accessible through the University of Southampton research repository (DOI: 10.5258/SOTON/D0831).

## References

[1] R. Slavík *et al.*, "Ultralow thermal sensitivity of phase and propagation delay in hollow core optical fibres," *Sci. Rep.*, vol. 5, p. 15447, Oct. 2015.

[2] N. Dadashzadeh *et al.*, "Near diffraction-limited performance of an OPA pumped acetylene-filled hollow-core fiber laser in the mid-IR," *Opt. Express*, vol. 25, no. 12, pp. 13351–13358, Jun. 2017.

[3] Y. Chen *et al.*, "Multi-kilometer long, longitudinally uniform hollow core photonic bandgap fibers for broadband low latency data transmission," *J. Lightw. Technol.*, vol. 34, no. 1, pp. 104–113, Jan. 2016.

[4] R. Thapa, K. Knabe, K. L. Corwin, and B. R. Washburn, "Arc fusion splicing of hollow-core photonic bandgap fibers for gas-filled fiber cells," *Opt. Express*, vol. 14, no. 21, pp. 9576–9583, Oct. 2006.

[5] J. W. Nicholson *et al.*, "Low-loss, low return-loss coupling between SMF and single-mode, hollow-core fibers using connectors," in *Proc. Conf. Lasers Electro-Optics (CLEO) Laser Sci. Photonic Appl.*, Jun. 2014, pp. 1–2.

[6] F. Couny, F. Benabid, and P. S. Light, "Reduction of Fresnel back-reflection at splice interface between hollow core PCF and single-mode fiber," *IEEE Photon. Technol. Lett.*, vol. 19, no. 13, pp. 1020–1022, Jul. 1, 2007.

[7] G. A. Miller and G. A. Cranch, "Reduction of intensity noise in hollow core optical fiber using angle-cleaved splices," *IEEE Photon. Technol. Lett.*, vol. 28, no. 4, pp. 414–417, Feb. 15, 2016.

[8] N. Hiroi, Y. Hashimoto, and K. Matsumoto, "Optical fiber array," U.S. Patent US 20090285533 A1, May 3, 2011.

[9] Y. Shou and J. Zhao, "Mode field expanded fiber collimator," U.S. Patent US 7920763 B1, Aug. 5, 2011.

[10] D. R. Gray *et al.*, "Complementary analysis of modal content and properties in a 19-cell hollow core photonic band gap fiber using time-of-flight and $S^2$ techniques," in *Proc. 38th Eur. Conf. Exhibit. Opt. Commun.*, Sep. 2012, pp. 1–4.

[11] D. R. Gray *et al.*, "Accurate calibration of $S^2$ and interferometry based multimode fiber characterization techniques," *Opt. Express*, vol. 23, no. 8, pp. 10540–10552, Apr. 2015.


Authorized licensed use limited to: CZECH TECHNICAL UNIVERSITY. Downloaded on January 21,2021 at 14:03:23 UTC from IEEE Xplore. Restrictions apply.

## 4.3 Low loss and high performance interconnection between standard single-mode fiber and antiresonant hollow-core fiber

Reference paper:

D. Suslov, M. Komanec, E. R. Numkam Fokoua, D. Dousek, A. Zhong, S. Zváanovec, T. Bradley, F. Poletti, D. J. Richardson, R. Slavík, "Low loss, high-performance interconnection between standard single-mode fiber and antiresonant hollow-core fiber", Scientific Reports, accepted, 2021

Relevance to the thesis:

The new coupling method/interconnection technique was further optimized and examined with a focus on the state-of-the-art NANF. In this paper we have shown an interconnection of SMF-to-NANF-to-SMF. We have presented several variants of efficient coupling using OM1 and OM2 GRIN multimode fibers as MFAs, as well as TEC-based MFA. We have identified the sources of the coupling losses, presented the theoretical limits of the SMF-to-NANF coupling for each of the proposed MFAs and, subsequently, experimentally verified them. The sources of the insertion losses have been identified to be mode-field size mismatch and shape symmetry mismatch due to the six fold symmetry of NANF, compared to the circularly symmetrical field distribution of GRIN and TEC MFAs. Furthermore, we have examined in detail HOM cross-coupling. To that end we present a quick and easy method to characterize HOMs by analyzing a broadband transmission spectrum using the Fourier transform. This gives us an evaluation of several first HOMs (given by the resolution of the optical spectrum analyzer and the length of the NANF), which are the most important as they propagate with the lowest attenuation and are, therefore, the most significant for bidirectional coupling, as well as detrimental in many practical applications. Fresnel back reflection has been again reduced using ARC. We demonstrate SMF-to-NANF interconnection with record-low IL of 0.15 dB per interconnection, which is the lowest reported value. $LP_{11}$ mode coupling is only -35 dB and Fresnel back reflection is -40 dB.

# Low loss and high performance interconnection between standard single-mode fiber and antiresonant hollow-core fiber

**Dmytro Suslov[1,*], Matěj Komanec[1], Eric R. Numkam Fokoua[2], Daniel Dousek[1], Ailing Zhong[1], Stanislav Zvánovec[1], Thomas D. Bradley[2], Francesco Poletti[2], David J. Richardson[2], and Radan Slavík[2]**

[1]Department of Electromagnetic Field, Czech Technical University in Prague, Technická 1902/2, 166 27 Prague 6, Czech Republic
[2]Optoelectronics Research Centre, University of Southampton, Southampton, SO17 1BJ, UK
[*]Corresponding author: Dmytro Suslov (email: suslodmy@fel.cvut.cz)

## ABSTRACT

We demonstrate halving the record-low loss of interconnection between a nested antiresonant nodeless type hollow-core fiber (NANF) and standard single-mode fiber (SMF). The achieved interconnection loss of 0.15 dB is only 0.07 dB above the theoretically-expected minimum loss. We also optimized the interconnection in terms of unwanted cross-coupling into the higher-order modes of the NANF. We achieved cross-coupling as low as -35 dB into the $LP_{11}$ mode (the lowest-loss higher-order mode and thus the most important to eliminate). With the help of simulations, we show that the measured $LP_{11}$ mode coupling is most likely limited by the slightly imperfect symmetry of the manufactured NANF. The coupling cross-talk into the highly-lossy $LP_{02}$ mode ($> 2000$ dB/km in our fiber) was measured to be below -22 dB. Furthermore, we show experimentally that the anti-reflective coating applied to the interconnect interface reduces the insertion loss by 0.15 dB while simultaneously reducing the back-reflection below -40 dB over a 60 nm bandwidth. Finally, we also demonstrated an alternative mode-field adapter to adapt the mode-field size between SMF and NANF, based on thermally-expanded core fibers. This approach enabled us to achieve an interconnection loss of 0.21 dB and cross-coupling of -35 dB into the $LP_{11}$ mode.

## Introduction

Hollow core fibers (HCFs) have been reported to reduce the attenuation from 1.3 dB/km a year ago[1] to the current state-of-the-art of 0.28 dB/km[2], making the prospect of obtaining an optical fiber with attenuation below that of solid silica single-mode fiber (SMF) a distinct possibility in the near future. The latest three low-loss records in HCFs (1.3 dB/km[1], 0.65 dB/km[3], and 0.28 dB/km[2]) were reported in the Nested Antiresonant Nodeless Fiber (NANF), which therefore emerges as the most promising geometry in the quest for lower losses than the SMF. Besides this potential for ultra-low attenuation, HCFs have a range of additional advantages including low latency of propagation[4], low thermal sensitivity of latency as well as accumulated phase[5], low nonlinearity[6,7], high damage threshold[8], etc., making them of interest in a wide range of applications. To fully benefit from these advantages, however, an efficient low-loss and low-back-reflection interconnection between HCFs and mainstream SMFs is needed.

Recently, we demonstrated a new permanent, low-loss SMF-HCF interconnection technique based on gluing rather than splicing[9]. Fiber gluing is a widely-used process in demanding and cost-sensitive applications including telecoms, e.g., for pigtailing of planar lightwave splitters[10]. As gluing does not require any heating of the fibers (as opposed to fusion splicing), there is no deformation to the HCF micro-structure, which otherwise increases the interconnection loss. Further, no heating means that an optical coating can be applied in between the HCF and SMF. When anti-reflective (AR) coating is deposited, it significantly reduces the unwanted 3.5% back-reflection occurring at the glass-air interface in between the air core of the HCF and the solid silica glass core of the SMF. In addition to reducing the back-reflection, it also lowers the insertion loss (by up to 3.5% that would otherwise be lost in the back-reflection). The most important aspect, however, that must be addressed to achieve low-loss SMF-HCF interconnection, is to adapt the mode-field diameter, which at 1550 nm is typically 10.4 µm for the SMF and >20 µm for low-attenuation HCF[9].

In[9], we inserted a short segment of graded-index multi-mode fiber (GRIN) in between the SMF and HCF, which served as a lens that adapted the mode field size. When complemented with the AR coating, an HCF-SMF insertion loss (IL) as low as 0.3 dB and back-reflection below -30 dB were achieved. This was demonstrated with a photonic bandgap type of HCF,

which was the state-of-the-art in terms of attenuation before the NANF emerged. These two types of HCFs are fundamentally different in their guiding mechanism (photonic bandgap guiding versus antiresonant effect guiding) as well as structure (delicate photonic bandgap with a large number of thin glass membranes versus a small number of tubes). As the antiresonant HCFs emerged as a low-attenuation solution only recently, there is only a limited number of reports on their interconnection with SMF. To the best of our knowledge, the lowest interconnection loss reported is 0.5 dB for simple SMF-NANF interconnection[11] or 1.5 dB for a more complex device (1x2 splitter,[12]).

Although the lowest-loss value reported for a HCF-SMF interconnection of 0.3 dB is acceptable for a wide range of applications, it is 0.17 dB higher than expected from simulations[9]. Additionally, there are no data on how much of the light is coupled into the HCF's higher-order modes (HOMs) in these low-loss interconnections, and (even more importantly) how and how much this can be suppressed. From the practical point of view, loss lower than 0.3 dB will be of interest in high-power applications and laser resonators. Lower unwanted coupling into HOMs is of interest in applications sensitive to modal noise, e.g., interferometry[13], precise time[14], frequency transfer[15] and even telecommunications[16],[17].

In this paper, we show a record low-loss SMF-NANF interconnection of 0.15 dB (which increases slightly to 0.16 dB when permanently glued), which is only 0.07 dB higher than the theoretically predicted minimum loss of 0.08 dB (calculated from the mode-field overlap between the field in NANF and a Gaussian field profile). This represents over 2 times improvement from the previous result in which the interconnection loss of 0.30 dB was 0.17 dB above the theoretical limit[9]. This improvement is thanks to the use of a mode-field adapter that is better matched to the mode of the HCF used. Simultaneously, we report a low-back-reflection level of -40 dB over 60 nm bandwidth thanks to a high-performance AR coating. Furthermore, we calculated and measured the coupling into the HOMs and show that: (i) the coupling magnitude to the $LP_{11}$ mode was measured to be below -35 dB (calculated value: -41 dB) and that it is likely to be limited by the symmetry of the fabricated NANF, and (ii) coupling magnitude to the $LP_{02}$ mode was measured to be below -22 dB (calculated value: -24 dB). In addition to the GRIN-based mode field adaptation, we also present a new configuration based on thermally-expanded core fibers (TECs), showing experimentally a NANF-SMF interconnection loss of 0.21 dB.

## Simulations of NANF mode field profile and higher-order modes

NANF HCF used in our experiment is of the same geometry as reported in[1], operating in the 2nd antiresonant window at 1550 nm. It has six large tubes with smaller tubes placed inside them, see Fig. 1a. The measured core diameter is 32.5 µm.

Firstly, we measured the field profile of light at the NANF output. The result together with an image of the used NANF end-face are shown in Fig. 1a. Subsequently, we simulated the fundamental mode-field profile of the NANF used in our experiments (obtained using the fiber end-face image shown in Fig.1a and technique described in detail in[18]) using COMSOL Multiphysics. Both simulated and measured mode field profiles show that NANF mode is not circularly symmetric - it actually has a six-fold symmetry, following the symmetry of the fiber microstructure. This is also visualized in Fig. 1c, where the mode field profile is plotted along the two principal axes (that are shown in Fig. 1b).

Let us consider light coupling between the NANF fundamental mode and a Gaussian-profile beam. A priori, we expect the mismatch between the circular symmetry of the Gaussian beam and the six-fold symmetry of the NANF fundamental mode to impose a fundamental limit on the achievable interconnection loss. However, the symmetry is not the only limiting factor, as we can see by analyzing the data shown in Fig. 1e, where one of the mode field profiles from Fig. 1c is fitted with a Gaussian profile. Clearly, the NANF mode field profile is not Gaussian, which is especially visible in the mode field tails, where the Gaussian profile vanishes more slowly than the profile of the NANF fundamental mode. Both of these phenomena (the non-circular symmetry and non-Gaussian mode field profile) contribute to: (i) the minimum-achievable coupling loss between a Gaussian-profile beam and the fundamental mode of NANF, and (ii) coupling into HOMs. Theoretical analysis (calculating overlap integrals between the Gaussian mode and the NANF modes) shows that the minimum coupling loss from a Gaussian beam into NANF fundamental mode is 0.08 dB, with simultaneous coupling into $LP_{02}$ mode (essentially a cross-talk) of -24 dB. Coupling into the $LP_{11}$ mode is -41 dB. The $LP_{11}$ coupling occurs due to the small deviations from the ideal symmetry (fabrication errors) of the manufactured NANF structure, this coupling would ideally be zero thanks to the different symmetries of the fundamental mode and the $LP_{11}$ mode. The attenuation of the fundamental, $LP_{11}$, and $LP_{02}$ modes (limited by confinement loss) is calculated to be $\sim$0.6 dB/km, $\sim$35 dB/km and $\sim$2100 dB/km, respectively.

## Mode field adaptation

There are two aspects to be addressed to obtain ultra-low-loss interconnection between NANF and standard SMF: 1) The differences in mode field profile between the NANF and SMF-28 and 2) the Fresnel losses and back-reflection caused by the difference in refractive indices at a glass-air interface (about 3.5% for a silica glass-air interface).

As for the mode field adaptation, we would ideally need to transform the mode field profile and size of the SMF to match those of the NANF. As discussed earlier, transforming the mode field profile is challenging due to the different symmetry

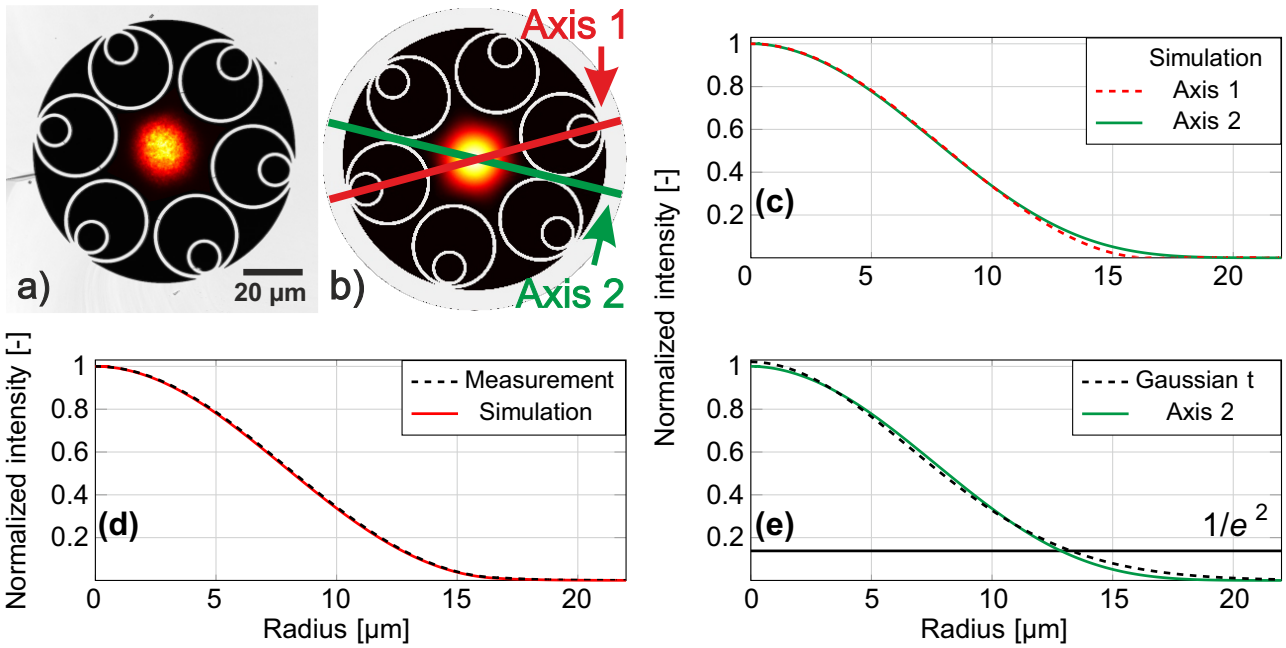


**Figure 1.** a) Measured mode field distribution at the output of NANF overlaid with the captured image of the NANF core area. b) Simulated fundamental mode field distribution overlaid with the NANF microstructure, extracted from the used NANF end-face photograph. c) Mode field profiles from (b) along the two principal axes shown in (b). d) Averaged axis 1 and 2 mode field profiles from measurement and simulation e) Mode field profile from (c) and its Gaussian fit.

(circular for SMF and six-fold for NANF) as well as the slightly different field profiles: both SMF and NANF modes are almost Gaussian, but as we have shown in Fig. 1e they do not fit the Gaussian profile perfectly. Thus, we attempt to match the mode field size only, accepting this will limit the minimum-achievable coupling loss. As shown in our theoretical analysis, this limitation is expected to be 0.08 dB (provided we generate a perfectly-Gaussian mode field profile of optimum size).

To enlarge the mode field diameter (MFD) of SMF (10.4 µm) to that of our NANF (∼24 µm), we use here two approaches: the first one uses commercially available graded-index multi-mode fiber (GRIN) as mode field adapters (MFA), the other one uses SMF-based TEC mode field adapters.

### GRIN and TEC fiber based MFAs

An optical signal that propagates from SMF to GRIN enlarges and shrinks its MFD in a periodic/sinusoidal fashion along the length of the GRIN (one period is referred to as 'one pitch'). It is therefore possible to achieve the desired MFD by controlling the length of the GRIN segment. The largest MFD is obtained when the GRIN length is at 1/4 of the pitch, which is also the length at which the output beam is collimated. In our experiment, we splice the GRIN fiber to SMF-28, put it into a single-channel glass fiber array (FA) and polish it to the desired length, which depends on the required MFD. We described this technique in detail in our previous publication[9].

We consider commercially available GRIN fibers of type OM1 (core diameter 62.5 µm, numerical aperture NA = 0.275) and OM2 (core diameter 50 µm, NA = 0.20). We used BeamProp software to model propagation through the GRIN fibers (OM1 and OM2) to get an estimate of the 1/4 pitch length as well as the output MFD. The modelling results for GRIN length in the vicinity of the 1/4 pitch (which is the region of our interest, as we show later) are shown in Fig. 2a. MFD is calculated at the $1/e^2$ of the intensity profile. We see that OM1 type GRIN provides a MFD up to 19.1 µm (at 1/4 pitch length of 260 µm), while OM2 type GRIN offers a MFD up to 23.2 µm (at 1/4 pitch length of 300 µm). The main reason OM2 provides larger MFD as compared to OM1 is its lower NA. Fig. 2b shows coupling loss between the mode generated by the GRIN MFA (which we measured in the near-field to be Gaussian) and a Gaussian mode with 24.1 µm MFD (MFD value obtained by fitting the NANF mode with a Gaussian profile). We see that OM2 should provide close to 0 dB loss for coupling into a Gaussian mode of 24.1 µm MFD for a GRIN length of 250-350 µm. Fig. 2c shows the coupling loss between the mode generated by the GRIN MFA (considered to be Gaussian) and mode of our NANF (which includes the loss due to the mode field diameter mismatch (shown in Fig. 2b) together with loss due to NANF's 6-fold symmetry and its slightly non-Gaussian field profile) with the earlier-discussed limit of 0.08 dB. However, MFD is not the only parameter of the beam leaving GRIN fiber. Unless it is at 1/4

pitch, the beam is converging (focusing) or diverging, introducing phase curvature across the mode profile. This effect is not considered in our simulations.

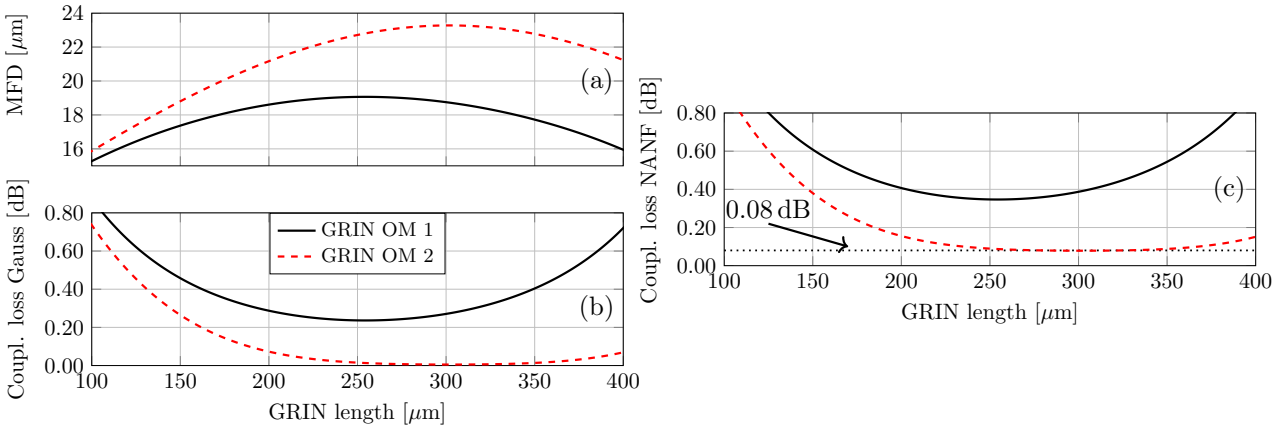


**Figure 2.** (a) Calculated MFD of OM1 (solid line) and OM2 (dashed line) type GRIN as a function of its length. (b) Coupling loss between Gaussian mode with MFD of 24.1 µm and output of GRIN mode field adapter shown in (a). (c) Coupling loss between NANF fundamental mode and output of GRIN mode field adapter shown in (a).

To overcome Fresnel losses, we use an AR coating applied on to the polished GRIN surface[9]. To deposit this coating, particular care must be given to the coating deposition temperature, as the GRIN is glued inside the FA. Glue may not withstand high temperatures used for standard thin-film coating procedures and lower deposition temperature may compromise the coating quality. This is why in our previous report, we achieved a back-reflection level of -30 dB only. Although this level of back-reflection does not degrade the interconnection loss (-30 dB back-reflection corresponds to 0.1% of transmission loss, which is negligible as compared to the expected insertion loss of 0.08 dB (1.8%) transmission loss), better back-reflection suppression would be of interest in many applications. Here, we improved the control of the AR deposition process, achieving more than 10 dB better back-reflection suppression. The AR coating is a 4-layer $TiO_2/SiO_2$ design, which allows suppression of back-reflection by up to 48 dB, with >40 dB suppression over a 60 nm bandwidth (1550 - 1610 nm), Fig. 3.

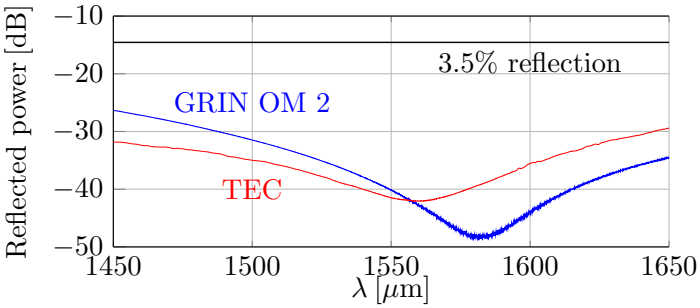


**Figure 3.** Measured back-reflection of SMF-GRIN and SMF-TEC MFAs as a function of wavelength.

TECs are commercially-available and typically provide 2-3 times magnification of the mode field size of standard SMF. We purchased TECs with mode field diameters of 20, 24, and 26 µm and a deposited AR coating of 40-dB back-reflection-level at 1550 nm as shown in Fig. 3.

## SMF-NANF interconnection characterization

### Measurement setup

As NANF can support the guidance of HOMs, we need to be cautious when measuring a single SMF-NANF interconnection to accurately characterize the coupling between the SMF and the NANF fundamental mode. This is because measuring power directly at the NANF output includes contributions from all the propagating modes and HOMs can carry an appreciable fraction of the total optical power.

One way to measure coupling between the SMF and NANF fundamental mode is to use a long length of NANF in which all HOMs are attenuated (thanks to the relatively high differential loss between the NANF fundamental mode and HOMs), obtaining only the fundamental mode power at the NANF output.

We chose another approach, using a short NANF (10 m) and performing interconnection with the SMF at both ends using a pair of identical MFAs (Fig. 4). This method allows for accurate coupling loss measurement between the fundamental modes of the two fibers[9] and also allows for estimation of the coupling efficiency into HOMs, which is not possible using a single interconnection and a long length NANF (HOMs will already be attenuated and no interference pattern will be visible). This approach provides additional means of characterization of the interconnection performance.

We took a set of GRIN and TEC MFA pairs with various mode field sizes. For each MFA pair, we aligned them with a 10 m long NANF sample and measured the total insertion loss as shown in Fig. 4. We used an Erbium-doped fiber amplifier (EDFA) operated in automatic power control mode as a broadband light source (Keyopsys KPS-BT2-C-10-LN-SA). We chose this source as it is broadband and unpolarized, avoiding effects of polarization dependent loss or interference during the alignment. The EDFA signal was filtered with a 10 nm wide optical band-pass filter (OBPF) (1545 - 1555 nm). The output of OBPF was then passed through a circulator (CIRC) to the input of the first MFA. The MFA output was precisely aligned with NANF using a 5-axis micropositioning stage (Thorlabs NanoMax MAX313D/M with pitch and yaw tilt platform APY002/M). Port 3 of CIRC enabled measurement of the back-reflection. The NANF output was aligned in a similar fashion to the second MFA.

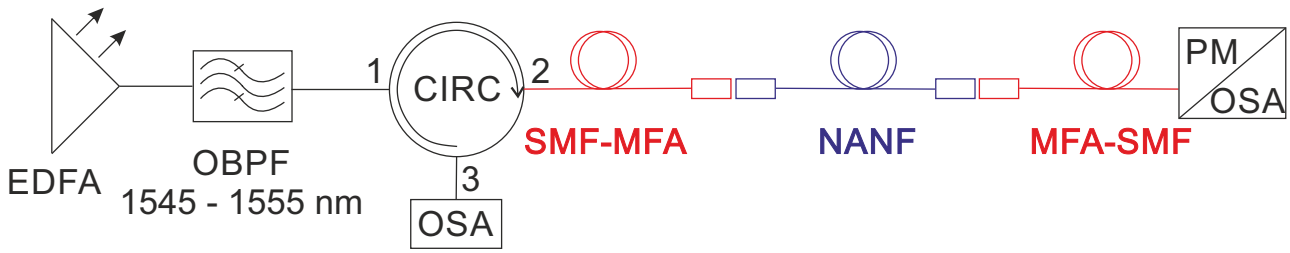


**Figure 4.** Setup used for insertion loss and back-reflection measurement of SMF-NANF-SMF interconnect for GRIN/TEC MFA pairs.

There are two important aspects of our measurement we would like to emphasise: Firstly, the use of the 5-axis stages that enables pitch and yaw alignment. Besides angular misalignment compensation, it also allows for compensation of small imperfections in the NANF cleave angle, which was always below 1° in our experiments. Secondly, the accurate calibration of transmitted power for accurate insertion loss measurement. For this, we firstly measured the transmitted power using an SMF patchcord and considered it as our reference (zero loss) value. Subsequently, we cut this patchcord in the middle and spliced the two MFAs in. Finally, we inserted the NANF sample in between the two MFAs and measure the total insertion loss of the SMF-NANF-SMF interconnections. Loss of a single SMF-NANF interconnection is then given as half of this value. This, however, means our loss measurement includes two SMF-SMF splices, which we do not account for in our analysis and which may cause up to 0.01 dB loss each. Although this makes for a slightly overestimated loss value, this is, however, at the level of accuracy of our power measurement (0.01 dB) and is thus considered negligible.

The output signal was captured using either a power meter (PM, Thorlabs S154C, to characterize insertion loss) or an optical spectrum analyzer (OSA, Yokogawa AQ6370C, to characterize back-reflection and HOM interference). This approach allows us to repeatably achieve the insertion loss of 0.15 dB within ±0.01 dB accuracy.

As analyzed in simulations, we expect some level of coupling into HOMs even when perfectly aligning the MFA with the NANF. As we mentioned, analysis of the optical spectrum of a broadband signal that propagates through NANF interconnected on both ends with SMF enables observation of coupling into HOMs. This manifests itself as an interference pattern. The light that is coupled into a HOM at the first MFA-NANF interface propagates in that mode and a fraction of it is coupled back into the fundamental mode of SMF after the second NANF-MFA interface. As the fundamental mode and the HOM have different effective refractive indices, the power recorded at the OSA shows a signature interference pattern. The amplitude of the interference pattern is proportional to the magnitude of the HOM excitation, while the interference period is proportional to the difference in propagation constants between the HOM and the fundamental mode of the NANF. Thus, we can distinguish between coupling to various HOMs too. This approach is significantly faster and easier to use than the traditional time of flight method[19], which is especially of interest during the alignment of the interconnection, in which we try to simultaneously maximize the output power (hence coupling into the fundamental mode) and minimize the HOM interference pattern amplitude observed at the OSA (to minimize coupling into HOMs). It is important to note that in practice this technique is only possible with short pieces of fiber due to the limitation of the OSA resolution. E.g. our OSA (Yokogawa AQ6370C) with a minimum resolution of 0.02 nm allows the use of 44 m long fiber.

### Interconnection loss with GRIN MFAs

In this work we consider commercially available GRIN fibers to find the best MFD match. For our NANF we found the OM2 GRIN fiber to provide the closest match with the OM1 coming the second. However, depending on the particular NANF and its corresponding MFD, different type of GRIN fiber can provide an optimal mode-field adaptation. The insertion loss of SMF-NANF interconnections was measured for each GRIN MFA pair, see Fig. 5.

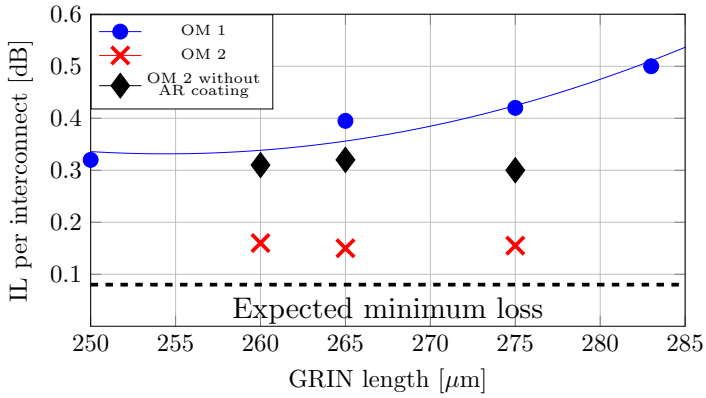


**Figure 5.** Insertion loss of SMF-28-NANF interconnect using OM1 (AR coated, blue circles, solid blue line represents fitted measurement data) and OM2 with (red crosses) and without (black diamonds) AR coating GRIN MFAs.

For OM1-based AR-coated MFA, a minimum loss of 0.32 dB was achieved with the GRIN fiber 1/4 pitch long (250 µm, Fig. 5), corresponding to the largest MFD that can be provided by the OM1 based MFA, Fig. 2. This MFD (19.1µm) is smaller than what is necessary for our NANF (Fig. 1d, MFD about 24 µm). The expected loss is 0.35 dB (Fig. 2c), which is close to the measured loss of 0.32 dB. We speculate this small discrepancy is caused by the small gap between the GRIN MFA and NANF fiber that was made during the alignment targeted to find the best value, which may have slightly enlarged the beam MFD (an effect we have not accounted for in our theoretical analysis).

The OM2-based MFA is expected to give significantly better match of the mode field size (up to 23.2 µm in 1/4 pitch GRIN length, which is achieved for 300 µm, Fig. 2a) to that of our NANF. As coupling between Gaussian fields of 23.2 µm and 24 µm MFDs leads to a negligible loss (<0.01 dB, Fig. 2b), we expect the NANF-MFA interconnection loss to be dominated by the 0.08 dB additional loss due to the symmetry and shape mismatch. Our experiments show a loss only slightly higher than expected: 0.15 dB. This was achieved for a slightly shorter GRIN length (265 µm), which however is, similarly to the optimum 1/4 pitch length, expected to bring negligible (<0.01 dB) mode field size mismatch loss, Fig. 2b. The 0.15 dB loss includes the loss of the SMF-GRIN splice. We measured this splice loss and found it to be below our power measurement resolution ($\leq$ 0.01 dB). To evaluate the effect of the AR coating on the insertion loss, we also measured IL with the GRIN-MFAs before applying the coating, Fig. 5, showing 0.15 dB increase in the IL (corresponding to 3.5%), which is exactly in line with the value expected theoretically for the air-silica glass interface.

Unlike our previous study with photonic bandgap HCFs[9] in which we concluded that the GRIN length in MFA is very critical ($\pm$5 µm length change produced almost 0.1 dB interconnection loss increase), here we see that significantly larger GRIN length variation in here-used HCF and GRIN MFA should produce negligible interconnection increase (Fig. 2c). Specifically, a change of up to $\pm$50 µm in GRIN length is predicted to produce insertion loss degradation below 0.01 dB. Experimentally, we confirm this, albeit over only a limited GRIN length variation of 15 µm. This improvement is thanks to the MFA used in combination with the HCF which was designed to ensure that the MFD of the mode generated with the quarter-pitch length GRIN is well matched to the MFD of the NANF. The larger margin on the GRIN length we show here can be achieved with cleaving[20], reducing the complexity of preparing an optimum-length GRIN MFA.

### Interconnection loss with TEC MFAs

The insertion loss for each TEC MFA pair was measured, Fig. 6. As expected, the TEC producing a MFD of 24 µm gives the lowest insertion loss. We measured 0.21 dB, which is 0.13 dB above the mode symmetry and shape mismatch limit of 0.08 dB. For 21 and 26.5 µm MFD TECs, we measured an insertion loss of 0.24 and 0.29 dB, respectively. Based on the mode size mismatch, we would expect degradation of 0.08 dB for 21 µm and 0.04 dB for 26.5 µm as compared to the optimum 24 µm. These very small values do not correlate well with the experiment (although they are of the same magnitude as measured). This can be caused either by mode shape mismatch (the TEC-MFA mode can deviate more from the Gaussian shape for larger MFDs) or by inner TEC insertion loss (larger TEC-MFA having higher insertion loss). Both of these are plausible, as larger

MFD TEC expansion requires longer heat processing and thus provides less control over the shape of the output TEC refractive index and mode field profile.

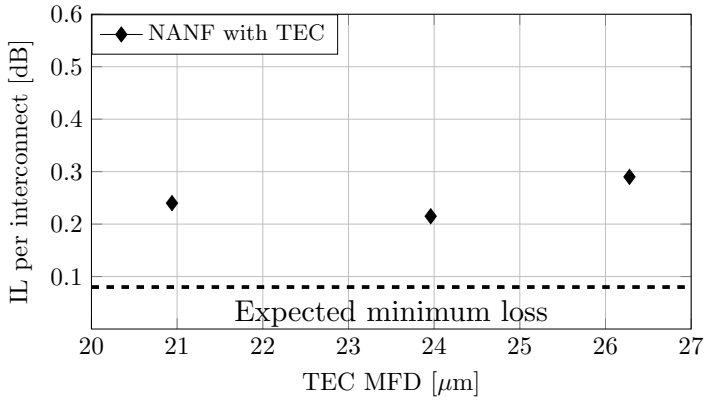


**Figure 6.** Insertion loss of SMF-28-NANF interconnect using TEC-based MFAs of various MFDs.

### Measurement of higher-order mode content

HOM interference patterns (optical spectrum measured at the SMF-MFA-NANF-MFA-SMF output) measured when using the best-performing pairs of GRIN and TEC MFAs are shown in Fig. 7.

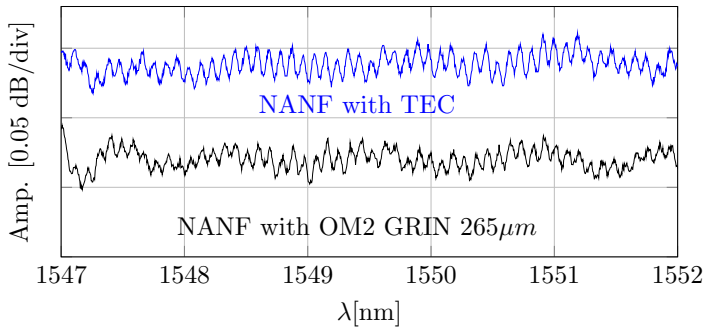


**Figure 7.** Interference pattern due to coupling into HOMs measured with the best-performing GRIN and TEC MFAs.

We see very weak (below 0.05 dB peak-to-peak) spectral oscillations of the transmitted power. The period of the oscillation is directly proportional to the propagation delay in NANF between the fundamental mode and a HOM that is being excited. Thus, a Fourier transform of the spectrum enables us to analyze the HOMs that are being excited, as we know the guided modes propagation constants from simulations. Fig. 8 shows the Fourier transform of data from Fig. 7, in which we have identified two HOMs that were predominantly excited: $LP_{11}$ (expected from simulations to be at 3.1 ps/m) and $LP_{02}$ (expected from simulations to be at 8.7 ps/m) modes. To estimate how much power is carried by these two modes, we have to find the relationship between the coupling efficiency for these HOMs and the measured quantities.

Considering only the fundamental mode and a single HOM, the detected power is:

$$|E+\alpha E\cos(\Delta\tau L)|^2 = |E|^2 + 2\alpha|E|^2\cos(\Delta\tau), \tag{1}$$

where $\alpha$ is the fraction of energy that couples into the HOM, propagates in the HOM, and then couples back into the fundamental mode. $\Delta\tau$ is the normalized differential delay between the two modes inside the NANF. $L$ is the fiber length and $E$ is the intensity of the electric field. We have neglected the term proportional to $\alpha^2$. Then, the Fourier transform of the measured data is:

$$\mathscr{F}(|E+\alpha E|^2) = |E|^2\delta(t) + \alpha|E|^2(\delta(t-\Delta\tau)+\delta(t+\Delta\tau)). \tag{2}$$

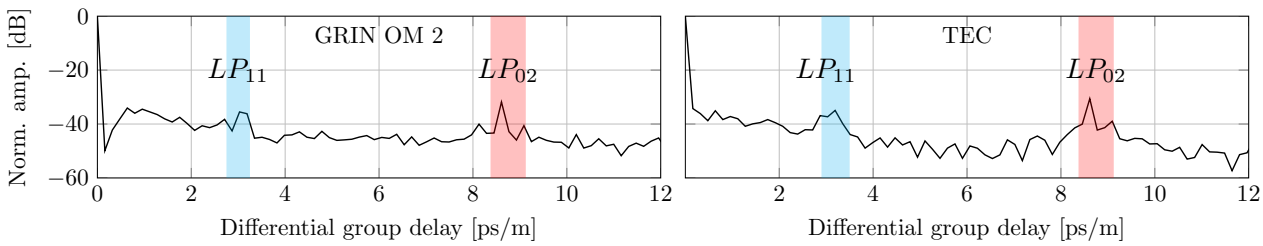


**Figure 8.** Fourier transform of spectral trances shown in Fig. 7. Positions of $LP_{11}$ and $LP_{02}$ modes expected from simulations are 3.1 and 8.7 ps/m.

In Fig. 8, we see the tone at $t - \Delta\tau$ (due to the beating between the NANF fundamental mode and the HOM) which has a normalized amplitude of $\alpha$. When taking into account the calculated attenuation of the $LP_{11}$ and $LP_{02}$ modes mentioned earlier (we need to separate the $\alpha$ contributions due to attenuation and due to coupling at the MFA-NANF interfaces) and assuming the HOM coupling is identical at both MFA-NANF interfaces, we calculated that the coupling magnitude at a single GRIN-MFA interface into the $LP_{11}$ and $LP_{02}$ modes is -35.3 dB and -21.3 dB, respectively. The $LP_{11}$ mode has negligible loss for the 10-m long NANF sample used (35 dB/km), and thus the measured tone amplitude in Fig. 8 corresponds directly to the coupling into the $LP_{11}$ mode. However, the loss for $LP_{02}$ (2100 dB/km) cannot be neglected (21 dB in 10 m of NANF) and contributes significantly to the calculated coupling efficiency into the $LP_{02}$ mode. For TECs, the $LP_{11}$ coupling is very similar, -35.0 dB, but coupling into $LP_{02}$ is slightly higher at -20.1 dB.

The measured results for coupling into the $LP_{11}$ (-35 dB) and those simulated considering slight deviation from the perfect symmetry of the used NANF sample (-41 dB) are very close, especially considering measurement and simulation errors (due to limited resolution of the trace in Fig. 8 and limited accuracy of extracting data from the measured cross-sectional fiber image used in the simulations). In light of this, we conclude that coupling into the $LP_{11}$ mode at a single MFA-NANF interconnection is most likely limited by the symmetry in the fabricated NANF rather than by other effects such as poor cleave quality. This conclusion is further supported by the fact that we measured an almost identical level of $LP_{11}$ coupling using both, GRIN and TEC MFAs, suggesting this coupling is more related to the NANF properties rather than anything else. As for the $LP_{02}$ results, we measured slightly higher values than predicted (-24 dB), suggesting the mode field profile generated in MFAs deviates slightly from a Gaussian (as the simulations were based on an MFA with Gaussian mode field profile). This slight deviation may also explain why we have not achieved an insertion loss closer to the expected value of 0.08 dB (which is also calculated considering a Gaussian-profile input beam). Furthermore, in the GRIN-MFA, the measured value of -22.3 dB is closer to the prediction (-24 dB) than the value measured for a TEC-MFA (-20.1 dB), suggesting the mode field profile at the TEC output deviates more from the Gaussian than at the GRIN-MFA output. This may explain why we measured the insertion loss with the GRIN-MFA to be slightly smaller (0.15 dB) than for TEC-MFA (0.21 dB).

It is worth mentioning that a low-level of cross-coupling into $LP_{11}$ mode (e.g., -35 dB in our experiment) is more critical than coupling into other HOMs due to the relatively low $LP_{11}$ mode attenuation. The relatively high level of cross-talk into the $LP_{02}$ mode is then less critical for most applications due to the very high attenuation of the $LP_{02}$ mode in typical NANFs. Apart from the $LP_{11}$ mode, all HOMs suffer attenuation similar to or higher than $LP_{02}$ mode.

We conclude that the predominant loss mechanism of our interconnection is through coupling into the $LP_{02}$ mode. We expect this could be minimized by designing the GRIN fiber (to have a refractive index profile that slightly deviates from parabolic) or by optimizing the fiber (refractive index profile) used in the TEC process. As far as reduction of the $LP_{11}$ mode coupling concerns, this would require more symmetric structure of the fabricated NANF. Since better symmetry will also bring lower attenuation[2], $LP_{11}$ mode coupling will be further reduced for lower-attenuation NANFs that have been already reported recently[2].

### Permanent interconnection

Based on the results shown in Fig. 5 we have proceeded to creating a permanent interconnection using a technique described in detail in[9]. We used a slightly modified setup from Fig. 4, where we added fiber-array holders (Thorlabs HFA001) onto the 5-axis stages.

The GRIN MFA, as discussed above, is glued in a fiber array and then polished to the desired length and AR coated. NANF fiber array, however, is prepared slightly differently, because the end-face of the NANF cannot be polished, as debris would get into the holes. This modified procedure has three steps. Firstly, after striping the protective coating from the small portion of NANF, we cleaved it, and inserted it into an empty pre-polished fiber array. Then, the NANF cleaved end-face was aligned with the pre-polished fiber-array end-face, so that both NANF and fiber-array end at the same point. Finally, we applied a

UV-curable glue to the back-side of the NANF fiber array to secure NANF inside it.

Afterwards, we put both fiber arrays (with GRIN MFA and NANF) into the fiber-array holders, which we fixed on our 5D stages (Thorlabs NanoMax MAX313D/M with pitch and yaw tilt platform APY002/M), enabling precise alignment in the same way that was used previously for characterization. After aligning the two fiber arrays, we applied a viscous UV-curable glue in between the two fiber arrays (ensuring the glue does not creep into the NANF microstructure) and cured the glue to form a permanent interconnection. During the curing process, we continuously monitored IL of the interconnection and observed an IL degradation of 0.01 dB, which is within our measurement accuracy. Thus, we conclude that the gluing did not degrade the interconnection performance.

It is worth mentioning that although we made the interconnections manually (as a proof of concept), the entire process can be in principle fully automated, as it is for conventional gluing-based fiber array assembly in the photonic industry.

## Conclusion

We have demonstrated record low-loss interconnect between NANF and SMF with insertion loss of only 0.15 dB. This is 0.07 dB above the theoretically-expected minimum loss due to the mode shape and symmetry mismatch between the NANF mode and an ideal Gaussian mode. The interconnect was based on a modified fiber-array technology, which is industry-proven, used, e.g., in telecom when attaching SMFs to high-port-number planar lightwave splitters (e.g., 1x64). As gluing is a cold process (no fusion splicing involved), it allows for deposition of optical coatings in between NANF and the SMF-GRIN mode field adapter. Anti-reflective coatings strongly-reduce the SMF-NANF 3.5% back-reflection due to the hollow core (air) to glass core interface. We experimentally demonstrated better than -40 dB back-reflection over 60 nm bandwidth while reducing the interconnection insertion loss by 0.15 dB (corresponding to the theoretically-expected reduction by 3.5%).

We used two approaches for adaptation of the mode field size between the SMF and NANF. The first mode field adapter used a short segment of telecom-standard (OM2) graded-index multimode fiber. The interconnection insertion loss was 0.15 dB, where we showed that a length variation as large as 15 µm (such accuracy can be straightforwardly achieved with a modified standard fiber cleaver) does not degrade the excellent interconnection insertion loss performance.

The second mode field adaptation approach used a thermally-expanded core of SMF. TECs are available commercially at low cost and can be manufactured with advanced commercially-available fusion splicers. We achieved NANF-SMF interconnection loss of 0.21 dB with TEC mode field adapters.

We studied the unwanted coupling into higher-order modes of NANF. We measured HOMs using a simple method based on an analysis of optical spectra. For the lowest-attenuation HOM ($LP_{11}$, about 35 dB/km in our NANF), we found unwanted coupling below -35 dB being most likely limited by the slight asymmetry of the fabricated NANF (rather than alignment or NANF end-face cleaving imperfection). The second most prominent HOM into which a small portion of light was coupled is the $LP_{02}$ mode (attenuation of 2100 dB/km in our NANF). Coupling into this mode, which has the same symmetry as the $LP_{01}$ mode, is mainly due to the mismatch of the shape of the mode field adapter output and the NANF $LP_{01}$ fundamental mode profile. We show that GRIN-based mode field adapter produces slightly smaller coupling into the $LP_{02}$ mode (-21.3 dB) than the TEC mode field adapter (-20.1 dB), suggesting the first one has a mode field shape better adapted to the $LP_{01}$ mode than the latter. This agrees with our insertion loss measurements, which show slightly worse result for TEC mode field adapters (0.21 dB versus 0.15 dB).

We then show that permanent glued interconnection of NANF with a GRIN-based mode field adapter brings negligible (0.01 dB in our measurement, which is at our resolution limit) degradation to the final interconnection.

This work represents a new benchmark in hollow core fiber interconnection, showing simultaneously low loss, low coupling into higher-order modes, and low level of back-reflection. It also outlines further necessary steps to improve this even further (e.g., by improving the symmetry of the hollow core fiber or engineering the mode field profile generated by mode field adapters to better match the shape of the hollow core fiber fundamental mode).

## References


1. Bradley, T. D. *et al.* Record Low-Loss 1.3dB/km Data Transmitting Antiresonant Hollow Core Fibre. In *44th European Conference on Optical Communication (ECOC 2018)*, 1–3, DOI: 10.1109/ECOC.2018.8535324 (2018).
2. Jasion, G. T. *et al.* Hollow Core NANF with 0.28 dB/km Attenuation in the C and L Bands. In *Optical Fiber Communication Conference Postdeadline Papers 2020*, Th4B.4, DOI: 10.1364/OFC.2020.Th4B.4 (Optical Society of America, 2020).
3. Bradley, T. *et al.* Antiresonant Hollow Core Fibre with 0.65 dB/km Attenuation across the C and L Telecommunication bands. In *45th European Conference on Optical Communication (ECOC 2019)* (2019).
4. Kuschnerov, M. *et al.* Transmission of commercial low latency interfaces over hollow-core fiber. *J. Light. Technol.* **34**, 314–320, DOI: 10.1109/JLT.2015.2469144 (2016).

5. Mutugala, U. *et al.* Hollow-core fibres for temperature-insensitive fibre optics and its demonstration in an optoelectronic oscillator. *Sci. Reports* **8**, DOI: 10.1038/s41598-018-36064-1 (2018).
6. Roberts, P. *et al.* Achieving low loss and low nonlinearity in hollow core photonic crystal fibers. In *Lasers and Electro-Optics*, 1240–1242 Vol. 2 (2005).
7. Liu, Z. *et al.* Nonlinearity-free coherent transmission in hollow-core antiresonant fiber. *J. Light. Technol.* **37**, 909–916, DOI: 10.1109/JLT.2018.2883541 (2019).
8. Shephard, J. *et al.* Improved hollow-core photonic crystal fiber design for delivery of nanosecond pulses in laser micromachining applications. *Appl. Opt.* **44**, 4582–4588, DOI: 10.1364/AO.44.004582 (2005).
9. Komanec, M. *et al.* Low-loss and low-back-reflection hollow-core to standard fiber interconnection. *IEEE Photonics Technol. Lett.* **31**, 723–726, DOI: 10.1109/LPT.2019.2902635 (2019).
10. Xiao, G., Zhang, Z. & Grover, C. Adhesives in the packaging of planar lightwave circuits. *Int. J. Adhesion Adhesives* **24**, DOI: 10.1016/j.ijadhadh.2003.11.003 (2004).
11. Suslov, D. *et al.* Highly-efficient and low return-loss coupling of standard and antiresonant hollow-core fibers. In *Frontiers in Optics + Laser Science APS/DLS*, FW5B.2, DOI: 10.1364/FIO.2019.FW5B.2 (Optical Society of America, 2019).
12. Jung, Y. *et al.* Compact micro-optic based components for hollow core fibers. *Opt. Express* **28**, 1518–1525, DOI: 10.1364/OE.28.001518 (2020).
13. Choi, H. *et al.* Miniature fiber-optic high temperature sensor based on a hybrid structured Fabry-Perot interferometer. *Opt. Lett.* **33**, 2455–2457, DOI: 10.1364/OL.33.002455 (2008).
14. Xin, M. *et al.* Attosecond precision multi-kilometer laser-microwave network. *Light. Sci. Appl.* **6**, DOI: 10.1038/lsa.2016.187 (2017).
15. Lisdat, C. *et al.* A clock network for geodesy and fundamental science. *Nat. Commun.* **7**, DOI: 10.1038/ncomms12443 (2016).
16. Sakr, H. *et al.* Ultrawide bandwidth hollow core fiber for interband short reach data transmission. In *2019 Optical Fiber Communications Conference and Exhibition (OFC)*, 1–3 (2019).
17. Nespola, A. *et al.* Record PM-16QAM and PM-QPSK transmission distance (125 and 340 km) over hollow-core-fiber. In *45th European Conference on Optical Communication (ECOC 2019)*, 285 (4 pp.)–285 (4 pp.), DOI: 10.1049/cp.2019.1019 (2019).
18. Fokoua, E. N. *et al.* Accurate modelling of fabricated hollow-core photonic bandgap fibers. *Opt. Express* **23**, 23117–23132, DOI: 10.1364/OE.23.023117 (2015).
19. Gray, D. R. *et al.* Complementary analysis of modal content and properties in a 19-cell hollow core photonic band gap fiber using time-of-flight and $S^2$ techniques. In *2012 38th European Conference and Exhibition on Optical Communications*, 1–4 (2012).
20. Chang, M. P. & Buscher, D. F. Cleaving optical fibre lengths to high relative accuracy. *Opt. Commun.* **157**, 282 – 290, DOI: https://doi.org/10.1016/S0030-4018(98)00440-4 (1998).


## 1 Acknowledgment


This work was supported by EPSRC project "Airguide Photonics", under grant EP/P030181/1 and the Czech Technical University in Prague project through SGS20/166/OHK3/3T/13. F. Poletti gratefully acknowledges EU ERC (grant 682724); R. Slavík and E. Numkam Fokoua were supported by RAEng Fellowships.
The data in this paper is accessible through the University of Southampton research repository (DOI: 10.5258/SOTON/D1774).


## 2 Author contributions

D.S. and R.S. wrote the manuscript and prepared figures with input from M.K. and S.Z.. D.S. and D.D. carried out the experiments. M.K., A.Z. and E.R.N.F. conducted the simulations and calculations. T.D.B., F.P. and D.J.R. designed and manufactured the fiber. The manuscript results were discussed by all authors and all authors provided comments on the draft of the manuscript.

## 3 Competing interests

Authors declare no competing interests.

## 4.4 Long-length and thermally stable high-finesse Fabry-Perot interferometers made of hollow-core optical fiber

Reference paper:

M. Ding, M. Komanec, D. Suslov, D. Dousek, S. Zvánovec, E.R. Numkam Fokoua, T. Bradley, F. Poletti, D.J. Richardson, R. Slavík, "Long-Length and Thermally Stable High-Finesse Fabry-Perot Interferometers Made of Hollow Core Optical Fibe" *IEEE/OSA Journal of Lightwave Technology*, 2020, 38(8), 2423-2427. ISSN 0733-8724.

Relevance to the thesis:

The rapid development of low-loss HCFs has enabled their use in cutting-edge applications such as Fabry-Perot interferometry (FPI). The use of HCF is highly advantageous thanks to the significantly lower thermal drift of the frequency compared to the SMF (110 MHz/°C in NANF vs 1.6 GHz/°C in SMF). The FPI in this paper was constructed using a slight modification of our coupling method where, instead of ARC on MFA, we deposited a highly reflective coating (over 98%) which forms the two mirrors of the cavity. Two interconnected samples were prepared using 5- and 23- m-long NANF with resulting finesse of 154 and 130 and with transmission peaks of 47 kHz and 50 kHz, respectively.

# Long-Length and Thermally Stable High-Finesse Fabry-Perot Interferometers Made of Hollow Core Optical Fiber

Meng Ding, Matěj Komanec, Dmytro Suslov, Daniel Dousek, Stanislav Zvánovec, Eric R. Numkam Fokoua, Thomas D. Bradley, Francesco Poletti, David J. Richardson, *Fellow, IEEE*, and Radan Slavík, *Senior Member, IEEE*

***Abstract*—We made and characterized two Fabry-Perot interferometer samples made of the latest-generation hollow core fiber with sub-1-dB/km loss. Thanks to this low transmission loss, we achieved a finesse of over 140 and 120, for interferometer lengths of 5 and 23 m, respectively. This resulted in transmission peaks as narrow as 47 kHz. Our all-fiber Fabry-Perot interferometers have standard single-mode fiber pigtails (for easy integration in conventional fiber optic systems) and employ fiber mode field adapters to enable low-loss coupling between the pigtails and the low-loss hollow core fiber. The high-reflectivity mirrors (>98%) were deposited directly on the fiber mode field adapters, which were glued to the hollow core fiber, resulting in permanently-aligned Fabry-Perot interferometers. We also measured how the position of the transmission peaks change with temperature (an important performance metrics for most applications, e.g., when used as a narrow-band band-pass filter) and found that it changed 14.5 times less in our Fabry-Perot interferometer relative to a similar device made of standard single mode fiber.**

***Index Terms*—Fabry-Perot, optical fiber applications, optical fiber devices.**

## I. Introduction

FABRY-PEROT interferometers (FPs) have many unique properties including high wavelength selectivity, high extinction ratios, the capability to enhance light intensity, etc. Their applications include, amongst others: lasers [1]–[3], metrology [4], [5] and sensing [6]–[8]. The full width at half maximum, FWHM of the transmission peaks is the key parameter of a FP, as a narrower peak provide better capability to discriminate frequency [6], of relevance, e.g., in reference cavities [2] or a ultra-high resolution sensors [5]. Another important parameter is the free spectral range (FSR), which is the spacing between neighboring transmission peaks and which is inversely proportional to the FPs optical length $nL$, where $n$ is the refractive index and $L$ is the length. The finesse ($F$) is then defined as the ratio FSR/FWHM. A small FWHM can be achieved with a high finesse or small FSR (or both). In free-space FPs (made, e.g., by drilling a hole in a low-expansion glass rod and then attaching high reflectivity mirrors at both ends [4]), $L$ is usually limited by practical constraints to less than 50 cm, limiting the achievable FSR. Thus, if a small FWHM is desired, ultra-high finesse (sometimes $>10^5$) is needed, making such FPs highly sensitive to alignment. Thus, an alternative implementation using single-mode fiber FPs (SMF-FPs) has been widely investigated. SMF-FPs can have long lengths (e.g., 100's of meters) and can be very compact and lightweight. Although the finesse of SMF-FPs [7], [8] does not reach that achievable in free-space FPs (due to the fiber transmission loss), their small FSR enables narrow transmission peaks similar to those of short, high-finesse free-space FPs. Unfortunately, SMF-FPs have several drawbacks that make free-space FPs the preferred approach for many applications, despite free-space FPs larger size and the alignment challenges. The two primary drawbacks are the large sensitivity to temperature variations [8] and unwanted nonlinear effects like stimulated Brillion scattering (SBS) [9], especially in high-finesse FPs where the intra-cavity power is strongly enhanced by the resonant effect. Both of these parasitic effects are mainly due to the interaction of light with the silica glass material in SMFs. For example, the thermal sensitivity of the FSR (determined by the temperature dependence of the optical length $nL$ of the SMF) is dominated (95%) by thermally-induced changes in the $n$ of silica glass (thermo-optic effect) with the thermally-induced fiber length (thermal expansion effect) change providing the other 5% [10].

Hollow core fibers (HCFs) in which the glass-light interaction is very weak should address shortcomings discussed above. Firstly, the thermo-optic effect is practically eliminated, making HCF 20 times less thermally sensitive than SMF of equal $L$ [10]. When considering equal optical length $nL$, this advantage

Manuscript received December 13, 2019; revised February 8, 2020; accepted February 9, 2020. Date of publication February 12, 2020; date of current version April 15, 2020. This work was supported in part by the EPSRC project "Airguide Photonics", under Grant EP/P030181/1 and in part by the Czech Technical University in Prague under Grant SGS SGS17/182/OHK3/3T/13. The work of Meng Ding was supported by CSC scholarship. The work of Francesco Poletti was supported by EU ERC under Grant 682724. The work of Radan Slavík was supported by RAEng Fellowship. *(Corresponding author: Meng Ding.)*

Meng Ding, Eric R. Numkam Fokoua, Thomas D. Bradley, Francesco Poletti, David J. Richardson, and Radan Slavík are with the Optoelectronic Research Centre, University of Southampton, SO17 1BJ Southampton, U.K. (e-mail: m.ding@soton.ac.uk; eric.numkam-fokoua@soton.ac.uk; t.bradley@soton.ac.uk; frap@orc.soton.ac.uk; djr@orc.soton.ac.uk; r.slavik@soton.ac.uk).

Matěj Komanec, Dmytro Suslov, Daniel Dousek, and Stanislav Zvánovec are with the Faculty of Electrical Engineering, Czech Technical University in Prague, 16627 Prague, Czech Republic (e-mail: komanmat@fel.cvut.cz; suslodmy@fel.cvut.cz; dousedan@fel.cvut.cz; xzvanove@fel.cvut.cz).

Color versions of one or more of the figures in this article are available online at https://ieeexplore.ieee.org.

Digital Object Identifier 10.1109/JLT.2020.2973576

0733-8724 © 2020 IEEE. Personal use is permitted, but republication/redistribution requires IEEE permission.
See https://www.ieee.org/publications/rights/index.html for more information.



Authorized licensed use limited to: UNIVERSITY OF SOUTHAMPTON. Downloaded on April 08,2020 at 08:59:58 UTC from IEEE Xplore. Restrictions apply.

is reduced (as $n\sim1$ in HCF compared to $n\sim1.45$ in SMF) to about 14 times [11], [12]. Nonlinearities are also substantially weaker in HCF as compared to SMF, enabling several orders of magnitude higher powers to be launched into HCF-FPs as compared to SMF-FPs [1].

Several recent works have reported high-finesse HCF-FPs. The cavity mirrors were formed using photonic crystal slabs [13] or high-reflectivity dielectric coatings [14]. However, all these reports dealt with cm-long fiber lengths limiting their use for applications requiring narrow FWHM transmission peaks. Generally, they used 7-cell photonic bandgap HCF designs, which offer good coupling into SMF, but whose high loss (>10 dB/km [15]) does not allow the construction of high-finesse long-length HCF-FPs (e.g., for 20-m long FP made with 10-dB/km fiber, the fiber-loss-limited maximum achievable finesse is 68). Furthermore, the reported HCF-FPs were not designed for long-term operation since their ends were not sealed, enabling air-born pollution like water vapor and dust to enter the hollow core, possibly causing long-term HCF-FP performance degradation.

Concerning ongoing efforts to reduce HCF loss, antiresonant type HCFs have recently witnessed tremendous progress [16]–[18]. The most recent results obtained with the Nested Antiresonant Node-less Fiber (NANF) geometry have broken the 1-dB/km barrier (0.65 dB/km across a bandwidth of 120 nm [18]). This has opened up a host of new application opportunities, including the possibility of making long length high-finesse HCF-FPs.

In this paper, we demonstrate and characterize two HCF-FPs with lengths of 5 and 23 m, with finesse > 120 over a wavelength range from 1530–1565 nm, made using NANF with sub-1 dB/km loss and pigtailed with SMF. These HCF-FPs are two orders of magnitude longer than previously-demonstrated. We compare their thermal stability with that of an SMF-FP, demonstrating more than an order of magnitude better performance. Besides improving the stability of fiber-based FPs, this also represents the first demonstration of such low thermal sensitivity in antiresonant HCFs; to date this has only been previously demonstrated for photonic bandgap type HCFs.

## II. Fabrication of HCF-FPs

The schematic of the pigtailed HCF-FP is shown in Fig. 1. The HCF used is a NANF similar to the one reported in [18] with a loss of 0.9 dB/km, operating in the 1550-nm wavelength region. The HCF-FP is pigtailed with SMF. Because of the mode mismatch between the fundamental mode of the HCF used (21 µm) and standard SMF (10 µm), a suitable piece of GRIN fiber was inserted in between the two to enable mode field adaptation [19]. The GRIN fiber was first fusion spliced to the SMF. Before connecting it to the HCF, a FP mirror was deposited on its end-face. We used a 13-layer Ta2O5/SiO2 dielectric coating-based mirror with a reflectivity of >98% (from 1500–1570 nm). We did not use fusion splicing to interconnect the mirrors to the HCF, as this would destroy the mirror and could cause deformation of the HCF microstructure. We also did not use mechanical splice as shown in [14], since this approach does not allow for active alignment of the angle between the NANF and the mirror, imposing inherent limitation to reproducibility as well as the maximum achievable finesse. Instead, we used a modified fiber-array technique (used industrially for fiber pigtailing of planar lightwave circuits, PLCs) which we have refined for low-loss interconnection (<0.3 dB/interconnection) between HCFs and SMF [19]. Here, the SMF spliced to the GRIN is first glued into a V-groove array, polished to the desired GRIN fiber length, and afterwards, a coating is deposited on the end facet (the mirror in the work presented here). Then the carefully cleaved NANF is inserted into another fiber array V-groove and glued in to that. The two fiber arrays are actively aligned (in x, y, z, pitch, and yaw) before gluing the fiber arrays together (to obtain a permanent and sealed interconnection, which does not allow any air-born pollutants to enter the hollow core cavity, and thus ensures no degradation in the long-term performance). A Photograph of a typical glued interconnection is shown in Fig. 1b.

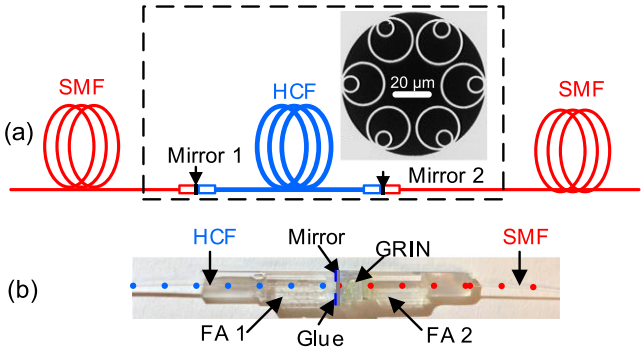


Fig. 1. (a) Configuration of the pigtailed HCF-FP with a cross-sectional scanning electron microscope (SEM) image of the HCF used. (b) Photograph of the fully assembled SMF-GRIN-Mirror-HCF interconnection. FA: fiber array, GRIN: Graded-index fiber based mode field adapter.

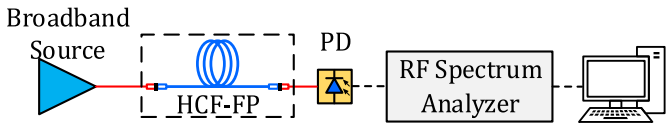


Fig. 2. Set-up for characterization of FPs in the radio-frequency (RF) domain. The broadband source is formed by two cascaded Erbium-doped fiber amplifiers (EDFAs) with a tunable bandpass filter inserted in between them. PD: photodetector.

Since we target long length high-finesse FPs which have very narrow transmission peaks, optical scanning method used, e.g., in [13] is not ideal for active cavity alignment prior to gluing. This is because too many parameters are changing during the alignment (FP peaks spectral position, insertion loss, polarization, etc.), making alignment tedious and slowly converging. We found that in practice, the following two methods (for coarse and fine alignments) allowed us to align the HCF-FP cavity relatively quickly. For the coarse alignment, we optimized transmitted optical power of the HCF-FP using a 10-nm wide broadband incoherent light source and a photodetector. Once maximum power has been reached, we analyzed the photodetected signal with a radio-frequency (RF) spectrum analyzer observing RF beats (discussed in detail later) [20], Fig. 2. In the



Authorized licensed use limited to: UNIVERSITY OF SOUTHAMPTON. Downloaded on April 08,2020 at 08:59:58 UTC from IEEE Xplore. Restrictions apply.

coarse method, the transmitted power is insensitive to HCF-FP peaks spectral position and polarization state inside the FP. By maximizing the transmitted power, coupling loss between the HCF and the mirrors (i.e., how much light at the HCF output is coupled back into it) is minimized, which in practice allows for almost-optimum HCF-FP cavity alignment. The RF beat analysis technique allowed us to measure FP finesse directly (as we show below) enabling us to fine tune the FP. The signal shown on the RF spectrum analyzer is proportional to the convolution of the FP's optical coefficient with its conjugate:

$$P(f) \propto \frac{1}{1+\left(\frac{2F_e}{\pi}\right)^2 \sin^2\left(\frac{\pi f}{FSR}\right)}. \quad (1)$$

Here, $f$ is the signal frequency shown on the RF spectrum analyzer and $F_e$ is:

$$F_e = \frac{\pi R}{1-R^2} \approx \frac{\pi\sqrt{R}}{2(1-R)} = \frac{F}{2}. \quad (2)$$

where $R = \sqrt{R_1}\sqrt{R_2}\alpha$ is the effective reflectivity of the interferometer with $R_{1,\,2}$ being the reflectivities of the mirrors, and $\alpha$ the single-trip loss including the coupling loss between the HCF and the mirrors (i.e., how much light at the HCF output is coupled back into it) and fiber transmission loss. Although Eq. (1) is identical in form to the expression for the FP's optical transmission transfer function [13] it is not the same since $F_e$ is different to the finesse $F$. For a high-finesse FP in which $R\sim1$, we have derived that $F \sim 2F_e$ based on the first order Taylor series approximation. Thus, the FP's RF spectrum has twice as large peaks compared to the optical spectrum. In our experiment, data from the RF spectrum analyzer were acquired with a computer, where they were fitted with Eq. (1) in LABVIEW, enabling the FSR and finesse to be output in real-time, allowing for active FP alignment.

We made two HCF-FP samples using 5 and 23 m long HCFs. When aligned (prior to gluing), their Finesses were 195 and 160, respectively. After gluing using a UV-curable glue, we witnessed a slight finesse reduction to 153 and 133, respectively. Although we believe this may be improved by further refining the gluing process, the high-finesse (>120) FPs obtained are robust and have not degraded with time (we have not seen any degradation in four months since gluing them).

The 23-m HCF-FP had a smaller finesse both before and after the gluing as compared to the 5-m device. By considering the HCF loss of 0.9 dB/km and mirror reflectivity of 98.6%, analysis using Eqs. (1, 2) suggests that it is due to the HCF's transmission loss.

## III. Characterization

Following the fabrication, we characterized the FPs using two techniques - besides the convenient, fast, and high-dynamic range RF technique we have described; we also measured it directly in the optical domain. We measured all of the important parameters (insertion loss, birefringence, and dependence on the wavelength). Finally, we measured the FPs' thermal sensitivity.

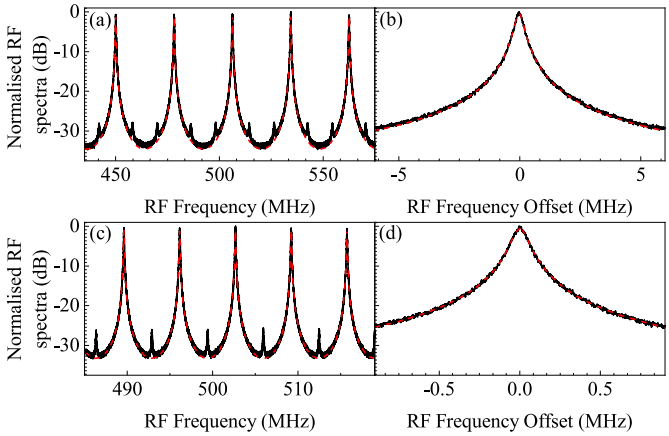


Fig. 3. Measured results for 5 m-HCF-FP (a, b) and 23 m HCF-FP (c, d). Normalized RF power spectra around 500 mHz (a,c) and their details around one peak (b, d). Solid black: measured, red dashed: fitted with Eq. (1).

### A. Characterization in the RF Domain

The FP's transmission spectra including information about FSR and finesse were measured in RF domain using the method described previously. Normalized RF power spectra showing 5 peaks around 500 MHz and normalized RF power spectra showing one peak with fitted curves for the fabricated HCF-FPs are shown in Fig. 3. The broadband source used for this measurement had a 1 nm optical bandwidth (this narrow bandwidth allowed us to perform spectrally-dependent characterization shown later) with a central wavelength of 1550 nm (given by the optical bandpass filter used in the source set-up, Fig. 2). The small spikes at bottom of the RF power spectra are artefacts originating from noise in the EDFA electronics. We saw them in all our experiments. When fitting the experimental data with Eq. (1), we used only data above −10 dB to avoid any contribution from the measurement noise. Despite this, we achieved a very good fit across the entire fitting range. The FSR and $F$ were 28.1 MHz and 153 for the 5 m HCF-FP and 6.5 MHz and 133 for the 23 m HCF-FP.

Subsequently, we measured the RF spectrum of the HCF-FPs over the entire C band (by tuning the wavelength of the 1-nm bandwidth tunable bandpass filter, Fig. 2). The results of both FPs are displayed in Fig. 4(a) (finesse) and Fig. 4(b) (FSR). The finesse values range from 140 to 160 for the 5-m HCF-FP and from 120 to 138 for the 23-m HCF-FP. Considering this measurement data and their variation across the C-band, the effective reflectivity (reflectivity that includes the coupling loss of light from the HCF to the mirror and back and HCF transmission loss) was calculated to be between 97.8% and 98.1% (5-m HCF-FP) and 97.4% to 97.75% (23 m HCF-FP). The FSRs, Fig. 4(b) slightly decrease with wavelength (by 150 Hz for 5-m HCF-FP and 600 Hz for 23-m HCF-FP over the entire C-band). This is due to the HCF chromatic dispersion, which we confirmed by fitting the data in Fig. 4(b) and calculating HCF chromatic dispersion from them, obtaining value of 2 ps/nm/km. This is consistent with value expected for our NANF-type HCF [18]. It is worth mentioning that this value of chromatic dispersion is 8



Authorized licensed use limited to: UNIVERSITY OF SOUTHAMPTON. Downloaded on April 08,2020 at 08:59:58 UTC from IEEE Xplore. Restrictions apply.

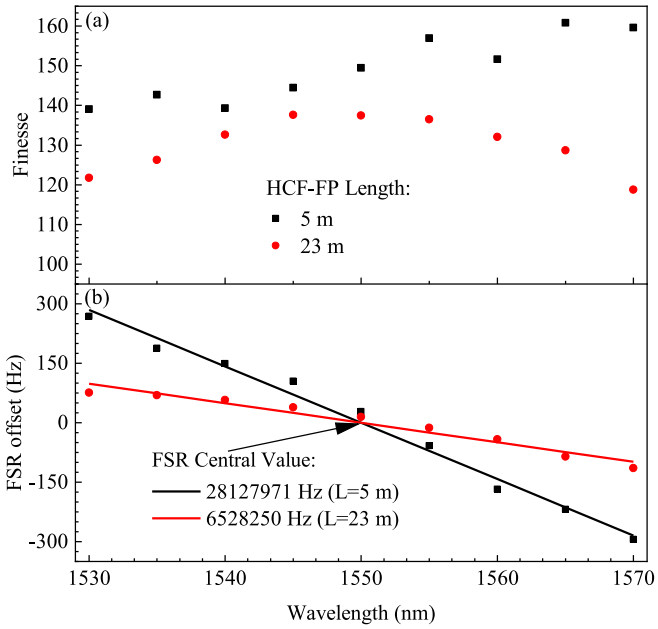


Fig. 4. (a) Finesse and (b) FSR offset of the two HCF-FP samples measured with the RF method every 5 nm across the C band.

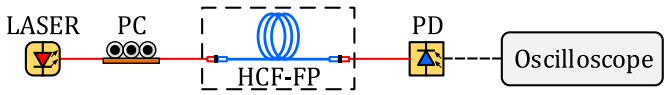


Fig. 5. Set-up to characterize the HCF-FPs in the optical domain. PC: polarization controller; PD: photodetector.

times lower than SMF and thus our HCF-FP is expected to have 8 times smaller variation of its FSR as compared to SMF-FP.

### B. Characterization in the Optical Domain

Further FP parameters such as insertion loss (FP transmission loss at resonance) and polarization dependence are less straightforward to measure using the RF analysis technique. Thus, we implemented a characterization technique operating directly in the optical domain, Fig. 5.

We scanned the input light frequency of a narrow-linewidth (<10 kHz) fiber laser (NP Photonics, 1556 nm) by applying a sawtooth waveform on its RF port. The output was photodetected and visualized on an oscilloscope. The laser RF port response was calibrated to obtain the spectral characteristics of the FP transfer.

Due to the birefringence of the HCF (caused by the fabricated HCF inner structure not being perfectly symmetric and by HCF bending/coiling [21]), transmission peaks occur at two different positions within one FSR period when varying the polarization state of the launched light (via a polarization controller, Fig. 5). It is worth mentioning that this phenomenon is also observed with SMF-FPs [22] in which a very small residual fiber birefringence causes this splitting. The transmitted spectra for the two polarization eigenstates of two HCF-FPs are displayed in Fig. 6. The polarization peak spectral splitting was 15.1 and 2.42 MHz for the 5 and 23 m HCF-FPs, respectively. If the two peaks for the

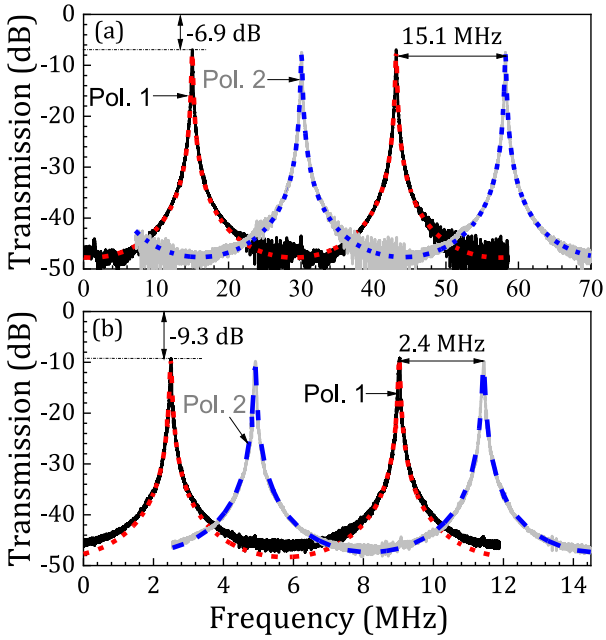


Fig. 6. Measured optical transmission spectra along the two principal axes of birefringence (Pol. 1, black and Pol. 2, grey solid) of (a) 5 m and (b) 23 m HCF-FPs. The insertion loss and polarization-induced spectral splitting are also shown. The red and blue dashed lines are data fitted by the transmission function of FP.

5 m HCF-FP were within the same FP resonance order (which we have not confirmed yet), HCF phase birefringence would have been $8 \times 10^{-8}$ with corresponding beat length of 20 m.

We measured the FP's insertion loss to be 6.9 dB for the 5 m HCF-FP, Fig. 6, with the fitted finesse of 166 and 154 for the two polarization eigenstates, respectively. For the 23 m HCF-FP, the FP insertion loss was 9.3 dB and the fitted finesse was 139 and 130 (corresponding to 3-dB transmission peak width of 47 and 50 kHz), respectively. The obtained finesses are consistent with the RF method. Based on our theoretical analysis using Eqs. (1, 2), the FP insertion loss is mainly caused by the mirror loss (∼0.5% for the mirrors used). Replacing the current mirrors with improved mirrors with a loss of 0.1% would reduce the FPs insertion loss by ∼3 dB. Furthermore, by improving the gluing technique (i.e., no degradation of finesse during the gluing process), we could further improve the FP insertion loss by ∼2 dB for the two HCF-FPs.

### C. Characterization of the Thermal Response

Thermal response here refers to how the transmission peaks frequency shifts with temperature. We characterized the thermal response of our 5 m HCF-FP using the set-up shown in Fig. 7. For comparison purposes we placed the 5 m HCF-FP together with a 3.6 m SMF-FP (which has the same optical length $nL$ as the 5 m HCF-FP) into the same thermal chamber. The light source (NP Photonics used earlier, but here operated at fixed wavelength) was split and launched simultaneously into both FPs. PCs were used at both interferometer inputs to align the input polarization to one of the two FPs' eigenstates. The output power of both FPs was monitored using two photodiodes.



Authorized licensed use limited to: UNIVERSITY OF SOUTHAMPTON. Downloaded on April 08,2020 at 08:59:58 UTC from IEEE Xplore. Restrictions apply.

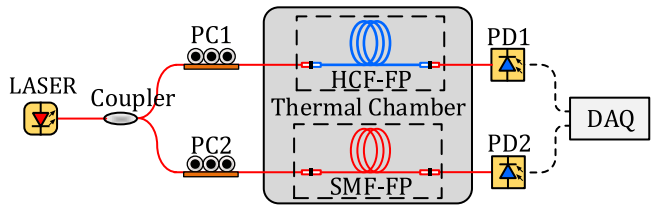


Fig. 7. Set-up for the thermal response measurement. DAQ: Data Acquisition System.

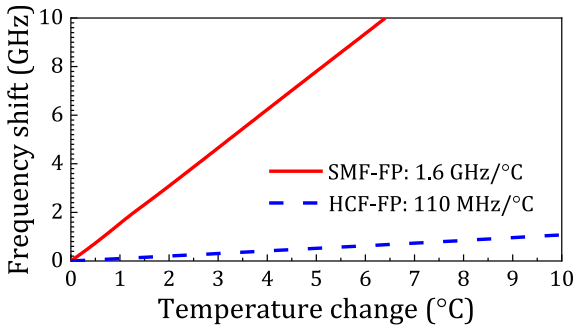


Fig. 8. Frequency shift of a selected transmission peak in the HCF-FP and a SMF-FP (of equivalent optical length) as the temperature is increased.

From the results shown in Fig. 8 we see that the transmission peak of the HCF-FP moved at a rate of 110 MHz/°C while in the SMF-FP it moved by 1.6 GHz/°C. Thus, the temperature sensitivity of HCF-FP is 14.5 times lower than that of SMF-FP, which matches well with the theoretical prediction. This is also the first demonstration of such a low sensitivity using an antiresonant HCF.

## IV. Conclusion

In conclusion, we fabricated 5-m and 23-m long HCF-FPs. Our fully assembled permanent-connection based FPs have finesse >120 over the entire C band, which represents the first demonstration of long length (>1 m) HCF-FPs with such a high finesse. This was enabled by the combination of the latest-generation of low-loss (sub-1dB/km) HCFs and the recently developed technique for permanent, low loss, fusion-splice-less sealed HCF interconnection with standard optical fibers. We achieved a FP transmission peak width as narrow as 47 kHz (with an equivalent time delay of 3.2 km). This is only a factor of three wider than for state-of-the-art bulk FP cavities that are typically 10 cm long and have a finesse in excess of $10^5$. We also showed HCF-FPs to have 14.5 times lower thermal sensitivity than SMF-FPs, which is due to the HCF's low thermal phase sensitivity. Our work represents the first demonstration of this property for antiresonant type HCF. The performance we demonstrate here, together with the expected high nonlinear threshold [9], will be of interest in many applications in which SMF-FPs cannot be used and free-space FPs are impractical.

## Acknowledgment

The data in this paper is accessible through the University of Southampton research repository (DOI: 10.5258/SOTON/D1233).

## References

[1] A. V. V. Nampoothiri *et al.*, "Hollow-core optical fiber gas lasers (HOFGLAS): A review [Invited]," *Opt. Mater. Express*, vol. 2, no. 7, pp. 948–961, 2012.
[2] A. V. V. Nampoothiri, B. Debord, M. Alharbi, F. Gérôme, F. Benabid, and W. Rudolph, "CW hollow-core optically pumped $I_2$ fiber gas laser," *Opt. Lett.*, vol. 40, no. 4, pp. 605–608, Feb. 2015.
[3] M. Xu, F. Yu, M. R. Hassan, and J. C. Knight, "Continuous-wave mid-infrared gas fiber lasers," *IEEE J. Sel. Top. Quantum Electron.*, vol. 24, no. 3, May-Jun. 2018, Art no. 0902308.
[4] S. Häfner *et al.*, "$8 \times 10^{-17}$ fractional laser frequency instability with a long room-temperature cavity," *Opt. Lett.*, vol. 40, no. 9, pp. 2112–2115, May 2015.
[5] T. Kessler *et al.*, "A sub-40-mHz-linewidth laser based on a silicon single-crystal optical cavity," *Nat. Photon.*, vol. 6, no. 10, pp. 687–692, Oct. 2012.
[6] G. Gagliardi, M. Salza, S. Avino, P. Ferraro, and P. De Natale, "Probing the ultimate limit of fiber-optic strain sensing," *Science.*, vol. 330, no. 6007, pp. 1081–1084, Nov. 2010.
[7] J. Chen, Q. Liu, X. Fan, and Z. He, "Ultrahigh resolution optical fiber strain sensor using dual pound–drever–hall feedback loops," *Opt. Lett.*, vol. 41, no. 5, pp. 1066–1069, 2016.
[8] N. M. R. Hoque and L. Duan, "Ultrahigh-resolution fiber-optic sensing using a high-finesse, meter-long fiber fabry-perot resonator," Aug. 2019, *arXiv:1908.08595*.
[9] M. B. Gray, J. H. Chow, K. McKenzie, and D. E. McClelland, "Using a passive fiber ring cavity to generate shot-noise-limited laser light for low-power quantum optics applications," *IEEE Photon. Technol. Lett.*, vol. 19, no. 14, pp. 1063–1065, Jul. 2007.
[10] R. Slavík *et al.*, "Ultralow thermal sensitivity of phase and propagation delay in hollow core optical fibers," *Sci. Rep.*, vol. 5, no. 1, Dec. 2015, Art. no. 15447.
[11] M. Tateda, S. Tanaka, and Y. Sugawara, "Thermal characteristics of phase shift in jacketed optical fibers," *Appl. Opt.*, vol. 19, no. 5, pp. 770–773, 1980.
[12] S. Meiselman and G. A. Cranch, "Optical phase response to temperature in a hollow-core photonic crystal fiber," *Opt. Express*, vol. 25, no. 22, pp. 27581–27594, Oct. 2017.
[13] J. Flannery, R. Al Maruf, T. Yoon, and M. Bajcsy, "Fabry-pérot cavity formed with dielectric metasurfaces in a hollow-core fiber," *ACS Photon.*, vol. 5, no. 2, pp. 337–341, Feb. 2018.
[14] Y. Tan *et al.*, "Hollow-core fiber-based high finesse resonating cavity for high sensitivity gas detection," *J. Light. Technol.*, vol. 35, no. 14, pp. 2887–2893, 2017.
[15] R. Amezcua-Correa, F. Gèrôme, S. G. Leon-Saval, N. G. R. Broderick, T. A. Birks, and J. C. Knight, "Control of surface modes in low loss hollow-core photonic bandgap fibers," *Opt. Express*, vol. 16, no. 2, pp. 1142–1149, Jan. 2008.
[16] S. Gao *et al.*, "Hollow-core conjoined-tube negative-curvature fiber with ultralow loss," *Nat. Commun.*, vol. 9, no. 1, 2018, Art. no. 2828.
[17] T. D. Bradley *et al.*, "Record low-loss 1.3 dB/km data transmitting antiresonant hollow core fiber," in *Proc. Eur. Conf. Opt. Commun.*, 2018, no. 1, pp. 1–3.
[18] T. D. Bradley *et al.*, "Antiresonant hollow core fiber with 0.65 dB/km attenuation in the C and L telecommunication bands," in *Proc. Eur. Conf. Opt. Commun.*, 2019, Art. no. PDP3.1.
[19] M. Komanec *et al.*, "Low-loss and low-back-reflection hollow-core to standard fiber interconnection," *IEEE Photon. Technol. Lett.*, vol. 31, no. 10, pp. 723–726, May 2019.
[20] H. Tsuchida, "Characterization of optical resonators with an incoherent light," *Opt. Express*, vol. 20, no. 28, pp. 29347–29352, Dec. 2012.
[21] C. Rohrer *et al.*, "Phase shift introduced degradation of polarization caused by bends in inhibited-coupling guiding hollow-core fibers, " *IEEE Photon. Technol. Lett.*, vol. 31, no. 16, pp. 1362–1365, Aug. 2019.
[22] T. Yoshino, K. Kurosawa, K. Itoh, and T. Ose, "Fiber-optic fabry-perot interferometer and its sensor applications," *IEEE Trans. Microw. Theory Tech.*, vol. 30, no. 10, pp. 1612–1621, Oct. 1982.



Authorized licensed use limited to: UNIVERSITY OF SOUTHAMPTON. Downloaded on April 08,2020 at 08:59:58 UTC from IEEE Xplore. Restrictions apply.

## 4.5 Optical Fiber Delay Lines in Microwave Photonics: Sensitivity to Temperature and Means to Reduce it

Reference paper:

M. Ding, Z. Feng, D. Marpaung, X. Zhang, M. Komanec, D. Suslov, D. Dousek, S. Zvánovec, E.R. Numkam Fokoua, T. Bradley, F. Poletti, D.J. Richardson, R. Slavík, "Optical Fiber Delay Lines in Microwave Photonics: Sensitivity to Temperature and Means to Reduce it" *IEEE/OSA Journal of Lightwave Technology*, 2021, 39, 2311-2318.

Relevance to the thesis:

We take a look at further application of HCFs and how our interconnection technique can enable its practical use. In this paper optical fiber based delay lines for use in microwave photonics are examined and compared. We demonstrate that the most thermally stable delay line is created using HCF, which is constructed using our interconnection technique. NANF based delay line shows the thermal sensitivity of only 0.5 ppm/K, as compared to 8 ppm/K in typical single-mode fiber.

# Optical fiber delay lines in microwave photonics: sensitivity to temperature and means to reduce it

Meng Ding, Zitong Feng, David Marpaung, Xi Zhang, Matěj Komanec, Dmytro Suslov, Daniel Dousek, Stanislav Zvánovec, Eric R. Numkam Fokoua, Thomas D. Bradley, Francesco Poletti, David J. Richardson, *Fellow, IEEE, Fellow OSA*, and Radan Slavík, *Senior Member, IEEE, Fellow OSA*

***Abstract*— One of the key functionalities in microwave photonics is to be able to define controllable time delays during the signal processing. Optical fibers are often used to achieve this functionality, especially when a long delay or a widely-tunable delay is needed. However, the stability of this delay in the presence of environmental changes (e.g., temperature) has not, to the best of our knowledge, been reviewed yet. Here, we firstly discuss the impact of temperature-induced variations on the signal propagation time in optical fibers and its implications in microwave photonics. We compare the impact of the thermal sensitivity of various delay lines for applications in which the signal is transported from point A to point B, as well as for applications in which the propagation time through a fiber or the fiber dispersion is used to create a fixed or tunable delay. In the second part of the paper we show the impact of fiber thermal sensitivity on a narrow-band microwave photonics filter made of standard single mode fiber (SSMF) and a hollow core fiber (HCF), which has significantly lower thermal sensitivity of propagation time to temperature. The central frequency of the band-pass filter changes almost 16 times more in the filter made of SSMF as compared to that of HCF, dictating very tight (0.05$^{O}$C) temperature stabilization for SSMF- based filters. On the basis of our thermal sensitivity analysis we conclude that HCFs are very promising for environmentally stable microwave photonics applications.**

***Index Terms*—Microwave Photonics, Microwave filters, Optical fiber applications, Fabry-Perot**

## I. Introduction

Microwave photonics uses optical devices and techniques for advanced processing and transport of radio frequency (RF) signals. Although integrated microwave photonics is compelling due to advantages such as small size and compactness, optical fibers still play a key role due to their ultralow loss (particularly relevant for long distances). One of the key microwave photonics requirements is to be able to set a a controllable delay of the signal being processed [1]. Defining a fixed delay is straightforwardly realized with minimum loss or signal distortion via signal propagation through a length of an integrated optics waveguide or an optical fiber. Some microwave photonics applications, however, require a tunable delay line, which is more challenging to implement. Quasi-tunable delay lines have been implemented, e.g., using a set of fiber lengths and switches with a fixed wavelength laser, Fig. 1(a) [1], while a continuously tunable delay line can be achieved, e.g., with a dispersive fiber and a tunable laser source, Fig. 1(b) [2].

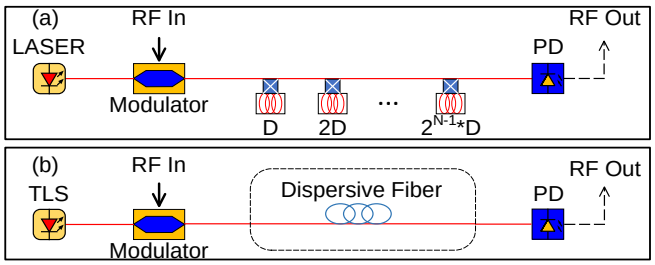


Fig. 1 Principle of tunable delay lines based on (a) switched fiber lengths with a fixed laser wavelength, and (b) a dispersive delay line with tunable laser source. D: delay; PD: photodetector; TLS, tunable laser source.

Delay lines in microwave photonics are often used to construct filters in finite input response (FIR) configurations [2], whose schematic is shown in Fig. 2 (a). By combining several (at least two) replicas of the original signal (delayed with respect to each other using delay lines) with adjusted amplitudes and phases, a filtering functionality is achieved. Indeed, infinite impulse response (IIR) configurations [2] that use output signal (after an appropriate delay) fed back into the input are also used, Fig. 2 (b). When combined with gain, such feedback structures can also be made to oscillate, forming an optoelectronic oscillator (OEO) [3]. Fig. 2(c) shows a schematic of a simple OEO. As its noise properties are directly

Manuscirpt received December xx, xxxx; revised February xx,xxxx; accepted xx, xxxx. This work was supported by EPSRC project "Airguide Photonics", under grant EP/P030181/1, Czech Technical University in Prague (SGS SGS17/182/OHK3/3T/13) and MEYS INTER-COST project LTC18008 within COST 16220 EUIMWP. Meng Ding is supported by CSC scholarship. Francesco Poletti gratefully acknowledges EU ERC (grant 682724); Radan Slavík was supported by RAEng Fellowship.

Meng Ding, Zitong Feng, Eric R. Numkam Fokoua, Xi Zhang, Thomas D. Bradley, Francesco Poletti, David J. Richardson, and Radan Slavík are with the Optoelectronic Research Centre, University of Southampton, SO17 1BJ, UK (Zitong.Feng@soton.ac.uk; R.Slavik@soton.ac.uk).

David Marpaung is with the Nonlinear Nanophotonics group, University of Twente, the Netherlands.

Matěj Komanec, Dmytro Suslov, Daniel Dousek, and Stanislav Zvánovec are with the Faculty of Electrical Engineering, Czech Technical University in Prague, 16627 Prague, Czech Republic.

related to the magnitude of the delay introduced in the feedback loop [3], a long delay (e.g., created in km-length fibers) is often used.

For stable operation of microwave photonics filters and other related devices such as OEOs, the delay introduced by a delay line should be stable with temperature. Even when using optical fibers for transport of the microwave signal (such as clock distribution [4], 5G networks [5], or radio astronomy [6]), changes in the RF signal phase due to temperature are of importance. However, the topic of this thermal stability has not, to the best of our knowledge, been comprehensively discussed in the literature in the field of microwave photonics yet.

In this paper, we first carry out a comprehensive comparison of fiber-based microwave photonics delay lines in terms of their thermal stability. We introduce the key effects that influence the thermal stability and quantify their contribution, allowing for comprehension of the topic as well as enabling microwave photonics engineers to design their systems taking the thermal stability into account. For example, using a dispersion compensating fiber instead of a standard optical fiber in the dispersive tunable delay line, up to 6 times lower sensitivity to temperature can be obtained.In the second part, we demonstrate our thermal sensitivity analysis on an IIR microwave photonics filter based on an all-fiber Fabry-Perot etalon made of standard fiber as well as novel hollow core optical fiber (the microwave photonics filter based on hollow core fibre (HCF) is demonstrated for the first time here). Thanks to the significantly better thermal stability of the HCF as compared to standard single mode fiber (SSMF), the developed HCF based microwave filter has a more than ten times better central frequency stability. We show this is of key importance in ultra-narrow pass-band filters (180 kHz in our filter, measured up to a central frequency of 40 GHz) and how this scales with the operational frequency.

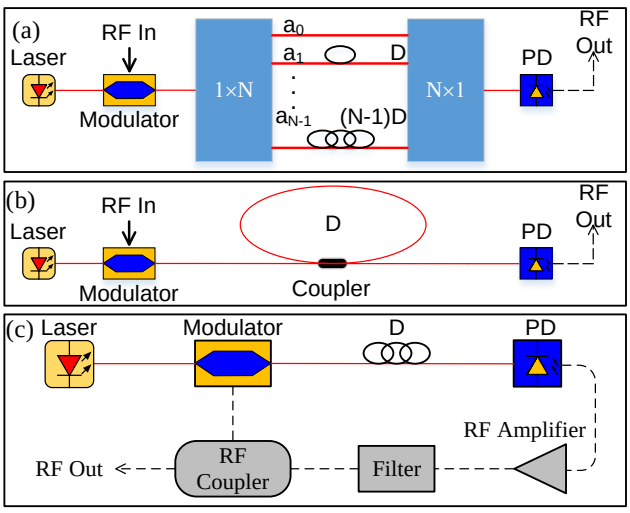


Fig. 2 Schematic of a FIR (a) and IIR (b) microwave photonics filters [2] and a simple OEO (c).

## II. Fibers' Thermal Sensitivity

There are several key configurations (Section III) used to generate delays in microwave photonics using optical fibers. Before analyzing their thermal sensitivities, we need to know the relevant thermal sensitivity properties of the optical fibers used and in particular of their propagation time and chromatic dispersion.

### A. Fiber delay

The propagation time τ of a microwave photonics signal propagating through a length $L$ of an optical fiber or a waveguide is given by:

$$\tau_{delay} = \frac{n_g L}{c}, \tag{1}$$

where $n_g$ in the group refractive index of the propagating medium and $c$ is the speed of light in vacuum. When temperature $T$ changes, two effects contribute to the time delay change: the fiber elongation with temperature (thermal expansion) and the change of propagation speed with temperature [7]. The change of time delay due to the temperature change per unit length is characterized by the thermal coefficient of delay (TCD). For an SSMF, which is made of fused silica, the TCD is about 40 ps/km/K to which the change of propagation speed with temperature contributes about 95% [7]. The thermal expansion contribution is very small thanks to the extremely low thermal expansion coefficient ($S_L$ = 5x10$^{-7}$ /K [8]) of silica glass, contributing about 2 ps/km/K [7]. For applications where the TCD of SSMF is too high, fibers with a specialty coating were developed [9] known as phase stable optical fiber (PSOF), reducing the TCD down to 3.7 ps/km/K.

Another approach is to use HCF in which light propagates through a central hole, eliminating the contribution of thermal induced propagation speed change, reducing the TCD to 2 ps/km/K, limited by the thermally-induced fiber elongation. This advantage has already been demonstrated in microwave photonics, resulting in the demonstration of an OEO with 16 times smaller sensitivity of the oscillating frequency to temperature as compared to an OEO made with SSMFs [10]. By careful design, HCFs can even be achieved with a TCD close to 0 ps/km/K [11] and an OEO with >100 times better thermal stability than SSMF has been reported using such a design [12]. Besides lower TCD, HCFs have other advantages over SSMFs relevant for microwave photonics, e.g., low nonlinearity in combination with low chromatic dispersion [13]. The key limitation to using HCF in microwave photonics applications had been up to recently transmission loss, which used to be significantly higher compared to SSMF. However, with the development of the latest generation of hollow core fibers: nested antiresonant nodeless fibers (NANFs) [14]–[17], attenuation levels of 0.28 dB/km have recently been achieved [17] and one can expect it to become even lower in the near future. NANF is therefore expected to be an ideal candidate for delay lines designed for microwave photonic and should open new device opportunities. However, to date, the use of NANF has not been demonstrated in any microwave photonics application to the best of our knowledge.

### B. Chromatic dispersion

The chromatic dispersion of an optical fiber is given by the sum of material and waveguide dispersions [18]. For weakly-

guiding fibers like SSMFs or typical dispersion compensation fibers (DCFs), the chromatic dispersion can be approximated by the three term Sellmeier equation [18], [19]:

$$D(\lambda)=\frac{S_0}{4}\left(\lambda-\frac{\lambda_0^{\,4}}{\lambda^3}\right), \tag{2}$$

where $\lambda_0$ is the zero dispersion wavelength and $S_0$ is the dispersion slope at the zerodispersion wavelength. The chromatic dispersion of SSMF and a typical DCF at C band obtained using Eq. (2) and fiber data from [20] and [21] are both plotted in Fig. 3. The temperature sensitivity of chromatic dispersion can be obtained by differentiating Eq. (2) with respect to temperature $T$:

$$\frac{dD}{dT}=\frac{D}{S_0}\cdot\frac{dS_0}{dT}-\frac{S_0\lambda_0^3}{\lambda^3}\cdot\frac{d\lambda_0}{dT}. \tag{3}$$

We then used Eq. (3) to calculate the chromatic dispersion of SSMF with a temperature increase of 100 K by using data from [20] (fiber Type A1 in [20]) and show it in Fig. 3. As concerns DCF, only the parameters relevant to the zero dispersion wavelength have been published so far (e.g., in [21]), which allows us to calculate the second term in Eq. (3), but not the first one. To allow us to illustrate the DCF's thermal sensitivity, we made an assumption that the first term in Eq. (3) (proportional to the change of $S_0$) is negligible as compared to the second one (proportional to the change of $\lambda_0$). We consider it a reasonable assumption, as for SSMF, the first term in Eq. (3) typically contributes to only 5-9% of the overall thermal sensitivity in the C-band [21]. Although it may have a larger contribution for the DCF, it is unlikely to be a dominant term.

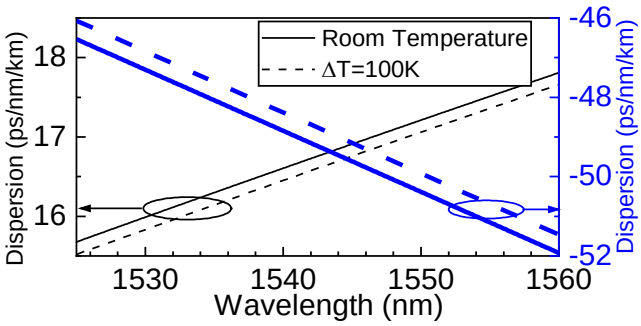


Fig. 3 Chromatic dispersion of SSMF (thin black) and DCF (thick blue, at room temperature calculated with Eq. (2) and data from [20], [21]. Chromatic disperiosn at temperature 100 K higher for SSMF was calculated with Eq. (3) and data from [20] (thin black dashed) and DCF calculated from the second term of Eq. (3) and data from [21] (thick blue dashed).

In Fig. 3 we see that over a limited bandwidth (e.g., C-band in Fig. 3) the dispersion curve is mainly red-shifted when the temperature is increased. Although this observation has been done with DCF characteristics that are approximate (as discussed earlier), it is in line with [21] and [22], where for all studied fiber types (including SSMF and DCF), the dispersion thermal sensitivity was considered to be:

$$\frac{dD(\lambda)}{dT}\cong S(\lambda)\cdot\frac{d\lambda_0}{dT}. \tag{4}$$

where D(λ) is the chromatic dispersion of interest and S(λ) is the dispersion slope at that wavelength. As $d\lambda_0/dT$ is almost constant for any fiber type ($d\lambda_0/dT$ = (0.02-0.03) nm/K [20]–[24]), dD(λ)/dT depends predominantly on the dispersion slope S(λ), as follows from Eq.(4).

For SSMF, chromatic dispersion and its thermal sensitivity are 17 ps/nm/km (at 1550 nm) and -1.5 fs/nm/km/K. For DCF, the chromatic dispersion ranges from -30 to -300 ps/nm/km [25] and $dD(\lambda)/dT$ is between 0.9 and 4 fs/nm/km/K [21] for λ~1550 nm. Photonic crystal fiber (PCF) generally provides larger dispersion, e.g., -700 ps/nm/km [26], but also has a larger dispersion slope S(λ) (as compared to DCF), making its $dD/dT$ relatively large, e.g., data from [26] leads to $dD/dT$ ~ 1.6 ps/nm/km/K.

The key properties of optical fibers relevant for microwave photonics delay lines and their thermal behavior are summarized in Table 1.

Table 1 Summary of discussed properties of opitcla fibers.

| | Silica-core fibers | | | | Hollow-core | |
|---|---|---|---|---|---|---|
| | SSMF | PSOF | DCF | PCF | PBGF | NANF |
| TCD, ps/km/K | 40 [7] | 3.7 [9] | | | 2.2 [10] | 1.7 [13] |
| Loss, dB/km | 0.2 | 0.4 [27] | | | 1.7 [28] | 0.28 [17] |
| Disp., ps/nm/km | 17 | | -30 to -300 | -700 [26] | 0-100 | 2 - 6 |
| Disp. thermal sensitivity, fs/nm/km/K | -1.5 [20] | | 0.9 to 4 [21] | 1600 [26] | | |

*SSMF: Standard single-mode fiber, PSOF: Phase-stable optical fiber, DCF: Dispersion-compensating fiber; PCF: Photonic crystal fiber, PBGF: Photonic bandgap fiber, NANF: Nested antiresonant nodeless fiber. All of these data are given in the C band.

## III. OPTICAL MICROWAVE PHOTONICS DELAY LINES AND THEIR THERMAL SENSITIVITY

Here, we divide the key configurations to generate delay in microwave photonics into three main categories that we discuss in the following text: (i) Fiber delay, (ii) Delay via fiber chromatic dispersion, and (iii) Delay with chirped fiber Bragg gratings (CFBG).

In the literature, there are two main concepts used to characterize the thermal properties of optical fibers. The first one normalizes time delay changes to the fiber length as characterized by the TCD (used, e.g., [9]) and is appropriate for applications in which fiber is used to transport a signal from point A to point B (e.g., to synchronize telescopes in radio astronomy [6]). Fiber properties relevant to these applications are summarized in Tab. 1. The other uses normalization to unit delay (1 s). For delay lines that serve to delay a signal, normalization to delay is more appropriate:

$$S_\tau = \frac{1}{\tau}\frac{d\tau}{dT}. \quad (5)$$

To distinguish between the normalization to length and delay, we use the relative unit (ppm/K) for the normalization to delay (as opposed to the ps/km/K we use for normalization to the length). In the previous section (Section II), we have already compared delay lines in terms of TCD. Here, we will discuss comparison in terms of $S_\tau$.

### A. Fiber Delay

The thermal sensitivity normalized to unit delay $S_\tau$ can be obtained from Eqs. (1) and (5) as:

$$S_\tau = \frac{1}{n_g}\frac{dn_g}{dT} + \frac{1}{L}\frac{dL}{dT} = S_n + S_L. \quad (6)$$

The first term describes the sensitivity of fiber group index to temperature, the second the thermally-induced expansion.

The thermal sensitivities $S_\tau$ of SSMF delay lines can be caculated from the TCD published in [9] to be around 8 ppm/K. A PSOF-based delay line was reported to have $S_\tau$ of 1.4 ppm/K [29]. HCF-based delay lines have been measured to have $S_\tau$ of 0.6 ppm/K using PBGF [10] and values as low as -0.08 ppm/K have been achieved when operating the PBGF close to its zero thermal sensitivity wavelength [12]. NANF has been demonstrated to achieve 0.5 ppm/K [13].

### B. Delay via fiber Chromatic Dispersion

Fig. 1(b) shows a simple schematic of a tunable dispersive fiber delay line, it's temperature sensitivity is essentially similar to that of a simple fiber delay line, Fig. 1 (a) analyzed in the previous section. However, the dispersive tunable delay line is often used in FIR filters in which signals generated by several lasers emitting at different wavelengths propagate through the same fiber and it is only the difference in their propagation times that is of importance. Fig. 4 shows a simple schematic of such a filter using two lasers with a wavelength separation of $\Delta\lambda$. Signals from both lasers are modulated by an RF signal and then the RF modulated signals at two wavelengths share the same fiber, where they experience different time delays due to the chromatic dispersion. The difference in the time delay experienced by the two lasers $\tau$ can be expressed as:

$$\tau_{disp} = LD\Delta\lambda. \quad (7)$$

Here, $D$ indicates the fiber's chromatic dispersion. Since we are interested how the delay (tuned to the desired value) changes with temperature, we consider fixed wavelength separation here, leading to:

$$S_\tau = \frac{1}{D}\frac{dD}{dT} + \frac{1}{L}\frac{dL}{dT} = S_D + S_L. \quad (8)$$

The first term is the normalized thermally induced change of dispersion and dD/dT is exactly the thermal sensitivity of dispersion as discussed in section IIB. Its value for all the considered fiber types (SSMF: -88 ppm/K at 1550 nm; DCF: -20 to -80 ppm/K, and PCF: -2800 ppm/K) is significantly higher than the second term that represents thermally-induced elongation (0.5 ppm/K).

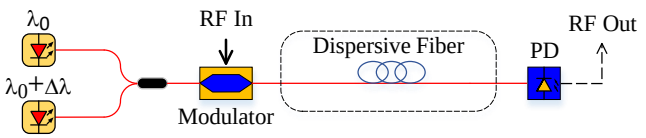


Fig. 4 Schematic of a two-tap tunable filter using a dispersive fiber structure with two lasers.

For SSMF, a tunable delay of up to 4.2 ns was demonstrated using 46 km of fiber within 5.4 nm range[2], while DCF with its significantly larger dispersion than SSMF (up to -300 ps/nm/km [25]), allowed a delay of up to 4 ns in only 1 km of fiber to be achieved with 40 nm wavelength tuning range[30]. PCFs were demonstrated to offer dispersion values of up to -700 ps/nm/km, enabling 60 ps tuning using just 10 m of fiber [31].

The length of the fiber is limited by its loss and there are other practical considerations such as cost, volume and weight. We add to this list also thermal sensitivity, which, as we mentioned earlier, is lowest with DCF, followed by SSMF, with the worst performance obtained with PCF.

### C. Delay via Chirped Fiber Bragg Gratings

Dispersive fiber from the previous sub-section can be substituted with a CFBG, which can have a large chromatic dispersion when operated in reflection, [32], [33]. The time delay difference between two lasers separated by $\Delta\lambda$ approximates as:

$$\tau_{chirp} \approx \left(\frac{L}{c}\cdot\frac{1}{\Delta\Lambda_{chirp}} + \frac{LD\Delta\lambda}{n_{eff}\Delta\Lambda_{chirp}}\right)\Delta\lambda = D_{chirp}\cdot\left(1+\frac{cD\Delta\lambda}{n_{eff}}\right)\cdot\Delta\lambda \quad (9)$$

where $\Delta\Lambda_{chirp}$ and $L$ are the period change and the length of the CFBG respectively, and $D_{chirp}=L/(c\cdot\Delta\Lambda_{chirp})$ is the CFBG chromatic dispersion that does not take into account the fiber chromatic dispersion. $n_{eff}$ is the average effective refractive index of a CFBG. Since $L$ and $\Delta\Lambda_{chirp}$ change at the same rate with temperature (for consistency with the previous analysis, we consider a uniform temperature change along the CFBG), $D_{chirp}$ does not change with temperature. Consequently, the only parameters that change with temperature are fiber chromatic dispersion and refractive index:

$$\frac{d\tau_{chirp}}{dT} = \frac{cD_{chirp}D(\Delta\lambda)^2}{n_{eff}}\left(\frac{1}{D}\frac{dD}{dT} - \frac{1}{n_{eff}}\frac{dn_{eff}}{dT}\right). \quad (10)$$

Considering a CFBG with a $D_{chirp}$ = 250 ps/nm inscribed in SSMF as an example and $\Delta\lambda$ = 20 nm, $d\tau_{chirp}/dT = -4\times10^{-5}$ ps/K, equating to a thermal sensitivity $S_\tau$ of 0.008 ppm/K, which is almost negligible.

However, real CFBGs exhibits ripples in the group delay [34], [35] due to fabrication imperfections. These ripples are

essentially time delay deviations from the ideal CFBG response. Consequently, the time delay changes significantly with temperature. The amplitude of the group delay ripples is typically independent of the CFBG parameters and is around 10 ps [34] (but this can be reduced to 1 ps by careful apodization [36]). As temperature changes, the delay of both signals (separated by $\Delta\lambda$) can change by up to ±10 ps for a typical CFBG and ±1ps for the lowest-reported ripple CFBG, generating up to 20 ps and 2ps peak-to-peak delay variations in $\tau_{chirp}$ respectively. As this variation does not change linearly with temperature (depends on the ripple period, grating chirp, etc.) we cannot define its sensitivity $S_\tau$ and can only give the peak-to-peak variations.

### D. Summary

We have discussed various microwave photonics fiber delay lines. Table 2 summarizes the results. Although we do not cover all the microwave photonics delay line implementations, their thermal sensitivities can generally be calculated from the parameters and configurations described above.

For delay generated by signal propagation in an optical fiber, HCFs are the least sensitive to temperature variations. For delays generated via chromatic dispersion, a DCF based delay line is several times less thermally sensitive than a SSMF based delay line. PCF is by far the most temperature sensitive. When using a CFBG, particular attention should be paid to the group delay ripples, which determine the delay variations with temperature and even for extremely low levels of group delay ripple (1 ps) can produce a significant sensitivity to temperature. The key parameters of the delay lines just discussed in terms of $S_\tau$ are summarized in Table 2.

Table 2 Optical delay-lines summary

| | Name | | Maximum time delay* | | $S_\tau$ (ppm/K) |
|---|---|---|---|---|---|
| Fiber delay lines | Solid-core fiber | SSMF | 100 µs | $L$ = 56 km [1] | ~8 |
| | | PSOF | 1 µs | $L$ = 0.5 km [32] | 1~2.2 |
| | HCFs | PBGF | 33 µs<br>3 µs | $L$ = 11 km [38]<br>$L$=1 km [12] | 0.6<br>0 |
| | | NANF | 1 µs | $L$ = 1.7 km [17] | 0.5 |
| Dispersive fiber delay lines | SSMF | | 10 ns | $D$ = 17 ps/nm/km | -88 |
| | DCF | | 1 ns | $D$ = -300 ps/nm/km [25] | -18~-80 |
| | PCF | | 10 ps | $D$ = -700 ps/nm/km [31] | -2800 |
| | CFBG | | 1 ns | $D_{chirp}$ = 2500 ps/nm [39] | Delay variations of ±10 ps |

*Maximum delay limited by maximum fiber length $L$ or chromatic dispersion ($D$ or $D_{chirp}$).

## IV. Novel Hollow Core Fiber Microwave Filter and Its Temperature Sensitivity

In this section, we show an example of a microwave photonics filter in which the thermal stability of the fiber used is important. We fabricate the same filter using SSMF as well as HCF and compare their performance, showing that the SSMF-based filter embodiment would only operate reliably with high-precision temperature stabilization, increasing its cost, size, and power consumption.

### A. Set-up

The core of our filter consists of an alignment-free all-fiber Fabry-Perot (FP) etalon made of 5-m of NANF, which has been reported in detail in [13]) or a 3.6-m long FC/PC-connectorized SSMF with mirrors directly-deposited on the FC/PC connector end-facets [40]. Due to the refractive index ($n$) difference (~1 for HCF and ~1.45 for SSMF), the optical length ($nL$) of the two FP etalons is nominally identical, allowing for a fair comparison. The cross-sectional electron microscope (SEM) image of the HCF we used (NANF design, with similar parameters to that used in [16]), is shown in Fig. 5.

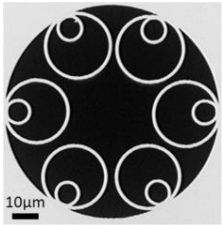


Fig. 5 The cross-sectional electron microscope (SEM) image of the NANF used in our FP etalon.

The schematic of our microwave photonics filter (we refer to it later simply as a 'filter') is shown in Fig. 6. A signal from a continuous-wave fiber laser (Rock from NP Photonics) with an output power of 16 dBm passes through a 40-GHz bandwidth Mach-Zehnder modulator (MZM), which generates two sidebands at the frequency of the RF input signal. After passing through a polarization controller (PC), the signal is injected into the FP. The laser central frequency is set (we explain later how we set this) to be resonant with the FP, i.e., to have minimum transmission loss. Both sidebands experience the same transmission loss – i.e., both are transmitted (when the RF signal frequency is a multiple of the FP spectral period) or both are equally attenuated. Thus, the FP output signal is amplitude-modulated with a modulation depth dependent on the RF signal frequency. The output signal from the FP is photodetected and

then divided into two parts. One of them is the output RF signal and is received by a vector network analyzer (VNA) to measure the amplitude and phase response of the FP. The other one is used for the laser wavelength locking to a transmission peak of the FP etalon via a feedback loop consisting of a lock-in amplifier, proportional-integral (PI) controller, and a piezo-stretcher that controls the wavelength of the Rock fiber laser. Fig. 7 shows the transmission signal and error signal before and after turning on the locking loop.

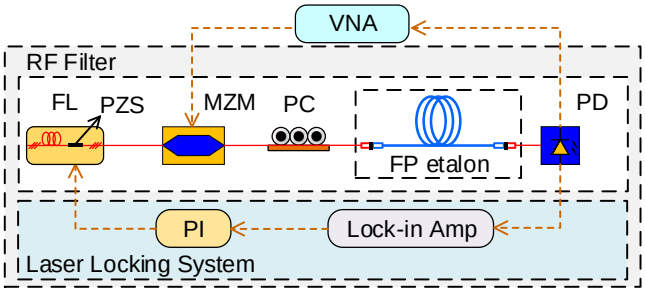


Fig. 6 Experimental set-up.FL: fiber laser; PZS: piezo-stretcher; MZM: Mach-Zehnder modulator; PC: Polarization controller; PD: photodiode; VNA: Vector network analyzer; PI: proportional-integral controller.

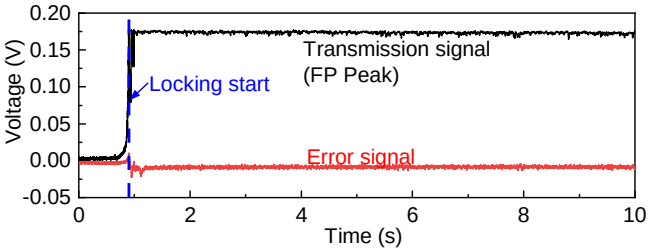


Fig. 7 Transmission signal and error signal before and after the laser wavelength has been locked to a transmission peak of the FP etalon.

### B. *Filter transmission characteristics*

For the sake of space, we show here only the filtering characteristics for the HCF-based filter, as the filter characteristics for SSMF-based filter were very similar.

The filter has a periodic transfer function with period of 28.1 MHz (given by the FP length of 5 m), shown in Fig. 8 at RF frequencies close to 10 GHz, 20 GHz and 40 GHz.

Details of the amplitude S21 response together with the phase response are shown in Fig. 9. The 3 dB passband width is 183 kHz and the phase response has the expected $\pi$ jump at the transmission peak.

### C. *Filter temperature sensitivity*

We placed the two FP etalons (based on HCF and SSMF, respectively) into the same thermal chamber. Firstly, we stabilized the temperature and measured the filters' characteristics at frequencies of 10 GHz, 20 GHz and 40 GHz. Subsequently, we increased the temperature by 1 ˚C and repeated the measurement, as shown in Fig. 10. The filter transmission peaks shifted in frequency. This shift was about 16 times larger for the SSMF-based filter than for HCF-based filter. As expected, the shift also depends linearly on the central frequency: i.e., the shift at 40 GHz is 4 times larger than at 10 GHz).

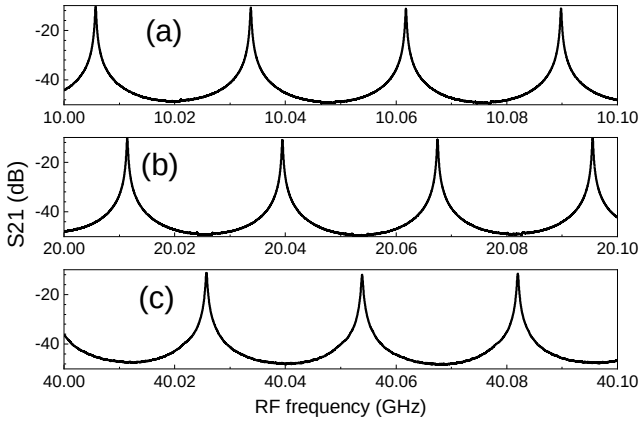


Fig. 8 Amplitude transfer characteristics of the HCF-based filter at 10 GHz (a), 20 GHz (b), and 40 GHz (c) over spans of 100 MHz.

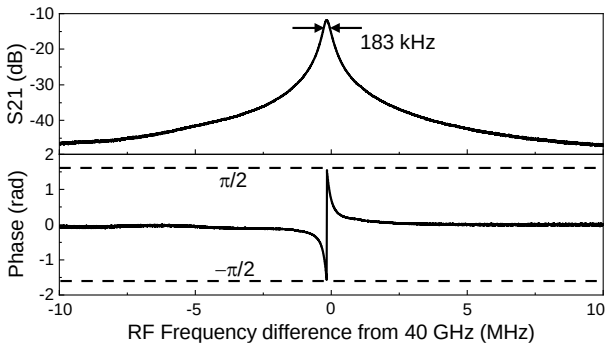


Fig. 9 Detailed amplitude and phase responses of the hollow core fiber based filter around 40 GHz RF frequency.

To extract temperature sensitivity data with good accuracy and to confirm the shift in filter transmission characteristics is linear with temperature, we kept increasing the temperature in 1 K steps and measured the position of the transmission peaks. The filters transmission peak shifts (at 40 GHz, where the change is the largest) are shown in Fig. 11. For SSMF-based filter, the transmission characteristics shift at a rate of 334 kHz/K while for the HCF-based filter the rate is only 21 kHz/K – a value almost 16 times lower as would be expected.

We also measured the filters characteristics when subject to our air-conditioned lab environment (temperature variations of about 1 K due to the air-conditioning turning on and off). Within about an hour, the frequency variations for the SSMF based filter were up to 480 kHz (at 40 GHz), while for the HCF-based filter, they were less than 30 kHz, see Fig. 12.

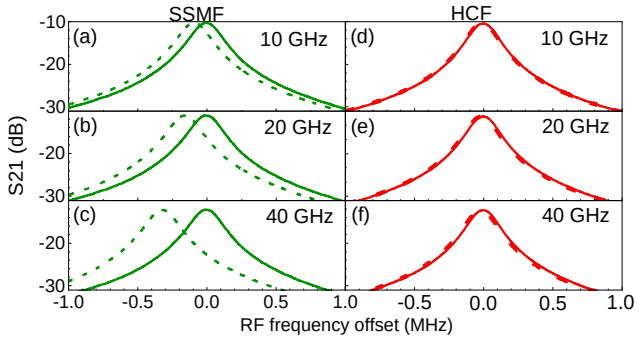


Fig. 10 Transmission characteristics measured at 25 ˚C (solid) and 26 ˚C (dashed) for SSMF-based filter (a-c, red) and HCF-based filter (d-f, green) measured at 10 GHz (a, d), 20 GHz (b, e), and 40 GHz (c,f).

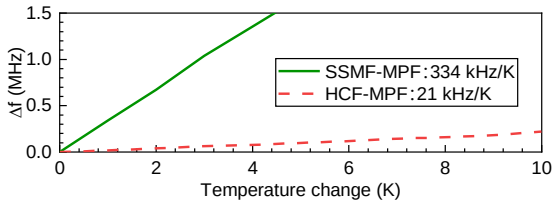


Fig. 11 Filter characteristics frequency shift at 40 GHz over 10 K temperature change for HCF-based filter (dashed, red) and SSMF-based filter (solid, green). FS: Frequency Shift of RF signal

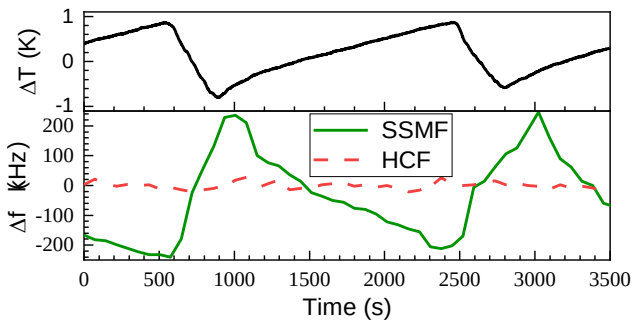


Fig. 12 Temperature variations ΔT in the laboratory and measured transmission peak frequency variations Δf for HCF (solid, green) and SSMF based (dashed, red) filters when subject to laboratory environment over 1 hour.

### D. Discussion

The results presented in Fig. 12 show that the SSMF-based bandpass filter operating at 40 GHz changes its central frequency (by up to 480 kHz) by more than is its bandwidth (3-dB bandwidth of 183 kHz), even in a temperature-controlled laboratory environment. On the other hand, an HCF-based filter allows for accurate operation without any further environmental stabilization.

To ensure that the central filter frequency does not change by more than 10% of its 3-dB bandwidth, the SSMF based filter (temperature shift of 334 kHz/K, Fig. 11) requires temperature stabilization better than 0.05 ˚C, which is rather impractical. On the other hand, the HCF based filter (21 kHz/K, Fig. 11) requires temperature stabilization of just 0.9 ˚C, easily achievable with simple temperature control. These requirements could be relaxed if the filter is operated at a lower frequency (e.g., at 10 GHz, four times larger temperature variations are acceptable), or with a larger bandwidth. However, if a lower bandwidth is targeted (e.g., in our recent work, we presented a FP fiber etalon with 10 times narrower transmission peaks [41] than presented here), the temperature stabilization needs to be improved, rendering a filter made of SSMF unstable and needing impractical mK-level temperature stabilization.

From the temperature-induced shifts given earlier (334 kHz/K and 21 kHz/K, Fig. 11), the thermal sensitivity of the used fibers (NANF hollow core fiber and SSMF) can be calculated by:

$$S_\tau = -\frac{df_{peak}/dT}{f_{peak}}. \quad (11)$$

Here, $f_{peak}$ indicates the measured central frequency of the filter. From our data and Eq. (11) we calculated a thermal sensitivity of 8.4 ppm/K (SSMF) and 0.5 ppm/K (NANF), which agrees well with the previously-published data summarized in Table 2.

## V. Conclusions

In this paper, we reviewed different configurations of optical fiber-based delay lines for microwave photonics in terms of their thermal sensitivity. The thermal sensitivity of point-to-point delay lines is best characterized by the Thermal Coefficient of Delay (TCD), which is normalized to the delay line length. Key parameters of delay lines using different optical fibers are summarized in Tab. 1, suggesting hollow core fiber (HCF) performs the best, having a TCD of as little as 2 ps/km/K.

For comparison of delay lines used primarily to create a delay, we normalize their thermal sensitivity to unit delay. There are two main configurations of such fiber-based photonic delay lines: based on propagation through a length of a fiber or propagation through a dispersive fiber or a chirped fiber Bragg grating (CFBG). The key results are summarized in Tab. 2. For simple propagation through a length of a fiber, HCF performs the best (thermal sensitivity of 0.5 ppm/K), For the dispersive delay line, devices based on dispersion compensating fiber (DCF) have the smallest thermal sensitivity (-18~-80 ppm/K). The thermal stability of a CBGF is limited by its group delay ripple, which even when strongly reduced by tight CFBG apodization is typically still at the 1-ps level.

To demonstrate the importance of the fiber thermal sensitivity in microwave photonics, we built two narrow-band IIR filters based on all-fiber Fabry-Perot etalons. The first one was made of a standard single mode fiber (SSMF), while the other one was made of low-thermally-sensitive HCF. Compared to SSMF-based filters, the HCF-based filter changes its central frequency almost 16 times less with temperature. As a result, the HCF-based filter is stable under laboratory conditions, and in real world applications would require only simple temperature control, while a SSMF-based filter would require impractically accurate/tight temperature control levels of 0.05 °C.

The experiments we have presented represent the first demonstration of the latest generation of HCF (which was recently demonstrated to enable a loss as low as 0.28 dB/km) in microwave photonics. Besides the low thermal sensitivity and a loss approaching that of SSMF, HCFs also exhibit a high nonlinear threshold, making them a very promising technology for the realization of delay lines in microwave photonics.

## VI. Acknowledgment

The data in this paper is accessible through the University of Southampton research repository (DOI: 10.5258/SOTON/D1708).

## References

[1] J. F. Diehl, J. M. Singley, C. E. Sunderman, and V. J. Urick, "Microwave photonic delay line signal processing," *Appl. Opt.*, vol. 54, no. 31, p. F35, 2015.

[2] J. Capmany, B. Ortega, and D. Pastor, "A tutorial on microwave photonic filters," *J. Light. Technol.*, vol. 24, no. 1, pp. 201–229, 2006.

[3] X. S. Yao and L. Maleki, "Optoelectronic microwave oscillator," *J. Opt. Soc. Am. B*, vol. 13, no. 8, p. 1725, Aug. 1996.

[4] S. Wang *et al.*, "2 GHz clock quantum key distribution over 260 km of standard telecom fiber," *Opt. Lett.*, vol. 37, no. 6, p. 1008, Mar. 2012.

[5] L. Gavrilovska, V. Rakovic, and V. Atanasovski, "Visions Towards 5G: Technical Requirements and Potential Enablers," *Wirel. Pers. Commun.*, vol. 87, no. 3, pp. 731–757, 2016.

[6] M. Burla *et al.*, "System integration and radiation pattern measurements of a phased array antenna employing an integrated photonic beamformer for radio astronomy applications," in *Applied Optics*, 2012, vol. 51, no. 7, pp. 789–802.

[7] A. H. Hartog, A. J. Conduit, and D. N. Payne, "Variation of pulse delay with stress and temperature in jacketed and unjacketed optical fibres," *Opt. Quantum Electron.*, vol. 11, no. 3, pp. 265–273, 1979.

[8] N. Lagakos, J. A. Bucaro, and J. Jarzynski, "Temperature-induced optical phase shifts in fibers," *Appl. Opt.*, vol. 20, no. 13, p. 2305, 1981.

[9] M. Bousonville *et al.*, "New phase stable optical fiber," *Beam Instrum. Work.*, pp. 101–103, 2012.

[10] U. S. Mutugala *et al.*, "Optoelectronic oscillator incorporating hollow-core photonic bandgap fiber," *Opt. Lett.*, vol. 42, no. 13, p. 2647, 2017.

[11] E. N. Fokoua, M. N. Petrovich, T. Bradley, F. Poletti, D. J. Richardson, and R. Slavík, "How to make the propagation time through an optical fiber fully insensitive to temperature variations," *Optica*, vol. 4, no. 6, p. 659, Jun. 2017.

[12] U. S. Mutugala *et al.*, "Hollow-core fibres for temperature-insensitive fibre optics and its demonstration in an Optoelectronic oscillator," *Sci. Rep.*, vol. 8, no. 1, pp. 1–6, 2018.

[13] M. Ding *et al.*, "Long-Length and Thermally Stable High-Finesse Fabry-Perot Interferometers Made of Hollow Core Optical Fiber," *J. Light. Technol.*, vol. 38, no. 8, pp. 2423–2427, 2020.

[14] F. Poletti, "Nested antiresonant nodeless hollow core fiber," *Opt. Express*, vol. 22, no. 20, p. 23807, 2014.

[15] T. D. Bradley *et al.*, "Record Low-Loss 1.3dB/km Data Transmitting Antiresonant Hollow Core Fibre," in *2018 European Conference on Optical Communication (ECOC)*, 2018, no. 1, pp. 1–3.

[16] T. D. Bradley *et al.*, "Antiresonant Hollow Core Fibre with 0.65 dB/km Attenuation in the C and L Telecommunication Bands," in *2019 European Conference on Optical Communication (ECOC)*, 2019, p. PDP3.1.

[17] G. T. Jasion *et al.*, "Hollow Core NANF with 0.28 dB/km Attenuation in the C and L Bands," *2020 Opt. Fiber Commun. Conf. Exhib. OFC 2020 - Proc.*, vol. 1, no. c, pp. 4–6, 2020.

[18] P. S. Andre, A. N. Pinto, and J. L. Pinto, "Effect of temperature on the single mode fibers chromatic dispersion," in *Proceedings of the 2003 SBMO/IEEE MTT-S International Microwave and Optoelectronics Conference - IMOC 2003. (Cat. No.03TH8678)*, 2004, vol. 3, no. July, pp. 231–234.

[19] P. S. André and A. N. Pinto, "Chromatic dispersion fluctuations in optical fibers due to temperature and its effects in high-speed optical communication systems," *Opt. Commun.*, vol. 246, no. 4–6, pp. 303–311, 2005.

[20] M. J. Hamp, J. Wright, M. Hubbard, and B. Brimacombe, "Investigation into the temperature dependence of chromatic dispersion in optical fiber," *IEEE Photonics Technol. Lett.*, vol. 14, no. 11, pp. 1524–1526, 2002.

[21] T. Kato, Y. Koyano, and M. Nishimura, "Temperature dependence of chromatic dispersion in various types of optical fiber," *Opt. Lett.*, vol. 25, no. 16, p. 1156, Aug. 2000.

[22] J. Rathje and M. Andersen, "Temperature induced change in the dispersion spectrum of dispersion compensating fibers," in *OFC 2003 Optical Fiber Communications Conference, 2003.*, 2003, vol. 2, pp. 712–713 vol.2.

[23] W. H. Hatton and M. Nishimura, "Temperature Dependence of Chromatic Dispersion in Single Mode Fibers," *J. Light. Technol.*, vol. 4, no. 10, pp. 1552–1555, 1986.

[24] K. S. Kim and M. E. Lines, "Temperature dependence of chromatic dispersion in dispersion-shifted fibers: Experiment and analysis," *J. Appl. Phys.*, vol. 73, no. 5, pp. 2069–2074, Mar. 1993.

[25] L. Grüner-Nielsen *et al.*, "Dispersion-compensating fibers," *Journal of Lightwave Technology*, vol. 23, no. 11. pp. 3566–3579, Nov-2005.

[26] Y. Jiang, X. Chen, B. Howley, M. Y. Chen, and R. T. Chen, "Effects of temperature fluctuation on highly dispersive photonic crystal fibers," *Appl. Phys. Lett.*, vol. 88, no. 1, 2006.

[27] Linden Photonics, Inc. "STFOC Optical Cable Non-kink Crush Proof," *datasheet*, 2020. [Online]. Available: http://www.lindenphotonics.com/documents/Linden - STFOC.pdf.

[28] P. J. Roberts *et al.*, "Ultimate low loss of hollow-core photonic crystal fibres," *Opt. Express*, vol. 13, no. 1, p. 236, 2005.

[29] J. J. Liu, X. P. Ma, G. X. Pei, N. Gan, and J. Sen Yang, "Phase-stabilized RF transmission system based on LLRF controller and optical delay line," *Nucl. Sci. Tech.*, vol. 30, no. 12, pp. 1–8, 2019.

[30] X. Zhu, F. Chen, H. Peng, and Z. Chen, "Novel programmable microwave photonic filter with arbitrary filtering shape and linear phase," *Opt. Express*, vol. 25, no. 8, p. 9232, 2017.

[31] Y. Jiang *et al.*, "Dispersion-enhanced photonic crystal fiber array for a true time-delay structured X-band phased array antenna," *IEEE Photonics Technol. Lett.*, vol. 17, no. 1, pp. 187–189, Jan. 2005.

[32] B. Ortega, J. L. Cruz, J. Capmany, M. V. Andrés, and D. Pastor, "Variable delay line for phased-array antenna based on a chirped fiber grating," *IEEE Trans. Microw. Theory Tech.*, vol. 48, no. 8, pp. 1352–1360, 2000.

[33] Y. Liu, J. Yang, and J. Yao, "Continuous true-time-delay beamforming for phased array antenna using a tunable chirped fiber grating delay line," *IEEE Photonics Technol. Lett.*, vol. 14, no. 8, pp. 1172–1174, 2002.

[34] B. Zhou, X. Zheng, X. Yu, H. Zhang, Y. Guo, and B. Zhou, "Impact of group delay ripples of chirped fiber grating on optical beamforming networks," *Opt. Express*, vol. 16, no. 4, p. 2398, 2008.

[35] M. Sumetsky, B. Eggleton, and C. de Sterke, "Theory of group delay ripple generated by chirped fiber gratings," *Opt. Express*, vol. 10, no. 7, p. 332, 2002.

[36] N. K. Srivastava, R. Parihar, and S. K. Raghuwanshi, "Efficient Photonic Beamforming System Incorporating a Unique Featured Tunable Chirped Fiber Bragg Grating for Application Extended to the Ku-Band," *IEEE Trans. Microw. Theory Tech.*, vol. 68, no. 5, pp. 1851–1857, 2020.

[37] D. Kwon and J. Kim, "All-fiber interferometer-based repetition-rate stabilization of mode-locked lasers to 10^−14-level frequency instability and 1-fs-level jitter over 1 s," *Opt. Lett.*, vol. 42, no. 24, p. 5186, Dec. 2017.

[38] Y. Chen *et al.*, "Multi-kilometer Long, Longitudinally Uniform Hollow Core Photonic Bandgap Fibers for Broadband Low Latency Data Transmission," *J. Light. Technol.*, vol. 34, no. 1, pp. 104–113, Jan. 2016.

[39] J. Zhang and J. Yao, "Broadband microwave signal processing based on photonic dispersive delay lines," *IEEE Trans. Microw. Theory Tech.*, vol. 65, no. 5, pp. 1891–1903, 2017.

[40] M. Ding, D. J. Richardson, and R. Slavik, "Long length fibre fabry-perot interferometers and their applications in fibre characterization and temperature sensing," in *2019 Conference on Lasers and Electro-Optics Europe and European Quantum Electronics Conference, CLEO/Europe-EQEC 2019*, 2019.

[41] M. Ding, E. R. N. Fokoua, T. D. Bradley, F. Poletti, D. J. Richardson, and R. Slavik, "Hollow core fiber Fabry-Perot interferometers with finesse over 3000," in *2020 Conference on Lasers and Electro-Optics (CLEO)*, 2020, p. 2F2P.

# CHAPTER 5 Conclusion

In this work I have presented an efficient coupling method leading to a novel SMF and PCF interconnection. This method is based on precise mode-field adaptation, low higher-order mode excitation and allows Fresnel losses that occur at the glass-air interface to be addressed using anti-reflective coatings. The result is a record-low loss SMF-to-HCF (HCF-to-SMF) interconnection. Furthermore, the proposed method can be adapted to be used in specific applications, such as Fabry-Perot interferometers.

In the first part of this thesis I have summarized the properties of PCFs to be able to accurately design appropriate MFAs for the coupling method. Experimental characterization of PCFs is both time and cost intensive, often requiring long segments of fiber which are difficult to obtain, making the PCF model an advantageous alternative. However, idealized models of PCF air-hole structure are often considered. Real post-draw fibers often exhibit small air-hole structure defects, such as air-hole ellipticity and change in their diameter. These minor changes can lead to significantly different PCF properties. Therefore, any PCF model requires the consideration of a real post-draw PCF. This approach is well described in [A1], where I demonstrate a simple, yet precise method for a PCF model. The results obtained using this method show a good agreement with the results obtained experimentally.

The second part of this thesis shows the results I achieved with the proposed coupling method leading to the novel interconnection technique. We show this in two articles [A2] and [A3], where we developed the interconnection between SMF and state-of-the-art PBGFs and NANFs. In both of the presented articles we were able to achieve best-reported results regarding interconnection losses. Furthermore, we significantly reduced Fresnel losses that occur at the interface between GRIN MFA and HCFs by depositing ARC. Lastly, we evaluated HOM excitation, which is a typical disadvantage of HCFs and a limiting factor for many HCF applications. The proposed coupling method showed that HOM cross-coupling can be significantly suppressed and a single-mode regime can be practically achieved.

In the last part of this thesis I show our interconnection in a practical application that allows us to effectively utilize the benefits of HCFs. In [A4] we show a slightly modified version of our interconnection which uses a highly reflective coating on GRIN MFA to create a Fabry-Perot interferometer. We show that such an interferometer has more than

order of magnitude lower frequency thermal drift compared to interferometer that created using standard SMF.

Similarly, in [A5], we examine the thermal stability of optical fiber based delay lines in microwave photonics. From the results it appears that the HCF provides the best results with thermal stability 16 times better than delay line made from SMF. HCF delay line was constructed using our interconnection technique, which allowed for easy to use, alignment free component.

The coupling method presented in this work shows the potential to advance the integration of the HCFs with existing SMF-based devices and networks. We achieved state-of-the-art results in this thesis which could serve as a benchmark for future work.

# References


[1] T. A. Birks, P. J. Roberts, P. S. J. Russell, D. M. Atkin, and T. J. Shepherd, "Full 2-d photonic bandgaps in silica/air structures," *Electronics Letters*, vol. 31, no. 22, pp. 1941–1943, Oct 1995.

[2] P. S. J. Russell, J. C. Knight, T. A. Birks, R. F. Cregan, B. J. Mangan, and J. P. de Sandro, "Photonic crystal fibres," in *Integrated Optics and Optical Fibre Communications, 11th International Conference on, and 23rd European Conference on Optical Communications (Conf. Publ. No.: 448)*, vol. 1, Sep 1997, pp. 63–64 vol.1.

[3] H. Liu, M. Hu, B. Liu, Y. Song, L. Chai, A. M. Zheltikov, and C. Wang, "Compact high-power multiwavelength photonic-crystal-fiber-based laser source of femtosecond pulses in the infrared–visible–ultraviolet range," *J. Opt. Soc. Am. B*, vol. 27, no. 11, pp. 2284–2289, Nov 2010.

[4] D. Richardson, N. Wheeler, Y. Chen, J. Hayes, S. Sandoghchi, G. Jasion, T. Bradley, E. Fokoua, Z. Liu, R. Slavik, P. Horak, M. Petrovich, and F. Poletti, "Hollow core fibres and their applications," in *Optical Fiber Communication Conference*. Optical Society of America, 2017, p. Tu3H.1.

[5] M. Kuschnerov, B. J. Mangan, K. Gong, V. A. J. M. Sleiffer, M. Herrmann, J. W. Nicholson, J. M. Fini, L. Meng, R. S. Windeler, E. M. Monberg, A. DeSantolo, K. Mukasa, V. Mikhailov, U. Feiste, W. Zhang, and R. Yu, "Transmission of commercial low latency interfaces over hollow-core fiber," *Journal of Lightwave Technology*, vol. 34, no. 2, pp. 314–320, Jan 2016.

[6] P. Roberts, F. Couny, T. Birks, J. Knight, P. St Russell, B. Mangan, H. Sabert, D. Williams, and L. Farr, "Achieving low loss and low nonlinearity in hollow core photonic crystal fibers," in *Lasers and Electro-Optics*, 2005, pp. 1240–1242 Vol. 2.

[7] Z. Liu, B. Karanov, L. Galdino, J. R. Hayes, D. Lavery, K. Clark, K. Shi, D. J. Elson, B. C. Thomsen, M. N. Petrovich, D. J. Richardson, F. Poletti, R. Slavík, and P. Bayvel, "Nonlinearity-free coherent transmission in hollow-core antiresonant fiber," *Journal of Lightwave Technology*, vol. 37, no. 3, pp. 909–916, Feb 2019.

[8] U. Mutugala, E. Numkam Fokoua, Y. Chen, T. Bradley, S. Sandoghchi, G. Jasion, R. Curtis, M. Petrovich, F. Poletti, D. Richardson, and R. Slavik, "Hollow-core fibres for temperature-insensitive fibre optics and its demonstration in an optoelectronic oscillator," *Scientific Reports*, vol. 8, 12 2018.

[9] F. Poletti, N. Wheeler, M. Petrovich, N. Baddela, E. Numkam Fokoua, J. Hayes, D. Gray, Z. Li, R. Slavík, and D. Richardson, "Towards high-capacity fibre-optic communications at the speed of light in vacuum," *Nature Photonics*, vol. 7, no. 4, pp. 279–284, 2013.

[10] E. N. Fokoua, D. J. Richardson, and F. Poletti, "Impact of structural distortions on the performance of hollow-core photonic bandgap fibers," *Opt. Express*, vol. 22, no. 3, pp. 2735–2744, Feb 2014.

[11] M. J. Li, J. A. West, and K. W. Koch, "Modeling effects of structural distortions on air-core photonic bandgap fibers," *Journal of Lightwave Technology*, vol. 25, no. 9, pp. 2463–2468, Sept 2007.

[12] G. T. Jasion, S. R. Sandoghchi, Y. Chen, N. V. Wheeler, T. Bradley, N. Baddela, J. Hayes, M. Petrovich, D. J. Richardson, J. S. Shrimpton, and F. Poletti, "Novel fluid dynamics model to predict draw of hollow core photonic band-gap fibres," in *2014 The European Conference on Optical Communication (ECOC)*, Sept 2014, pp. 1–3.

[13] G. T. Jasion, F. Poletti, J. S. Shrimpton, and D. J. Richardson, "Volume manufacturing of hollow core photonic band gap fibers: Challenges and opportunities," in *Optical Fiber Communication Conference*. Optical Society of America, 2015, p. W2A.37.

[14] I. Kaminow, T. Li, and A. E. Willner, *Optical fiber telecommunications VA: systems and networks*. Elsevier, 2008.

[15] E. Yablonovitch, "Inhibited spontaneous emission in solid-state physics and electronics," *Phys. Rev. Lett.*, vol. 58, pp. 2059–2062, May 1987.

[16] K. Saitoh, M. Koshiba, T. Hasegawa, and E. Sasaoka, "Chromatic dispersion control in photonic crystal fibers: application to ultra-flattened dispersion," *Opt. Express*, vol. 11, no. 8, pp. 843–852, Apr 2003.

[17] E. Liu, B. Yan, W. Tan, J. Xie, R. Ge, and J. Liu, "Guiding characteristics of sunflower-type fiber," *Superlattices and Microstructures*, vol. 115, pp. 123 – 129, 2018.

[18] A. Medjouri, L. M. Simohamed, O. Ziane, and A. Boudrioua, "Investigation of high birefringence and chromatic dispersion management in photonic crystal fibre with square air holes," *Optik*, vol. 126, no. 20, pp. 2269 – 2274, 2015.

[19] T. A. Birks, J. C. Knight, and P. S. J. Russell, "Endlessly single-mode photonic crystal fiber," *Opt. Lett.*, vol. 22, no. 13, pp. 961–963, Jul 1997.

[20] E. K. Akowuah, H. Ademgil, S. Haxha, and F. AbdelMalek, "An endlessly single-mode photonic crystal fiber with low chromatic dispersion, and bend and rotational insensitivity," *Journal of Lightwave Technology*, vol. 27, no. 17, pp. 3940–3947, 2009.

[21] H. Ademgil and S. Haxha, "Endlessly single mode photonic crystal fiber with improved effective mode area," *Optics Communications*, vol. 285, no. 6, pp. 1514 – 1518, 2012.

[22] R. Cregan, B. Mangan, J. Knight, T. Birks, P. Russell, P. Roberts, and D. Allan, "Single-mode photonic band gap guidance of light in air," *Science*, vol. 285, no. 5433, pp. 1537–1539, Sep. 1999.

[23] W. Zhi, R. Guobin, L. Shuqin, and J. Shuisheng, "Loss properties due to rayleigh scattering in different types of fiber," *Opt. Express*, vol. 11, no. 1, pp. 39–47, Jan 2003.

[24] E. N. Fokoua, F. Poletti, and D. J. Richardson, "Analysis of light scattering from surface roughness in hollow-core photonic bandgap fibers," *Opt. Express*, vol. 20, no. 19, pp. 20 980–20 991, Sep 2012.

[25] T. Hasegawa, Y. Tamura, H. Sakuma, Y. Kawaguchi, Y. Yamamoto, and Y. Koyano, "The first 0.14-db/km ultra-low loss optical fiber," *SEI Technical Review*, no. 86, pp. 18–22, 2018.

[26] J. Roberts, F. Couny, H. Sabert, B. Mangan, D. Williams, L. Farr, M. Mason, A. Tomlinson, T. Birks, J. Knight, and P. Russell, "Ultimate low loss of hollow-core photonic crystal fibres," *Optics express*, vol. 13, pp. 236–44, 02 2005.

[27] B. J. Mangan, L. Farr, A. Langford, P. J. Roberts, D. P. Williams, F. Couny, M. Lawman, M. Mason, S. Coupland, R. Flea, H. Sabert, T. A. Birks, J. C. Knight, and P. S. J. Russell, "Low loss (1.7 db/km) hollow core photonic bandgap fiber," in *Optical Fiber Communication Conference, 2004. OFC 2004*, vol. 2, 2004, pp. 3 pp. vol.2–.

[28] C. Smith, N. Venkataraman, M. Gallagher, D. Mueller, J. West, N. Borrelli, D. Allan, and K. Koch, "Low-loss hollow-core silica/air photonic bandgap fibre," *Nature*, vol. 424, pp. 657–9, 09 2003.

[29] N. M. Litchinitser, A. K. Abeeluck, C. Headley, and B. J. Eggleton, "Antiresonant reflecting photonic crystal optical waveguides," *Opt. Lett.*, vol. 27, no. 18, pp. 1592–1594, Sep 2002.

[30] P. Roberts, D. Williams, B. Mangan, H. Sabert, F. Couny, W. Wadsworth, T. Birks, J. Knight, and P. Russell, "Realizing low loss air core photonic crystal fibers by exploiting an antiresonant core surround," *Optics Express*, vol. 13, no. 20, pp. 8277–8285, 2005.

[31] D. V. Skryabin, "Coupled core-surface solitons in photonic crystal fibers," *Opt. Express*, vol. 12, no. 20, pp. 4841–4846, Oct 2004.

[32] Y. Chen, Z. Liu, S. R. Sandoghchi, G. T. Jasion, T. D. Bradley, E. Numkam Fokoua, J. R. Hayes, N. V. Wheeler, D. R. Gray, B. J. Mangan, R. Slavík, F. Poletti, M. N. Petrovich, and D. J. Richardson, "Multi-kilometer long, longitudinally uniform hollow core photonic bandgap fibers for broadband low latency data transmission," *Journal of Lightwave Technology*, vol. 34, no. 1, pp. 104–113, Jan 2016.

[33] M. N. Petrovich, F. Poletti, A. van Brakel, and D. J. Richardson, "Robustly single mode hollow core photonic bandgap fiber," *Opt. Express*, vol. 16, no. 6, pp. 4337–4346, Mar 2008.

[34] J. Nicholson, L. Meng, J. Fini, R. Windeler, A. DeSantolo, E. Monberg, F. DiMarcello, Y. Dulashko, M. Hassan, and R. Ortiz, "Measuring higher-order modes in a low-loss, hollow-core, photonic-bandgap fiber," *Opt. Express*, vol. 20, no. 18, pp. 20 494–20 505, Aug 2012.

[35] J. M. Fini, J. W. Nicholson, R. S. Windeler, E. M. Monberg, L. Meng, B. Mangan, A. DeSantolo, and F. V. DiMarcello, "Low-loss hollow-core fibers with improved single-modedness," *Opt. Express*, vol. 21, no. 5, pp. 6233–6242, Mar 2013.

[36] J. W. Nicholson, B. Mangan, L. Meng, A. DeSantolo, P. Vannasouk, E. Warych, and T. Taunay, "Low-loss, low return-loss coupling between smf and single-mode, hollow-core fibers using connectors," in *CLEO: 2014*. Optical Society of America, 2014, p. JTu4A.71.

[37] N. M. Litchinitser, S. C. Dunn, P. E. Steinvurzel, B. J. Eggleton, T. P. White, R. C. McPhedran, and C. M. de Sterke, "Application of an arrow model for designing tunable photonic devices," *Opt. Express*, vol. 12, no. 8, pp. 1540–1550, Apr 2004.

[38] M. S. Habib, J. E. Antonio-Lopez, C. Markos, A. Schülzgen, and R. Amezcua-Correa, "Single-mode, low loss hollow-core anti-resonant fiber designs," *Opt. Express*, vol. 27, no. 4, pp. 3824–3836, Feb 2019.

[39] J. R. Hayes, S. R. Sandoghchi, T. D. Bradley, Z. Liu, R. Slavík, M. A. Gouveia, N. V. Wheeler, G. Jasion, Y. Chen, E. N. Fokoua, M. N. Petrovich, D. J. Richardson, and F. Poletti, "Antiresonant hollow core fiber with an octave spanning bandwidth for short haul data communications," *Journal of Lightwave Technology*, vol. 35, no. 3, pp. 437–442, Feb 2017.

[40] G. T. Jasion, T. D. Bradley, K. Harrington, H. Sakr, Y. Chen, E. N. Fokoua, I. A. Davidson, A. Taranta, J. R. Hayes, D. J. Richardson, and F. Poletti, "Hollow Core NANF with 0.28 dB/km

Attenuation in the C and L Bands," in *Optical Fiber Communication Conference Postdeadline Papers 2020*. Optical Society of America, 2020, p. Th4B.4.

[41] A. D. Pryamikov, A. S. Biriukov, A. F. Kosolapov, V. G. Plotnichenko, S. L. Semjonov, and E. M. Dianov, "Demonstration of a waveguide regime for a silica hollow - core microstructured optical fiber with a negative curvature of the core boundary in the spectral region > 3.5 $\mu$m," *Opt. Express*, vol. 19, no. 2, pp. 1441–1448, Jan 2011.

[42] A. N. Kolyadin, A. F. Kosolapov, A. D. Pryamikov, A. S. Biriukov, V. G. Plotnichenko, and E. M. Dianov, "Light transmission in negative curvature hollow core fiber in extremely high material loss region," *Opt. Express*, vol. 21, no. 8, pp. 9514–9519, Apr 2013.

[43] F. Poletti, "Nested antiresonant nodeless hollow core fiber," *Opt. Express*, vol. 22, no. 20, pp. 23 807–23 828, Oct 2014.

[44] S.-F. Gao, Y.-Y. Wang, W. Ding, D.-L. Jiang, S. Gu, X. Zhang, and P. Wang, "Hollow-core conjoined-tube negative-curvature fibre with ultralow loss," *Nature Communications*, vol. 9, no. 1, 2018.

[45] T. D. Bradley, J. R. Hayes, Y. Chen, G. T. Jasion, S. R. Sandoghchi, R. Slavík, E. N. Fokoua, S. Bawn, H. Sakr, I. A. Davidson, A. Taranta, J. P. Thomas, M. N. Petrovich, D. J. Richardson, and F. Poletti, "Record Low-Loss 1.3dB/km Data Transmitting Antiresonant Hollow Core Fibre," in *2018 European Conference on Optical Communication (ECOC)*, Sep. 2018, pp. 1–3.

[46] T. Bradley, G. Jasion, J. Hayes, Y. Chen, L. Hooper, H. Sakr, M. Alonso Gouveia, A. Taranta, A. Saljoghei, H. C. Mulvad, M. Fake, I. Davidson, N. Wheeler, E. Fokoua, W. Wang, S. Sandoghchi, D. Richardson, and F. Poletti, "Antiresonant Hollow Core Fibre with 0.65 dB/km Attenuation across the C and L Telecommunication bands," in *45th European Conference on Optical Communication (ECOC 2019)*, 09 2019.

[47] H. Choi, K. Pack, S. Park, U.-C. Paek, B. Lee, and E. Choi, "Miniature fiber-optic high temperature sensor based on a hybrid structured Fabry-Perot interferometer," *Optics Letters*, vol. 33, no. 21, pp. 2455–2457, 2008.

[48] M. Xin, K. Şafak, M. Peng, A. Kalaydzhyan, W.-T. Wang, O. Mücke, and F. Kärtner, "Attosecond precision multi-kilometer laser-microwave network," *Light: Science and Applications*, vol. 6, no. 1, 2017.

[49] C. Lisdat, G. Grosche, N. Quintin, C. Shi, S. Raupach, C. Grebing, D. Nicolodi, F. Stefani, A. Al-Masoudi, S. Dörscher, S. Häfner, J.-L. Robyr, N. Chiodo, S. Bilicki, E. Bookjans, A. Koczwara, S. Koke, A. Kuhl, F. Wiotte, F. Meynadier, E. Camisard, M. Abgrall, M. Lours, T. Legero, H. Schnatz, U. Sterr, H. Denker, C. Chardonnet, Y. Le Coq, G. Santarelli, A. Amy-Klein, R. Le Targat, J. Lodewyck, O. Lopez, and P.-E. Pottie, "A clock network for geodesy and fundamental science," *Nature Communications*, vol. 7, 2016.

[50] H. Sakr, T. D. Bradley, Y. Hong, G. T. Jasion, J. R. Hayes, H. Kim, I. A. Davidson, E. N. Fokoua, Y. Chen, K. R. H. Bottrill, N. Taengnoi, P. Petropoulos, D. J. Richardson, and F. Poletti, "Ultrawide bandwidth hollow core fiber for interband short reach data transmission," in *2019 Optical Fiber Communications Conference and Exhibition (OFC)*, 2019, pp. 1–3.

[51] A. Nespola, S. Straullu, T. Bradley, H. C. Mulvad, J. Hayes, G. Jasion, M. Alonso Gouveia, S. Sandoghchi, S. Bawn, F. Forghieri, D. Richardson, F. Poletti, and P. Poggiolini, "Record pm-16qam and pm-qpsk transmission distance (125 and 340 km) over hollow-core-fiber," in

*45th European Conference on Optical Communication (ECOC 2019)*, 01 2019, pp. 285 (4 pp.)–285 (4 pp.).

[52] R. Paschotta, "Fiber joints," https://www.rp-photonics.com/fiber_joints.html, Mar 2017, online, accessed 27.08.2020.

[53] J. R. Reitz, F. J. Milford, and R. W. Christy, *Foundations of Electromagnetic Theory (4th Edition)*, 4th ed. USA: Addison-Wesley Publishing Company, 2008.

[54] S. Farsinezhad and F. Seraji, "Analysis of fresnel loss at splice joint between single-mode fiber and photonic crystal fiber," *International Journal of Optics*, vol. 2, pp. 17–21, 02 2012.

[55] T. Conese, G. Barbarossa, and M. N. Armenise, "Accurate loss analysis of single-mode fiber/d-fiber splice by vectorial finite-element method," *IEEE Photonics Technology Letters*, vol. 7, no. 5, pp. 523–525, 1995.

[56] J. T. Lizier and G. E. Town, "Splice losses in holey optical fibers," *IEEE Photonics Technology Letters*, vol. 13, no. 8, pp. 794–796, 2001.

[57] Y. L. Hoo, W. Jin, J. Ju, and H. L. Ho, "Loss analysis of single-mode fiber/photonic-crystal fiber splice," *Microwave and Optical Technology Letters*, vol. 40, no. 5, pp. 378–380, 2004.

[58] V. Parmar, R. Bhatnagar, and P. Kapur, "Optimized butt coupling between single mode fiber and hollow-core photonic crystal fiber," *Optical Fiber Technology*, vol. 19, pp. 490–494, 08 2013.

[59] P. Hofmann, A. Mafi, C. Jollivet, T. Tiess, N. Peyghambarian, and A. Schulzgen, "Detailed investigation of mode-field adapters utilizing multimode-interference in graded index fibers," *Journal of Lightwave Technology*, vol. 30, no. 14, pp. 2289–2298, July 2012.

[60] C. Wang, Y. Zhang, J. Sun, J. Li, X. Luan, and A. Asundi, "High-efficiency coupling method of the gradient-index fiber probe and hollow-core photonic crystal fiber," *Applied Sciences*, vol. 9, p. 2073, 05 2019.

[61] C. Jollivet, J. Guer, P. Hofmann, A. Mafi, and A. Schülzgen, "All-fiber mode-field adapter for low coupling loss between step-index and large-mode area fibers," in *Advanced Solid-State Lasers Congress*. Optical Society of America, 2013, p. JTh2A.02.

[62] K. Shiraishi, N. Oyama, K. Matsumura, I. Ohishi, and S. Suga, "A fiber lens with a long working distance for integrated coupling between laser diodes and single-mode fibers," *Journal of Lightwave Technology*, vol. 13, no. 8, pp. 1736–1744, 1995.

[63] G. Kliros and P. Divari, "Coupling characteristics of laser diodes to high numerical aperture thermally expanded core fibers," *Journal of Materials Science: Materials in Electronics*, vol. 20, pp. 59–62, 12 2009.

[64] H. Chen, Y. Qiu, G. Li, H. Zhang, and Q. Chen, "Improving fiber to waveguide coupling efficiency by use of a highly germanium-doped thermally expanded core fiber," *Optics & Laser Technology*, vol. 44, no. 3, pp. 679 – 682, 2012.

[65] K. Vanmol, T. Baghdasaryan, N. Vermeulen, K. Saurav, J. Watté, H. Thienpont, and J. V. Erps, "3d direct laser writing of microstructured optical fiber tapers on single-mode fibers for mode-field conversion," *Opt. Express*, vol. 28, no. 24, pp. 36 147–36 158, Nov 2020.

[66] S. Xie, R. Pennetta, and P. S. J. Russell, "Self-alignment of glass fiber nanospike by optomechanical back-action in hollow-core photonic crystal fiber," *Optica*, vol. 3, no. 3, pp. 277–282, Mar 2016.

[67] R. Zeltner, S. Xie, R. Pennetta, and P. S. Russell, "Broadband optomechanically stabilized coupling to liquid-filled hollow-core fiber using silica nanospike," in *Optics in the Life Sciences Congress*. Optical Society of America, 2017, p. OtW4D.2.

[68] R. Pennetta, S. Xie, F. Lenahan, M. Mridha, D. Novoa, and P. Russell, "Fresnel-reflection-free self-aligning nanospike interface between a step-index fiber and a hollow-core photonic-crystal-fiber gas cell," *Physical Review Applied*, vol. 8, 07 2017.

[69] D. Fan, Z. Jin, G. Wang, F. Xu, Y. Lu, D. J. J. Hu, L. Wei, P. Shum, and X. Zhang, "Extremely high-efficiency coupling method for hollow-core photonic crystal fiber," *IEEE Photonics Journal*, vol. 9, no. 3, pp. 1–8, 2017.

[70] X. Chen, X. Hu, and J. Li, "A coupling method from hollow-core fiber with large core diameter to single mode fiber," in *Asia Communications and Photonics Conference (ACPC) 2019*. Optical Society of America, 2019, p. M4A.134.

[71] W. Huang, Y. Cui, X. Li, Z. Zhou, Z. Li, M. Wang, X. Xi, Z. Chen, and Z. Wang, "Low-loss coupling from single-mode solid-core fibers to anti-resonant hollow-core fibers by fiber tapering technique," *Opt. Express*, vol. 27, no. 26, pp. 37 111–37 121, Dec 2019.

[72] H. Li, W. Huang, Z. Wang, Z. Zhou, Y. Cui, Z. Li, and X. Xi, "Double-end low-loss coupling of anti-resonant hollow-core fibers with solid-core single-mode fibers by tapering technique," *Laser Physics Letters*, vol. 17, no. 10, p. 105101, sep 2020.

[73] X. Chen, X. Hu, L. Liao, Y. Xing, G. Chen, L. Yang, J. Peng, H. Li, N. Dai, and J. Li, "High coupling efficiency technology of large core hollow-core fiber with single mode fiber," *Opt. Express*, vol. 27, no. 23, pp. 33 135–33 142, Nov 2019.

[74] P. J. Bennett, T. M. Monro, and D. J. Richardson, "Toward practical holey fiber technology: fabrication, splicing, modeling, and characterization," *Opt. Lett.*, vol. 24, no. 17, pp. 1203–1205, Sep 1999.

[75] D. K. Sharma, A. Sharma, and S. M. Tripathi, "Optimum splicing of high-index core microstructured optical fibers and traditional single-mode fibers using improved field model," *Optics & Laser Technology*, vol. 109, pp. 157–167, 2019.

[76] G. A. Miller and G. A. Cranch, "Reduction of intensity noise in hollow core optical fiber using angle-cleaved splices," *IEEE Photonics Technology Letters*, vol. 28, no. 4, pp. 414–417, Feb 2016.

[77] C. Wu, J. Song, Z. Zhang, and N. Song, "High strength fusion splicing of hollow-core photonic bandgap fiber and single-mode fiber," in *Photonics and Fiber Technology 2016 (ACOFT, BGPP, NP)*. Optical Society of America, 2016, p. AW4C.7.

[78] J. T. Krause, C. R. Kurkjian, and U. Paek, "Method for glass fiber splicing by flame fusion," 1984.

[79] E. W. M. B. S. Wang, "Advanced topics on fusion splicing of specialty fibers and devices," in *Passive Components and Fiber-based Devices*, vol. 6781, 2007, pp. 6781 – 6781 – 14.

[80] R. Robert, "Speciality fiber splicing and processing with ring of fire® technology," in *Optical fibers and aplication*. Northlab Photonics AB, 2014.

[81] J. H. Chong and M. K. Rao, "Development of a system for laser splicing photonic crystal fiber," *Opt. Express*, vol. 11, no. 12, pp. 1365–1370, Jun 2003.

[82] E. S. Douglas M. Duke, Usman Nasir, "Benefits of $co_2$ laser heating for high reliability fiber

splicing," in *Proc.SPIE*, vol. 9735, 2016, pp. 9735 – 9735 – 12.

[83] J. H. Chong, M. K. Rao, Y. Zhu, and P. Shum, "An effective splicing method on photonic crystal fiber using co2 laser," *IEEE Photonics Technology Letters*, vol. 15, no. 7, pp. 942–944, 2003.

[84] B. Bourliaguet, C. Paré, F. Émond, A. Croteau, A. Proulx, and R. Vallée, "Microstructured fiber splicing," *Opt. Express*, vol. 11, no. 25, pp. 3412–3417, Dec 2003.

[85] L. Xiao, M. S. Demokan, W. Jin, Y. Wang, and C. L. Zhao, "Fusion splicing photonic crystal fibers and conventional single-mode fibers: Microhole collapse effect," *Journal of Lightwave Technology*, vol. 25, no. 11, pp. 3563–3574, Nov 2007.

[86] O. Frazão, J. P. Carvalho, and H. M. Salgado, "Low-loss splice in a microstructured fibre using a conventional fusion splicer," *Microwave and Optical Technology Letters*, vol. 46, no. 2, pp. 172–174, 2005.

[87] A. D. Yablon and R. T. Bise, "Low-loss high-strength microstructured fiber fusion splices using grin fiber lenses," *IEEE Photonics Technology Letters*, vol. 17, no. 1, pp. 118–120, Jan 2005.

[88] H. Kim, Y. Jung, Y. Chen, S. Rikimi, F. Poletti, and D. J. Richardson, "Free space based hollow core fiber interconnection and associated in-line components," in *Optical Fiber Communication Conference (OFC) 2019*. Optical Society of America, 2019, p. Th3E.3.

[89] Y. Jung, H. Kim, Y. Chen, T. D. Bradley, I. A. Davidson, J. R. Hayes, G. Jasion, H. Sakr, S. Rikimi, F. Poletti, and D. J. Richardson, "Compact micro-optic based components for hollow core fibers," *Opt. Express*, vol. 28, no. 2, pp. 1518–1525, Jan 2020.

# Author's Publications

## List of author's publications that are relevant to the doctoral thesis

All authors contributed equally unless otherwise stated.

**Papers in the peer-reviewed journals:**


[A1] D. Suslov, M. Komanec, T. Němeček, J. Bohata, S. Zvánovec, "Exact modeling of photonic crystal fibers for determination of fundamental properties" *Optical Fiber Technology*, 2020, 56 ISSN 1068-5200.

[A2] M. Komanec, D. Suslov, S. Zvánovec, Y. Chen, T. Bradley, S.R. Sandoghchi, E.R. Numkam Fokoua, G.T. Jasion, M.N. Petrovich, F. Poletti, D.J. Richardson, R. Slavík, "Low-Loss and Low-Back-Reflection Hollow-Core to Standard Fiber Interconnection" *IEEE Photonics Technology Letters*, 2019, 31(10), 723-726. ISSN 1041-1135.

[A3] D. Suslov, M. Komanec, E.R. Numkam Fokoua, D. Dousek, A. Zhong, S. Zvánovec, T. Bradley, F. Poletti, D.J. Richardson, R. Slavík, "Low loss, high-performance interconnection between standard single-mode fiber and antiresonant hollow-core fiber", Scientific Reports, accepted, 2021

[A4] M. Ding, M. Komanec, D. Suslov, D. Dousek, S. Zvánovec, E.R Numkam Fokoua, T. Bradley, F. Poletti, D.J. Richardson, R. Slavík, "Long-Length and Thermally Stable High-Finesse Fabry-Perot Interferometers Made of Hollow Core Optical Fibe" *IEEE/OSA Journal of Lightwave Technology*, 2020, 38(8), 2423-2427. ISSN 0733-8724.

[A5] M. Ding, Z. Feng, D. Marpaung, X. Zhang, M. Komanec, D. Suslov, D. Dousek, S. Zvánovec, E.R. Numkam Fokoua, T. Bradley, F. Poletti, D.J. Richardson, R. Slavík, "Optical Fiber Delay Lines in Microwave Photonics: Sensitivity to Temperature and Means to Reduce it" *IEEE/OSA Journal of Lightwave Technology*, 2021, 39, 2311-2318.

**Papers presented in international proceedings:**

[C1] D. Suslov, D. Dousek, S. Zvánovec, E.R. Numkam Fokoua, F. Poletti, D.J. Richardson, M. Komanec, R. Slavík, “Angled interconnection between standard single-mode fiber and nested nodeless antiresonant fibers“, *CLEO*, accepted, 2021.

[C2] D. Suslov, M. Komanec, S. Zvánovec, T. Bradley, F. Poletti, D.J. Richardson, R. Slavík, “Highly-efficient and low return-loss coupling of standard and antiresonant hollow-core fibers“, *Proceedings of Frontiers in Optics*, The Optical Society, 2019. p. 1-2. ISBN 978-1-943580-67-5.

[C3] D. Suslov, M. Komanec, T. Němeček, S. Zvánovec, “High-efficiency coupling to small-core microstructured fibers for broadband dispersion characterization", *Proceedings of SPIE - The International Society for Optical Engineering*, 2018.

# List of author's publications that are not relevant to the doctoral thesis

## Papers in the peer-reviewed journals

[A6] M. Komanec, D. Dousek, D. Suslov, S. Zvánovec, "Hollow-Core Optical Fibers", *Radioengineering*, 29, pp. 417-430, 2020.

[A7] T. Němeček, M. Komanec, B. Nelsen, T. Martan, D. Suslov, P. Hartmann, S. Zvánovec , "Experimentally and analytically derived generalized model for the detection of liquids with suspended-core optical fibers", *Optical Fiber Technology*, Vol. 45, pp. 295-299, 2018.

[A8] R. Ahmad, M. Komanec, D. Suslov, S. Zvanovec, "Modified octagonal photonic crystal fiber for residual dispersion compensation over telecommunication bands", *Radioengineering*, Vol. 27, Issue 1, pp. 10-15, 2018.

## Papers presented in international proceedings:

[C5] M. Komanec, P. Vidner, J. Spáčil, D. Suslov, P. Pešek, T. Němeček, S. Zvánovec, "Polarization-maintaining Fiber-optic Gyroscope Using a Closed-loop with Kalman Filtering", *29th Conference and Exhibition on Optical Communications 2018*, 2018, p. 26-29. ISBN 978-80-86742-50-2.

[C6] M. Komanec, T. Němeček, D. Suslov, P. Vidner, S. Zvánovec, "Application of Conventional G.652 Optical Fibers with Increased Evanescent-wave Overlap for Detection of Liquids", *Proceedings of the 11th International Symposium on Communication Systems, Networks & Digital Signal Processing*, 2018

[C7] T. Nemecek, M. Komanec, D. Suslov, P.Peterka, D. Pysz, R. Buczynski, B. Nelsen, S. Zvánovec, "Development and characterization of highly-nonlinear multicomponent glass photonic crystal fibers for mid-infrared applications", *Proceedings of SPIE - The International Society for Optical Engineering*, 2017.

[C8] M. Komanec, T. Němeček, D. Suslov, R. Ahmad, T. Martan, "Optical switching based on arsenic-selenide and lead-silicate fibers", *2016 10th International Symposium on Communication Systems, Networks and Digital Signal Processing*, 2016.

[C9] M. Komanec, T. Němeček, D. Suslov, R. Ahmad, S. Zvánovec, "Detection of liquids in the near and mid-infrared based on lead-silicate suspended-core microstructured fibers", *Proceedings of SPIE - The International Society for Optical Engineering*, 2016.

[C10] M. Komanec, T. Němeček, R. Ahmad, T. Martan, D. Suslov, S. Zvánovec, "Suspended-core silica and lead-silicate fibers for nonlinear application and sensing purposes", *Proceedings of SPIE - The International Society for Optical Engineering*, 2016.

**Dmytro Suslov** ***Curriculum vitae***


| | | |
|---|---|---|
| Contact Information | Technická 2<br>Prague, 166 27 | +420 22435 2275<br>suslodmy@fel.cvut.cz |
| Date of birth | 17.12.1990 | |


**Education**

**Czech Technical University in Prague, Faculty of Electrical Engineering**, Prague, Czech Republic

PhD, Radioelectronics, - currently studying

- Disertation thesis: *Methods of Effective Signal Coupling Into the Photonic Crystal Fibers*
- Supervisor: Ing. Matěj Komanec, Ph.D.
- Co-Supervisor: prof. Ing. Stanislav Zvánovec, Ph.D.

Ing., Communications, multimedia a electronics, 2016

- Master thesis: *Supercontinuum Source in Near- and Mid–infrared Region*
- Supervisor: Ing. Matěj Komanec, Ph.D.

**Work experience**

**Researcher** 2016 to present

Czech Technical University in Prague, Faculty of Electrical Engineering, Prague, Czech Republic

**Applied results**

1. Komanec, M., Zvánovec, S., Němeček, T., Spáčil, J., Suslov, D., Vidner, P. „Fiber optic gyroscope based on polarization preserving optical fibers" 2019, Utility Model CZ 32688
2. Martan, T., Suslov, D., Komanec, M., „Technology of connection of microstructured optical fibers based on soft-glasses for generation of broadband optical signals", 2017, verified technology
3. Komanec, M., Brouček, M., Chvojka, P., Suslov, D., Zvánovec, S., „Prototype of a broadband optical signal source", 2017, prototype
4. Komanec, M., Suslov, D., Zvánovec, S., „Component based on microstructured soft-glass fiber for generation of broadband optical signals", 2016, functional sample

**Projects**

- 2019-22 Project MPO FV40089, „High-speed optical source modules for data centers", team member
- 2016-20 Project MPO FV30136, „High-precision fiber collimator arrays", team member
- 2016-17 Project COST LD15083, „High-power pulse lasers for mid-infrared supercontinuum sources", team member
- 2016-17 Project TAČR TA04010220, „Wideband optical source based on soft-glass fibers", team member

| | |
|---|---|
| Training | • February 2018, Winter school on Fiber lasers, part of COST MP1401, Switzerland<br>• August - September 2016, International Training School on Fiber Lasers & Optical Fiber Technology, part of COST MP1401, Czech Republic |
| Foreign languages | **English**: B2 level<br>**Ukrainian**<br>**Russian** |
| Other skills | Drivers licence type B |